Finite element simulation of ceramic deformation during sintering

Bahram Sarbandi

ParisTech
INSTITUT DES SCIENCES ET TECHNOLOGIES
PARIS INSTITUTE OF TECHNOLOGY

MINES ParisTech

École doctorale n°432 :
Sciences des Métiers de l'Ingénieur

Doctorat européen ParisTech

T H È S E

pour obtenir le grade de docteur délivré par

l'École nationale supérieure des mines de Paris

Spécialité « Mécanique »

présentée et soutenue publiquement par

Bahram Sarbandi

le 5 Décembre 2011

Finite Element Simulation of Ceramic Deformation During Sintering
Simulation Numérique des Déformations des Produits Céramiques lors du Frittage

Directeurs de thèse : **Jacques Besson**
David Ryckelynck

THÈSE

Jury

M. François Valdivieso	Examinateur	Ecole des Mines de St.Etienne
M. Didier Bouvard	Rapporteur	Université de Grenoble
M. Jean-Pierre Bonnet	Président	Université de Limoges
M. Elias Cueto	Rapporteur	Universidad de Zaragoza
M. Jacques Besson	Examinateur	Mines Paris - ParisTech
M. Michel Boussuge	Examinateur	Mines Paris - ParisTech
M. David Ryckelynck	Examinateur	Mines Paris - ParisTech

MINES ParisTech
Centre des Matériaux
CNRS UMR 7633, BP 87, 91003 Evry, FRANCE

To my parents, Ali and Sadaf

Remerciements - Acknowledgements

First of all, I would like to express my sincere gratitude and thanks to Prof. Jacques Besson, Prof. Michel Boussuge and Prof. David Ryckelynck for their unconditional support and guidance during this research.

This thesis has been carried out in the framework of PRECOCE project in which I had the chance to work with different partners like ICERMA, Imerys, ENSCI Limoges and Avignon Ceramic. I would like to appreciate these three years of cooperation, discussion and meetings with Dr. Yacine Sadallah, Dr. Gilles Gasgnier, Dr. Philippe Blanchart and Mr. Philippe Coulon.

I would like to thank to Prof. Didier Bouvard and Prof. Elias Cueto for accepting to write a report on this work and also to Prof. Jean-Pierre Bonnet for accepting to become the president of my jury and Prof. Francois Valdivieso for his acceptance to become a referee of my dissertation.

I would also like to thank Ms. Karine Vieillevigne and Mr. Sylvain Gailliegue for helping me in experimental part.

I am thankful to the members of CdM, specially Nicolas, Ozgur, Edouard, Ramin, Siarhei, Justin, Guillaume, Joao, Yoann, Julien, Matthieu, Yang, Abderrahmen, Jianqiang, Konstantin, Vladislav, Thomas, Delphine, Clémence, Angélique, Huaidong, Michel, Sophie, Faten, Farida, Djamel and also administrative team of CdM Konaly and Liliane.

My sincere thanks go to Bahman, Saeid, Behrouz, Mohammad, Reza and Sholeh for their friendship and all the memories and moments we shared.

My most heartfelt acknowledgement must go to my parents Ali and Sadaf and my sister Bita for their endless love and support.

Bahram Sarbandi

Résumé

Pour les fabricants de céramiques, il est primordial de maîtriser la déformation des pièces lors du frittage afin d'éviter les post-traitements et usinages ultérieurs qui augmentent les coûts de production. Face à ce problème, une alternative à la coûteuse démarche essai-erreur est la prévision par simulation numérique aux éléments finis des déformations des produits au cours du frittage.
Pour une approche numérique, il faut d'abord développer des lois de comportement qui prennent en compte les différents mécanismes de déformation induits par le frittage. Les paramètres intrinsèques aux matériaux intervenant dans ces lois doivent être déterminés par l'expérience.
Le but de cette thèse est de proposer des modèles prédictifs de la déformation des pièces céramiques lors du cycle de frittage. La procédure est basée sur une loi de comportement et les essais associés: l'essai de densification lors du frittage et l'essai de flexion-frittage.
Deux matériaux différents ont été étudiés.

- Une porcelaine fabriquée par procédé dit de coulage:
  Bien que ce procédé soit utilisé depuis des années, il continue à poser des problèmes fondamentaux qui entravent le développement de produits innovants. La déformation anisotrope durant le frittage des pièces coulées est un de ces problèmes. Les origines d'un comportement anisotrope des céramiques au cours du frittage sont liées aux propriétés rhéologiques de la barbotine, ainsi qu'à l'orientation anisotrope des particules dans les pièces crues. Une loi de comportement anisotrope prédictive de la déformation lors du frittage des pièces céramiques coulées a été développée.
- Un réfractaire à base de zircon et de silice destiné à la fabrication de noyaux pour la fonderie de superalliages:
  Le comportement des noyaux de fonderie en zircon et silice lors de frittage a été étudié à l'aide d'essais de dilatométrie et d'essais de flexion-frittage. La spécificité de ces matériaux est un très faible retrait au cours de frittage. Ce comportement est lié à la cristallisation de la silice pendant le processus de cuisson. La cristallisation s'accompagne d'un blocage de l'écoulement visqueux ainsi que le retrait du frittage. Un modèle prédictif de ce comportement a été proposé.

Les lois de comportement ainsi développées ont été implémentées dans le code de calcul par éléments finis "Zset". Après l'identification des paramètres des modèles, une simulation numérique par éléments finis a été réalisée sur des pièces génériques.
Enfin la sensibilité des résultats aux paramètres d'une loi de comportement de frittage isotrope a été étudiée en utilisant une approche par réduction de modèle.

Abstract

The control of the deformation of ceramic parts during the sintering process is essential, in order to avoid post-treatment and subsequent machining which increase the production costs. The procedure for obtaining the desired form after sintering is usually carried out by trial and error. An alternative to this costly approach is the prediction of shape instabilities during sintering by finite element simulation. With this aim, constitutive models have to be developed, taking into account the different deformation mechanisms induced by sintering. These phenomenological constitutive models use different material parameters which must be determined by experiment.
This thesis aims to propose a methodology for modelling the deformation of ceramics during sintering. This methodology consists in experimental analysis of densification and pyroplastic behaviour of ceramics, developing a phenomenological constitutive model and material parameters identification. Two different materials have been studied.

- A porcelain manufactured by slip casting process:
  Although slip casting process has been used for many years, it involves some technical problems that hinder the development of innovative products. Anisotropic deformation during sintering of slip cast parts is one of these problems. This behaviour is related to the rheological properties of the slurry and the orientation of anisotropic particles in the green part.
  An anisotropic constitutive model of sintering has been developed in order to predict the deformation of slip cast porcelain during firing process.
- Ceramic cores made by injection moulding and used for investment casting of superalloys:
  Thermomechanical behaviour of zircon-silica cores has been studied by dilatometry and sinter-bending tests. The technical specificity of these materials is their low shrinkage during sintering process. This behavior is related to the crystallization of silica at high temperature. The crystallization inhibits the viscous flow and stops sintering shrinkage. A constitutive model predicting this behaviour is also proposed.

These constitutive models have been implemented in the "Zset" finite element program. After identifying the model parameters, the finite element numerical simulation has been performed on representative parts.
Finally, the sensitivity of numerical results to mechanical parameters of an isotropic sintering model is analysed using a model reduction approach.

Contents

List of Figures

List of Tables

Chapter -I-

Introduction

Contents

I.1 Aims

In order to design new range of ceramic products, the product designer has a perfect idea about the final dimensions and shape of the part. For obtaining a perfect object without any defects, the manufacturing aspects should be taken into account, too. One of the most important stages in ceramic forming is sintering process during which the ceramic part undergoes thermo-mechanical loadings leading into shape deformation of the sintered body. Consequently, ceramic manufacturers are obliged to find the optimal forming parameters by trial and error, which involves on average 4 to 5 times mold fabrication and modification.
French ceramic producers have decided to use numerical tools instead of trial and error for reducing the cost and increasing the quality of their products. In this regard, PRECOCE [1] project has been launched in 2007. The main objective of this project consists in developing a user friendly numerical code which can predict the deformation of the ceramic part during the firing process by taking into account the thermo-mechanical properties of initial green compact. Using this code would reduce both the manufacturing cost and tool adjusting time by a rate of $30\% - 40\%$.

Figure I.1 : List of the project partners, participant and fund raisers.

[1] PREdiction du COmportement des CEramiques lors du frittage

Six french ceramic manufacturers participate in this project by providing six material-process couples. The experimental characterizations of studied materials have been done by Materials Center of Mines ParisTech and Ecole Nationale Supérieure de Céramique Industrielle de Limoges (ENSCI). According to the experimental results, constitutive models have been developed. These models have been implemented in Zset code of Centre des Materiaux Mines ParisTech. The same constitutive laws have been implemented in Aster code coupled with a commercial pre-processor (FEMAP) and has been delivered to the project partners.

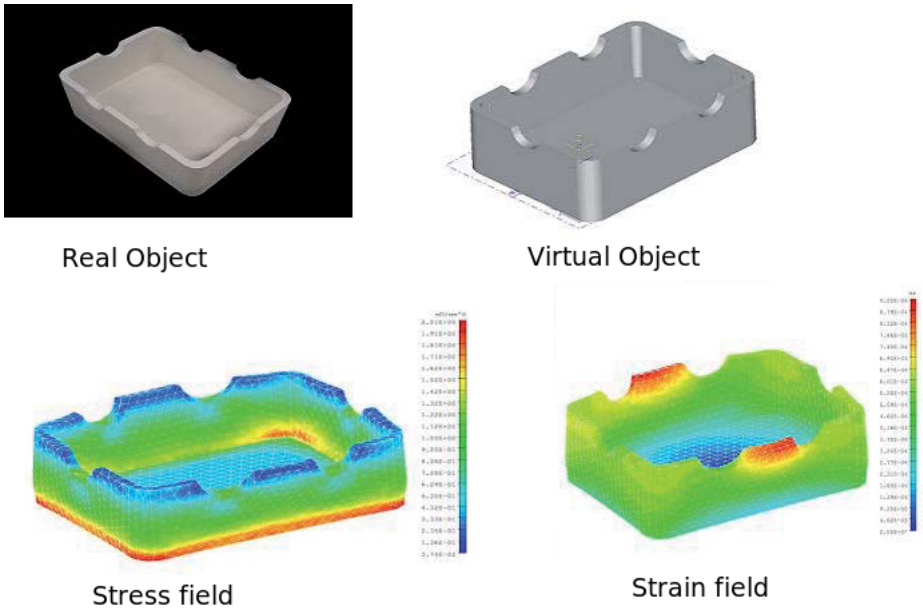

Figure I.2 : Preliminary studies on the finite element simulation of ceramic deformation during sintering.

[SadCritt2006]

In this context, Centre des Materiaux Mines ParisTech was in charge of characterising and developing the constitutive models for two materials:

- Traditional white-ware porcelain manufactured by slip casting process.
- Investment casting ceramic core mould manufactured by injection process.

The experimental tests used to characterize the behaviour of ceramic materials at high temperature are principally:

- Thermo-mechanical analysis (TMA) by Setaram dilatometer
- Kinetics of natural sintering without external load
- Kinetics of natural sintering
- Investigation of the densification behaviour of specimens along different directions
- Study of the pyroplastic behaviour of ceramics by sinter-bending test
- Microstructural observation

According to experimental results, the constitutive laws have been proposed and implemented in Zset code. The model parameters have been identified by experimental-numerical results confrontation. The shape changes of industrial parts have been simulated by finite element method. In addition, a model reduction method has been used to rapidly study the sensitivity of model parameters. Also, a new sort of tetrahedral elements with mixed formulation (displacement-pressure -volume variation) have been developed, in order to reduce the simulation size and neglect the elastic behaviour after full densification.

I.2 Outline

This document is divided into six chapters:

- Chapter I introduces the aim and outline of the project, as well as the origin of ceramic deformation during sintering.
- The literature review on constitutive models used for ceramic sintering simulation, anisotropic sintering behaviour and high temperature behaviour of ceramic core materials is presented in chapter II. In addition, the origins of anisotropic densification behaviour of ceramics during sintering is explained.
  Furthermore, silica based ceramic core materials, their thermal stability at elevated temperature and the effect of different constituents on their densification behaviour is reported.
- The experimental methods used for materials characterization are discussed in chapter III.
- Chapter IV is dedicated to slip casting process of white-ware porcelains, their thermo-mechanical characterizations, anisotropic constitutive model of sintering, mixed formulation finite elements, parameter identification method and finally, finite element simulation of an actual object.
- Chapter V deals with reactive sintering, injection moulding of ceramic cores used in investment casting of super-alloys, constitutive model for reactive sintering, model identification and simulation of a test part.
- Chapter VI relates sensitivity analysis, model reduction and some numerical aspects on modelling of sintering.

I.3 Shape instabilities / changes during sintering

The successful industrial production of a ceramic part strictly depends on the uniformity of granular pileup in a way that the dimensional changes be repetitive in the whole green compact. The firing process is a stage of production which is always applied on semi-finished porous objects manufactured by various forming processes. Consequently, the principal causes of dimensional variations during sintering, have been introduced into the green ceramic body during the forming stages. Sintering stage is not only reducing these fluctuations/variations but also is intensifying the differences observed at the end of manufacturing from one part to another. Loosing this dimensional precision is usually misunderstood and misinterpreted as sintering defects.
Predicting the dimensions of a complex part after sintering is an important challenge in powder metallurgy process. However, dimensional change of a part during sintering results from numerous geometrical and microstructural parameters. The latter plays an important

role in creating anisotropic shape change. Some of the origins of ceramic shape changes during sintering are:

- **Arrangement of powder particles**
  In fact, the initial arrangement of powder particles that depends on the forming process, can lead to non uniform density field in the green compact. Consequently, this non uniform density field will result in anisotropic deformation. Cold isostatic pressing can be used to correct this non uniform density field produced in green compact by die compaction process.

- **Initial porosity morphology**
  The morphology of initial porosity can also cause anisotropic shrinkage. The porosity morphology along pressing axis is different from the pore shapes along the axis normal to pressing in compressed compacts. As the flat-shaped porosities have natural tendency to spheroidize, shrinkage along pressing axis is different from the shrinkage along normal direction. During heating, flat-shaped porosities grow (spheroidize) along the compression axis while the body is shrinking along the other direction (normal to compression axis).

- **Particles size and distribution**
  Although, the porosity plays an important role during densification, particles size, their granulometric distribution and their shape can also influence the final form of the ceramic part after firing process.
  If the distribution of the anisotropic particles is not random, the ceramic part deformation during sintering would be anisotropic.

- **Multi-layer ceramic structure**
  Multi-layer ceramic structures are designed in order to increase the performance of ceramic materials or to fabricate multi-component materials. More complex problems have been observed during their sintering process. For instance, sintering the multi-layer materials can lead to distortion and rupture since each layer has its own shrinkage rate.In order to guarantee a perfect coherence in the interface of different layers after sintering, perfect adaptation of different shrinkages is necessary [green2008constrained].

I.4 Conclusion

As illustrated in this short introduction, understanding the densification and shrinkage behavior of green ceramic compacts with either complex or simple forms during sintering process is essential. In order to come off with a perfect result, controlling the fabrication process is also important. However, knowledge of sintering mechanisms is essential for setting up any type of densification models.
The empirical solutions can be used after a costly trial-and-error phase. In addition, this procedure should be repeated for every new parts introduced in production line.
Consequently, numerical simulation of ceramic deformation during sintering can be a more economical solution by reducing the cost and time spent for numerous trial-and-error experiences.

Summary in French

Ce chapitre constitue une introduction générale au problème de la déformation des céramiques lors de frittage. Le contexte industriel et la problématique y sont décrits: il s'agit de la conception d'un code de calcul éléments finis afin de prévoir la forme finale des matériaux céramiques après le frittage. Le plan du manuscrit est ensuite présenté.
Ce chapitre se conclut par la présentation des origines de la déformation macroscopique au cours de frittage.

Chapter -II-

Literature review

Contents

II.1 Introduction

Simulation of sintering has been the subject of research for about 40 years. In 1960s two particle sintering model explained the growth of the bridge which forms between two particles during the sintering process. During the next decade, models for shrinkage calculation have been proposed. From 1990, numerical sintering models have been developed by using mechanics of continuum media and finite element analysis in order to simulate the final density distribution and volumetric deformation of ceramic part during sintering. The following list is just a limited number of research papers on modelling of sintering used for the primary section of this chapter : [Watanabe72, BessonAbouaf91a, gillia2000phenomenological, kim2002near, mori2006finite, toussaint2004experimental, wang2006computer, zavaliangos2000numerical].

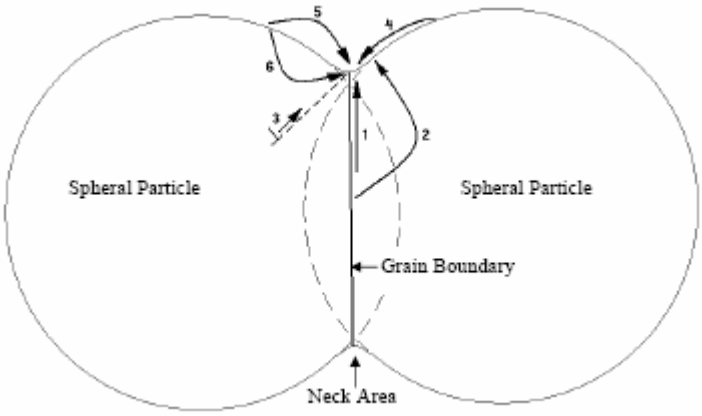

Figure II.1 : Sintering mechanism according to double particle model, 1; Diffusion in grain boundaries, 2; Volumic diffusion, 3; Plastic flow, 4; Surface diffusion, 5; Evaporation-condensation, 6; Volumic diffusion.

II.2 Different sintering models

Three different kinds of mathematical models exist for sintering simulation:

1. Microscopic (physical) model
2. Mesoscopic models
3. Macroscopic (phenomenological)models

II.2.1 Microscopic models

The most simple model, also called *two spheres model*, has been already used to illustrate the sintering mechanism.
In order to better take into account the microstructural state, sintering is assumed to be composed of three different stages:
1st stage : The two particles barely/hardly get into contact and initiate the bridge/neck forming between them.
2nd stage : The necking/bridge between the particles is formed and, consequently, the initial shapes of particles change. At this level two important phenomena can be observed:

1. The center of particles are always fixed.

2. The pores form an interconnected network around the particles.

3rd stage : In this stage, the closed porosity is formed and the pores become isolated.

II.2.2 Mesoscopic models

The mesoscopic models are based on simple geometries like two/multi-sphere model. These models involve the mass transfer mechanisms during sintering, but they are used to predict the evolution of microstructure during firing process which determine the mechanical, thermal and electrical properties at macroscopic scale. Some examples of this category: Pott models, front tackling models, vertex models, phase field models, cellular automata [holm2001computer].

II.2.3 Macroscopic models

The macroscopic models have been developed in order to simulate the shrinkage and also distortion of actual industrial parts made by ceramic-powder metallurgy during sintering process. This type of models are utterly useful for ceramic mould design, mastering the geometry of the parts and also the process parameters modifications. In these modeling cases, the mechanical, high temperature and densification properties of powder-made compacts can be described by developing a constitutive law which is based on the continuum mechanics of porous media [olevsky1998theory, bordia1988constrained, kraft2004numerical].

II.3 Continuum mechanics approach to sintering

II.3.1 Overview

The green compact material, obtained after injection and debinding, is a porous medium (solid and porosity) whose behaviour can be described by continuum mechanics. The solid phase, which is made of powder particles, is assumed to have an isotropic, non-linear viscous behaviour. In addition, when the spatial distribution of porosity is homogeneous, the global behaviour of material would be isotropic, either.
During sintering, porosity disappears under either the sintering or external mechanical stress. Consequently, the ceramic material shrinks during sintering. The relative density (and the porosity) are two important parameters which describe the densification process during sintering:

$$\theta = \frac{V_p}{V_T} \tag{II.1}$$

$$\rho = 1 - \theta \tag{II.2}$$

where V_p is the porosity volume, V_T is the total volume and ρ the relative density. During densification, porosity decreases while the relative density increases. At the end of densification, theoretically $\theta = 0$ or $\rho = 1$ and the compact is perfectly dense.

II.3.2 Mass conservation principle

Although the volume of powder compact decreases during sintering, the mass of the solid part of the compact remains unchanged. As the mass of air in pores is negligible, the relative density evolution follows the mass conservation principle:

$$\dot{\rho} + \rho\dot{e} = 0 \tag{II.3}$$

$$\dot{e} = tr(\underline{\dot{\varepsilon}}) \tag{II.4}$$

As a result:

$$\frac{\dot{\rho}}{\rho} = -tr(\underline{\dot{\varepsilon}}) \tag{II.5}$$

where $\dot{e}$ is the volumic strain rate, $\underline{\dot{\varepsilon}}$ the strain rate of solid phase and porosity. Mass conservation equation relates the volumic strain rate $\dot{e}$ with the densification rate $\dot{\rho}$.

II.3.3 Momentum conservation of continuum media

Momentum conservation of continuum media for sintering process of a powder compact can be written as:

$$\Delta\underline{\sigma} + f = \rho_{ap}\frac{d^2u}{dt^2} \tag{II.6}$$

where $\underline{\sigma}$ is the Cauchy stress tensor, f is the external force applied on the powder compact during sintering, u is the displacement field and t is the time. The term $\rho_{ap}.\frac{d^2u}{dt^2}$ is negligible as sintering is assumed to be a quasi-static transformation.

II.3.4 Heat/Energy conservation principle

Sintering process couples the thermal and mechanical phenomena simultaneously. However, the deformation of sintered part strongly depends on the evolution of temperature. The conservation energy equation in this case is expressed as:

$$\rho_{ap}C_{eff}\dot{T} - \nabla(K_{eff}\nabla T) = \beta(\underline{\sigma} : \underline{\dot{\varepsilon}}_{vp} - \sigma_s\dot{e}) \tag{II.7}$$

where C_{eff} is the heat capacity, K_{eff} is the thermal conductivity, β is the viscoplastic work dissipated as heat ($0 < \beta < 1$), $\underline{\dot{\varepsilon}}_{vp}$ is the viscoplastic strain rate and finally $\dot{e}$ is the volumic strain rate.
In free sintering case, stress and viscoplastic strain are negligible. As a result, the II.7 equation can be simplified as:

$$\rho_{ap}C_{eff}\dot{T} - \nabla(K_{eff}\nabla T) = 0 \tag{II.8}$$

The equation II.8 is the heat conservation formula which controls the temperature distribution in the sintered part. Obviously, the heat capacity and thermal conductivity of powder compact material depend on the relative density or porosity of sintered part. In addition, C_{eff} depends on temperature as well as porosity:

$$C_{eff} = C_0(T)C(\theta) \tag{II.9}$$

where $C_0(T)$ is the specific heat capacity for dense material ($\theta = 0$) and $C(\theta)$ is the specific heat capacity which depends on porosity. On the other hand, the thermal conductivity of sintered material is inversely proportional to the amount of porosity [olevsky2000instability]. The empirical equation associating K_{eff} evolution with porosity (θ) is:

$$K_{eff} = K_0\left(\frac{1-\theta}{1+\gamma^{\theta^2}}\right) \tag{II.10}$$

where K_0 is thermal conductivity for dense material and γ sensitivity of thermal conductivity to the presence of porosity. In case of which $\theta < 30\%$, the following linear equation is taken into account ($1 < \omega < 2$):

$$K_{eff} = K_0(1 - \omega\theta) \tag{II.11}$$

In the following, it is assumed that the temperature evolution in the sintered part is uniform during the entire firing process [olevsky2000instability].

II.4 Constitutive model for sintering

Deformation of polycrystalline materials during sintering, which is controlled by diffusion, is almost similar to creep induced deformation [coble2009model, folweiler2009creep, herring2009diffusional, nabarro2000grain, nabarro2002creep]. As a result, a visco-plastic constitutive model can be used in order to describe the deformation during the firing process. In addition to this viscoplastic behaviour, thermal expansion has been also observed during the first stages of sintering as well as elastic deformation of green ceramics at low temperature. Consequently, the global constitutive model which considers all sorts of deformation during sintering is called thermo-elasto-viscoplastic and is composed of three terms:

$$\underline{\dot{\varepsilon}} = \underline{\dot{\varepsilon}}_{\text{th}} + \underline{\dot{\varepsilon}}_e + \underline{\dot{\varepsilon}}_{vp} \tag{II.12}$$

Viscoplastic strain rate consists of sintering strain rate as well as creep strain rate:

$$\underline{\dot{\varepsilon}}_{vp} = \underline{\dot{\varepsilon}}_s + \underline{\dot{\varepsilon}}_c \tag{II.13}$$

Each term is discussed in detail in the following sections.

II.4.1 Elastic deformation

The linear, isotropic elastic strain rate is expressed as:

$$\underline{\varepsilon}_e = \underline{\underline{C}}_e : \underline{\sigma} \tag{II.14}$$

where $\underline{\underline{C}}_e$ is the elastic matrix. The equation II.14 can be expressed as Hooke's law:

$$\underline{\sigma} = \underline{\underline{D}}_e : \underline{\varepsilon}_e = \underline{\underline{D}}_e : (\underline{\varepsilon} - \underline{\varepsilon}_{\text{th}} - \underline{\varepsilon}_{vp}) \tag{II.15}$$

$\underline{\underline{D}}_e$ is the elastic stiffness matrix ($\underline{\underline{D}}_e = \underline{\underline{C}}_e{}^{-1}$) which is defined in equation II.16 for an isotropic material:

$$D_e = \frac{E}{1+\nu_e}\frac{1}{1-2\nu_e}\begin{pmatrix} 1-\nu_e & \nu_e & \nu_e & 0 & 0 & 0 \\ \nu_e & 1-\nu_e & \nu_e & 0 & 0 & 0 \\ \nu_e & \nu_e & 1-\nu_e & 0 & 0 & 0 \\ 0 & 0 & 0 & 1-2\nu_e & 0 & 0 \\ 0 & 0 & 0 & 0 & 1-2\nu_e & 0 \\ 0 & 0 & 0 & 0 & 0 & 1-2\nu_e \end{pmatrix} \tag{II.16}$$

where E is the elastic modulus and ν_e is the Poisson's ratio. For a porous material, the elastic modulus as well as the Poisson's ratio depend on the relative density:

$$E = E_0 \exp(-b_0(1-\rho)) \tag{II.17}$$

$$\nu_e = \nu^0 \sqrt{\frac{\rho}{3-2\rho}} \tag{II.18}$$

where ν^0 and E_0 are respectively the Poisson's ratio and the elastic modulus of a dense material.

II.4.2 Thermal strain

The thermal strain is due to thermal expansion:

$$\underline{\dot{\varepsilon}}_{\text{th}} = \alpha \dot{T} \underline{1} \tag{II.19}$$

where α is the thermal expansion coefficient which is related to the slope of the tangent of the length-temperature plot, $\dot{T}$ is temperature rate and $\underline{1}$ is the second order identity tensor.

II.4.3 Viscoplastic strain

The viscoplastic strain rate during sintering process can be expressed as:

$$\underline{\dot{\varepsilon}}_{vp} = \frac{\underline{\sigma}'}{2G_p} + \frac{\sigma_m - \sigma_s}{3K_p}\underline{1} \tag{II.20}$$

in which $\underline{\sigma}'$ is the deviatoric stress tensor and $\sigma_m = \frac{tr(\sigma)}{3} = \frac{\sigma_1+\sigma_2+\sigma_3}{3}$ the hydrostatic stress. The right side of equation II.20 consists of two terms. The first one ($\frac{\underline{\sigma}'}{2G_p}$) is associated with the deformation of the sintered part due to shear stress, while the second one ($\frac{\sigma_m-\sigma_s}{3K_p}\underline{1}$) is related to volume change during sintering.
According to equation II.13, the viscoplastic strain rate can be decomposed into a creep term:

$$\underline{\dot{\varepsilon}}_c = \frac{\underline{\sigma}'}{2G_p} + \frac{\sigma_m}{3K_p}\underline{1} \tag{II.21}$$

and a sintering term:

$$\underline{\dot{\varepsilon}}_s = \frac{-\sigma_s}{3K_p}\underline{1} \tag{II.22}$$

According to equation II.20, the powder made material will be sintered when the sintering

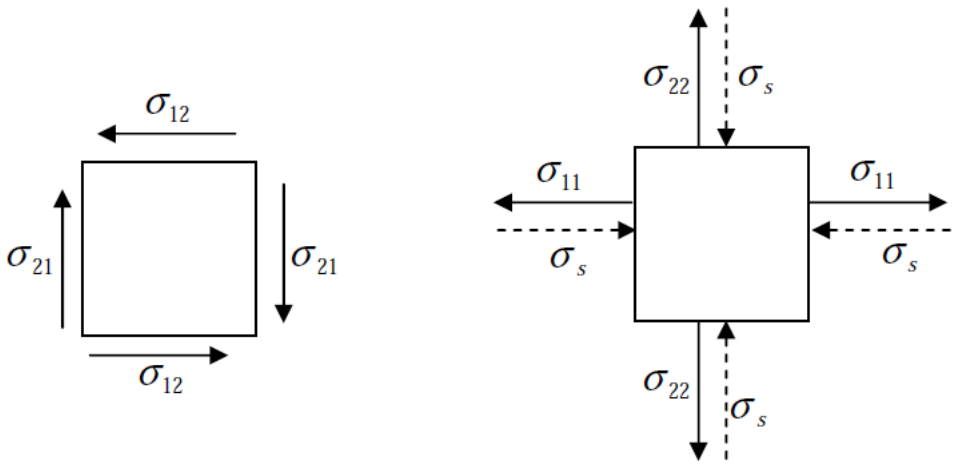

Figure II.2 : Stress state in sintered object: Deformation due to shear and volume change .

stress (σ_s) is larger than the hydrostatic Cauchy stress (σ_m).
The parameters like G_p, K_p and σ_s depend on the physical and thermo-mechanical characteristics of the material such as: relative density, temperature, grain size, diffusion coefficient and activation energy. Existing models in the literature propose different methods for determining these parameters. According to this, model identifications can be classified

into three different categories:
phenomenological identification, micro-mechanical identification and experimental identification. The following sections are dedicated to some examples of viscoplastic model parameter identification.

II.4.3.1 Olevsky and Skorohod's model

Olevsky and Skorohod have developed a phenomenological model by determining the parameters of viscoplastic constitutive law from rheological behaviour of porous material during sintering [olevsky1998theory].

$$G_p = (1-\theta)^2\eta \tag{II.23}$$

$$K_p = \frac{4(1-\theta)^3\eta}{3\theta} \tag{II.24}$$

$$\sigma_s = \frac{3\gamma_{sv}(1-\theta)^2}{r_0} \tag{II.25}$$

where θ represents the porosity ($\theta = 1-\rho$) and r_0 is the radius of spherical particle. η is the viscosity which depends on temperature:

$$\eta = \eta_0 \exp(\frac{Q}{RT}) \tag{II.26}$$

This method is easy to use in a finite element simulation code as it includes of a limited number of characteristic parameters.

II.4.3.2 Kraft's model

In order to determine the coefficients of the macroscopic constitutive law, Kraft *et al* have used the micro-mechanical model of sintering, by taking into account different mass transfer mechanisms:

$$G_p = \left(\frac{\rho_0}{\rho}\right)^{\frac{2}{3}} \left(\frac{\rho-\rho_0}{1-\rho_0}\right)^2 \left(\frac{\rho {r_0}^3}{90D}\right) \tag{II.27}$$

$$K_p = \left(\frac{\rho_0}{\rho}\right)^{\frac{2}{3}} \left(\frac{\rho-\rho_0}{1-\rho_0}\right)^2 \left(\frac{\rho {r_0}^3}{54D}\right) \tag{II.28}$$

$$\sigma_s = \left(\frac{8\gamma_{sv}}{r_0}\right) \left(\frac{\rho_0}{\rho}\right)^{\frac{1}{3}} \rho \tag{II.29}$$

where ρ_0 is the initial relative density and D is diffusion coefficient in grain boundaries:

$$D = \left(\frac{\Omega\delta_b D_{b0}}{KT}\right) \exp\left(\frac{-Q_b}{RT}\right) \tag{II.30}$$

where Q_b is the activation energy related to diffusion in grain boundaries and D_{b0} is the frequency of diffusion in grain boundaries. Based on preceding research works, Kraft et. al. have constructed a solid phase sintering constitutive model which gathers together numerous sintering mechanisms parameters. The inconvenience of this model is the identification of these numerous parameters which still remains a challenge [kraft2004numerical].

II.4.3.3 Gillia and Bouvard's model

Bouvard *et al* have proposed experimental tests for determining the viscosity and sintering stress for WC-Co powder compact and alumina. They assume that the stress level developed during sintering is negligible and, consequently, the relation between the strain rate and stress is linear. They use cylindrical specimens for strain measurement during sintering. In order to measure the radial ($\dot{\varepsilon}^z_{vp}$) and transversal ($\dot{\varepsilon}^r_{vp}$) strain rate, free sintering tests and also sintering under external loads have been performed. The viscosity and the Poisson's ratio have been calculated from these values:

$$\eta_z = \frac{\dot{\varepsilon}^z_{vp}}{\sigma_z} \tag{II.31}$$

$$\nu_{vp} = -\frac{\dot{\varepsilon}^z_{vp}}{\dot{\varepsilon}^r_{vp}} \tag{II.32}$$

where σ_z is the external applied stress. The shear and volumic modulus have been calculated respectively by:

$$G_p = \frac{\eta_z}{2(1+\nu_{vp})} \tag{II.33}$$

$$K_p = \frac{\eta_z}{3(1-2\nu_{vp})} \tag{II.34}$$

This empirical model is relatively simple and practical as it takes into account less physical parameters. On the other hand, for estimating these model coefficients, it is necessary to conduct individual tests for each material [kim2003phenomenological, gillia2001viscosity].

II.4.3.4 Riedel *etal* model

Riedel has proposed an isotropic linear viscous constitutive model which is based on a simple assumption. He assumes a bidimensional hexagon with the pores located on the edges in order to describe sintering mechanism controlled by diffusion in grain boundaries.

$$\underline{\dot{\varepsilon}} = \frac{12\Omega\delta D_b}{(\sqrt{3})(kTd^3)(1-\omega)^3}(2\underline{\sigma}' + \underline{1}(\sigma_m - (1-\omega)\sigma_s)) \tag{II.35}$$

In which Ω is atomic volume, δD_b is the diffusion coefficient at the grain boundaries, k is the Boltzman's constant, d is the surface of a grain and ω is the empty portion of the grain boundary surface which depends on the average size of porosity. If the effect of relative density and the porosity distribution are taken into account, the equation II.35 will be reduced to:

$$\underline{\dot{\varepsilon}} = \frac{\underline{\sigma}'}{2G_p} + \frac{\sigma_m - \sigma_s}{3K_p}\underline{1} \tag{II.36}$$

where G_p and K_p are shear and spherical (volumic) modules respectively:

$$G_p = \frac{(\sqrt{3})(kTd^3)(1-\omega)^3}{48\Omega\delta D_b} \tag{II.37}$$

$$K_p = \frac{4\eta_s}{3}\left(\frac{1-\rho_0}{1-\rho}\right)^{\frac{m+1}{m+\frac{5}{3}}} \tag{II.38}$$

In equations II.38 and II.37, ρ is relative density, ρ_0 is the reference density and m is a parameter which controls the shape of porosity size distribution.
In Riedel's model, the effect of porosity size distribution has been taken into account. Porosity

size distribution is controlled by grain boundary diffusion. However, in this model, grain growth is not considered [riedel1990constitutive].

II.4.3.5 Johnson *etal* model, combined stage model

This model is based on a general viscous flow equation and its atomic conversion into shrinkage which is viable for all sintering stages.
In order to characterize the microstructure, two parameters are involved in this model: geometry (M) and scale (Γ). In comparison to linear visco-elastic constitutive law, Johnson's model can simulate the material properties with larger density variations. On the other hand, it's more difficult to determine the parameters of this model, especially the scale (Γ) parameter, as its physical significance is not very clear.

$$-\frac{dL}{Ldt} = \frac{\gamma_s \Omega}{kT}\left(\frac{\Gamma_v D_v}{M^3} + \frac{\Gamma_b \delta D_b}{M^4}\right) \tag{II.39}$$

The term on the left side of equation II.39 represents the instantaneous linear shrinkage. γ_s is the surface energy (tension), Ω is the atomic volume, k is the Boltzmann's constant, M is the average diameter of grains. D_v and D_b are the volumic diffusion and the diffusion coefficient in the grain boundaries respectively. Γ is the scale parameter which depends on the average distance of diffusion, geometrical aspects of microstructure and diffusional driving force [hansen1992combined].

II.4.3.6 Besson-Abouaf model

Besson and Abouaf have proposed a generic phenomenological approach to simulate viscoplastic deformation of porous compacts. The model introduces an effective scalar stress σ_{eff} which is defined as a quadratic function of the stress tensor by:

$$\sigma_{eff}^2 = C(\rho)\sigma_{vM}^2 + F(\rho)(\sigma_{kk} - 3P_s)^2 \tag{II.40}$$

where σ_{vM} is the von Mises stress and σ_{kk} the trace of the stress tensor. P_s is the sintering pressure. C and F are decreasing functions of the relative density ρ and represent the stress localization generated by the porosity. The effective stress is decomposed into a shear ($C(\rho)\sigma_{vM}^2$) part and a pressure part ($F(\rho)(\sigma_{kk} - 3P_s)^2$) . Therefore, it allows the modelling of both densification and shear deformation. At full density the functions C and F should have the values: $C = 1$ and $F = 0$. In the full density case, the σ_{eff}^2 is equal to the von Mises equivalent stress. The use of the sintering pressure (P_s) implies that the basic mechanisms responsible for sintering and creep are the same. The viscoplastic strain rate tensor is obtained as:

$$\underline{\dot{\varepsilon}}_{vp} = \rho\frac{\sigma_{eff}}{\eta}\frac{\partial \sigma_{eff}}{\underline{\sigma}} = \rho\frac{\sigma_{eff}}{\eta}\left(\frac{3}{2}C\underline{\sigma}' + F(\sigma_{kk} - 3P_s)\underline{1}\right) \tag{II.41}$$

where it is assumed that the matrix material has a linear viscous behaviour. η represent the viscosity of the dense material. Finally one gets:

$$\frac{1}{G_p} = \frac{\rho}{\eta}\frac{3}{2}C \tag{II.42}$$

$$\frac{1}{3K_p} = \frac{\rho}{\eta}3F \tag{II.43}$$

so that the model corresponds to the generic framework presented in II.3. In this constitutive model, the grain growth which can have drastic influence on the creep and the densification kinetics of ceramics has been taken into account. The grain growth rate during sintering ($\dot{G_{sa}}$) is given by:

$$\dot{G}_{sa} = \frac{k_0}{G^m} \tag{II.44}$$

Grain growth is modelled assuming that deformation produces a damage (D) whose evolution is controlled by:

$$\dot{D} = k_1 w - k_2 D \tag{II.45}$$

And finally the grain growth rate $\dot{G}$ is given by:

$$\dot{G} = k_3 D + \dot{G}_{sa} \tag{II.46}$$

[besson1992rheology]

II.4.4 Model conclusion

As mentioned before, the main difference of sintering constitutive models is related to model parameters. In figure II.3, the bulk modulus and the sintering stress of different models, as well as their effect on densification behaviour, are compared [olevsky1998theory].

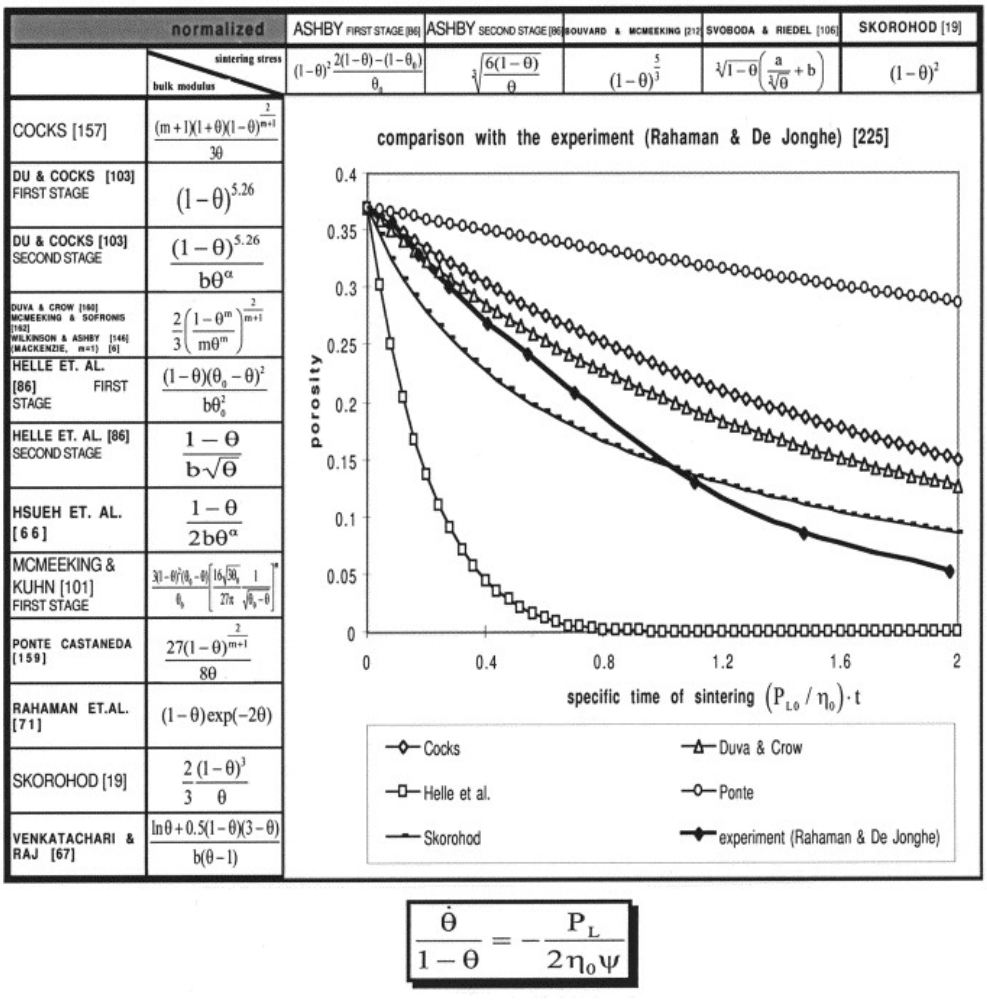

$$\frac{\dot{\theta}}{1-\theta} = -\frac{P_L}{2\eta_0\psi}$$

Figure II.3 : Different sintering models comparison.
[olevsky1998theory]

II.5 Literature review on anisotropic sintering

In this section, the anisotropic behaviour of ceramics during sintering is discussed. The origin of this anisotropic behaviour is related to the forming process of the green body. This behaviour has been observed in some specific cases such as the sintering of co-fired ceramics, thin films as well as the sintering of ceramics manufactured by hot forging of powder compounds , slip casting and tape casting processes.
In these cases, the isotropic constitutive laws are no longer valid to predict the materials behaviour during the firing process.
In this section, some examples of anisotropic sintering are discussed.

II.5.1 Sintering of co-fired ceramic films

The ceramic films are used in different applications such as protective coatings for different functional parts, reactive coatings on a different ceramic substrate as well as solid oxide fuel cells. The multi-layer ceramic structures are also used in electronics industry. Sintering of these low temperature co-fired ceramics (LTCC) is a challenging task since different combination of materials are sintered in one operation [pohle2006effect, calata2001constrained].

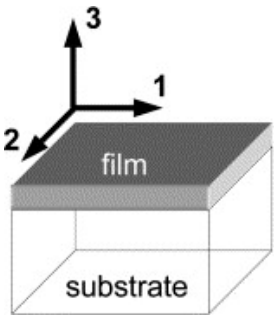

Figure II.4 : Schematic of a green ceramic film co-layered with a stiff substrate. [bordia2006anisotropic]

Since the ceramic films are in contact with a stiff substrate, a biaxial tensile stress develops during their firing process. This tensile stress may lead to defects such as curvature and warpage of film during the heat treatment [taub2010constrained]. By considering the geometry in figure II.4, Bordia *et al* assume that the deformation of the film in the plane (1-2) is isotropic since it is constrained by the stiff substrate whereas the film can shrink in the plane (1-3) along the axis 3. The following expressions are proposed for the stress and the film densification rate:

$$\sigma = -\frac{E_1 \dot{\varepsilon}_1^{free}}{1-\nu_{12}} \tag{II.47}$$

$$\dot{\varepsilon}_3 = \dot{\varepsilon}_3^{free} + \frac{2\nu_{13}}{1-\nu_{12}}\dot{\varepsilon}_1^{free} \tag{II.48}$$

As shown in the II.47 and II.48 equations, anisotropic viscosities, viscous Poisson's ratio and two free strain rates have to be determined [bordia2006anisotropic].

II.5.2 Anisotropic densification behaviour of sinter-forged ceramics

Zuo *et al* have studied the evolution of hot-forged alumina ceramics during sintering. They have observed the microstructure of samples under free sintering and constrained sintering.

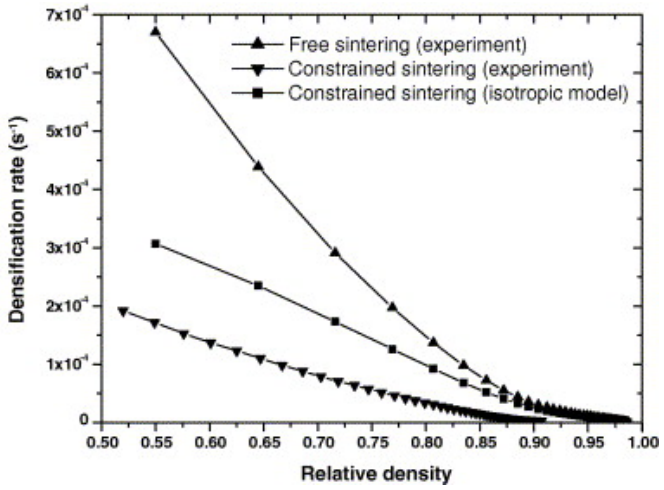

Figure II.5 : Comparison between experimental and numerical densification rates using isotropic model for free and constrained sintering of hot forged samples.
[zuo2003critical]

Figure II.5 shows that the isotropic model is unable to describe the densification behaviour observed during free and constrained sintering of hot forged alumina samples. The observations carried out by scanning electron microscopy (SEM) on the free sintered and constrained sintered specimens show that the pores are randomly oriented in the free sintered samples. However, they have preferential orientations in hot forged samples. In addition, during free sintering, spherical pores remain spherical whereas in hot forged sintering, pores take the form of an ellipsoid under the compressive stress [zuo2003critical, bordia2006anisotropic].

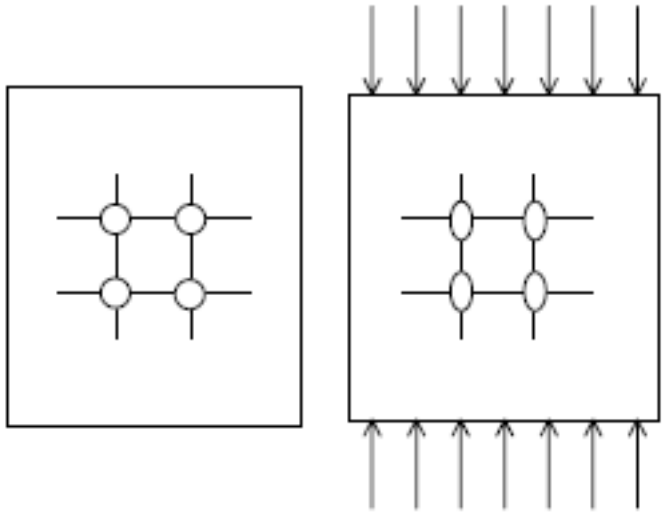

Figure II.6 : Pores structure in sintering of free (left) and hot forged (right) samples.
[bordia2006anisotropic]

According to these results, the following equations are proposed for stress state and strain rates in hot-forged samples. As the radial strain rate of samples during sinter-forging is zero,

the axial stress is:

$$\sigma_3 = \frac{E_3 \dot{\varepsilon}_1^{free}}{\nu_{31}} \tag{II.49}$$

and the axial strain rate is:

$$\dot{\varepsilon}_3 = \dot{\varepsilon}_3^{free} + \frac{\dot{\varepsilon}_1^{free}}{\nu_{31}} \tag{II.50}$$

In conclusion, Zuo *et al* and Bordia *et al* have studied the anisotropic densification of co-fired ceramic films and hot-forged ceramic specimens. In both cases, anisotropy has been detected and models have been developed by just modifying the isotropic equations. They have concluded that the microstructure of sintering body becomes anisotropic because of non-hydrostatic stresses during sintering [zuo2003critical, bordia2006anisotropic].
However, in our work, the anisotropic behaviour is due to the preferential orientations of slip cast ceramics and a different approach for modelling has been taken into account.

II.5.3 Anisotropic shrinkage in casting processes

As mentioned before, the origins of an anisotropic densification of ceramics can be related to the forming process. The shape distortion of sintered part manufactured by monolithic injection molding, extrusion, slip and tape casting tremendously increases the processing costs due to further finishing steps.
In this part, the anisotropic behaviour observed during the sintering of tape cast materials is explained.
Raj *et al* have studied the effect of processing parameters and particle shape on the anisotropic shrinkage in tape-cast alumina [raj1999anisotropic]. They have defined the shrinkage anisotropy as:

$$K_A = 100 \left(1 - \frac{\varepsilon_{xx}}{\varepsilon_{yy}}\right) \tag{II.51}$$

In equation II.52, ε_{xx} is the shrinkage in the plane of the tape in the casting direction and ε_{yy} in the transverse direction. The instantaneous shrinkage anisotropy between the increments $n-1$ and n can be defined as:

$$K_B = 100 \left(1 - \left(\frac{\varepsilon_{yy,n-1} - \varepsilon_{yy,n}}{\varepsilon_{xx,n-1} - \varepsilon_{xx,n}}\right)\left(\frac{1 - \varepsilon_{xx,n-1}}{1 - \varepsilon_{yy,n-1}}\right)\right) \tag{II.52}$$

Figure II.7 shows the instantaneous shrinkage anisotropy as a function of shrinkage in the casting direction for the tape cast alumina. In the final stages of sintering, the instantaneous shrinkage anisotropy approaches zero. This means that the shrinkage rates in the casting and transverse directions are found to be approximately the same.

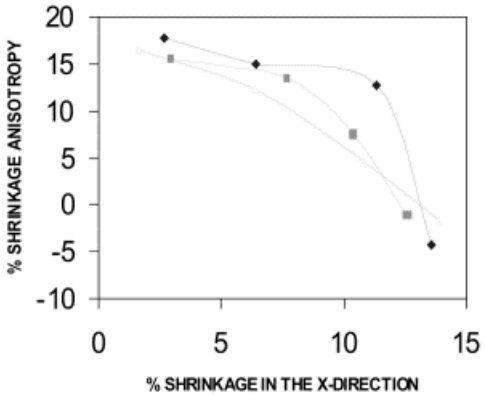

Figure II.7 : Instantaneous shrinkage anisotropy as a function of shrinkage in the casting direction for tape cast alumina.

[raj1999anisotropic]

The anisotropic shrinkage usually observed during the densification of green bodies formed by casting processes is due to high shear rates involved in processes such as tape casting, injection molding or slip casting.
High shear rates during forming process result in preferential orientations of the microstructure. Therefore, the neck length in the casting direction increases faster than that of transverse direction during the sintering process. Consequently, the different rates of neck length growth along casting and transverse directions leads to the shrinkage anisotropy. Zhang and Schneibel have proposed a three-dimensional model for the sintering of two particles by surface and grain boundary diffusion [zhang1998sintering]. By extending this model to a 2D periodic arrangements of oriented ellipses, Raj and Cannon have simulated the solid state sintering of tape cast alumina [raj2002anisotropic].

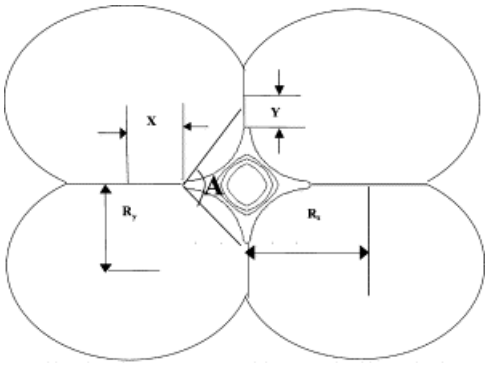

Figure II.8 : 2D arrangement of oriented elliptical particles to model solid state sintering and the simulation of pore shape variation in the center.

[raj2002anisotropic]

Figure II.8 shows the geometry used for simulating the solid state sintering in tape cast materials. The constitutive equations for grain boundary and surface diffusion can be found in [zhang1998sintering,zhang1995sintering]. The velocity of the normal surface can be calculated by the Laplacian of the curvature from Fick's second law of diffusion. In a similar way, the rate of particle approach is:

$$V_y = \frac{3\Gamma}{X^3}\left(sin\left(\frac{A}{2}\right) - KX\right) \tag{II.53}$$

In equation II.53 K is the curvature, X is half the neck length and Γ is the diffusivity ratio:

$$\Gamma = \frac{\delta_b D_b}{\delta_s D_s} \tag{II.54}$$

After solving the equations using the finite difference method, the shrinkage rates in both casting and transverse directions can be obtained.
Figure II.9 shows the numerical simulation of the instantaneous shrinkage anisotropy as a function of shrinkage in the casting direction for different values of Γ.

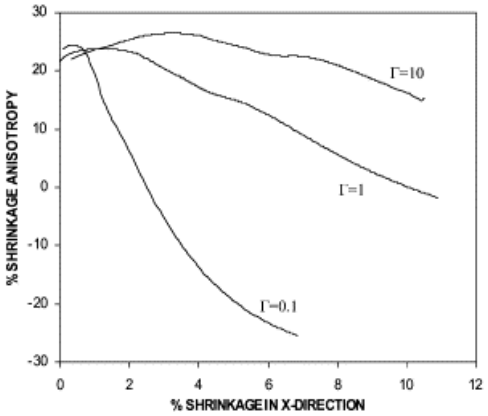

Figure II.9 : Numerical simulation of the instantaneous shrinkage anisotropy as a function of shrinkage in the casting direction for tape cast alumina.
[raj1999anisotropic]

By comparing figure II.9 which represents the numerical simulation with the experimental results shown in figure II.9, the trends observed between the experimental and simulated results match for a Γ between 1 and 10 [raj2002anisotropic].
The same phenomena have been observed during firing of die-pressed compacts [boccaccini1998situ, ozer2006anisotropic].

II.5.4 Shrinkage anisotropy during sintering of uniaxially pressed compacts

In this part, the anisotropic shrinkage of uniaxially pressed compacts is reviewed. According to a study carried out by Shui *et al*, the origins of the sintering shrinkage anisotropy in uniaxially pressed alumina compacts is associated with the particle orientation as well as the anisotropic particle packing density [shui2002origin]. The investigations have been carried out on two types of alumina particles with slightly elongated shape and spherical shape.
An anisotropic shrinkage is observed during the sintering of the compacts having elongated shape of particles even after cold isostatic pressing. However, no shrinkage anisotropy is observed during the firing process of the compacts with spherical shape of particles for the same processing conditions.

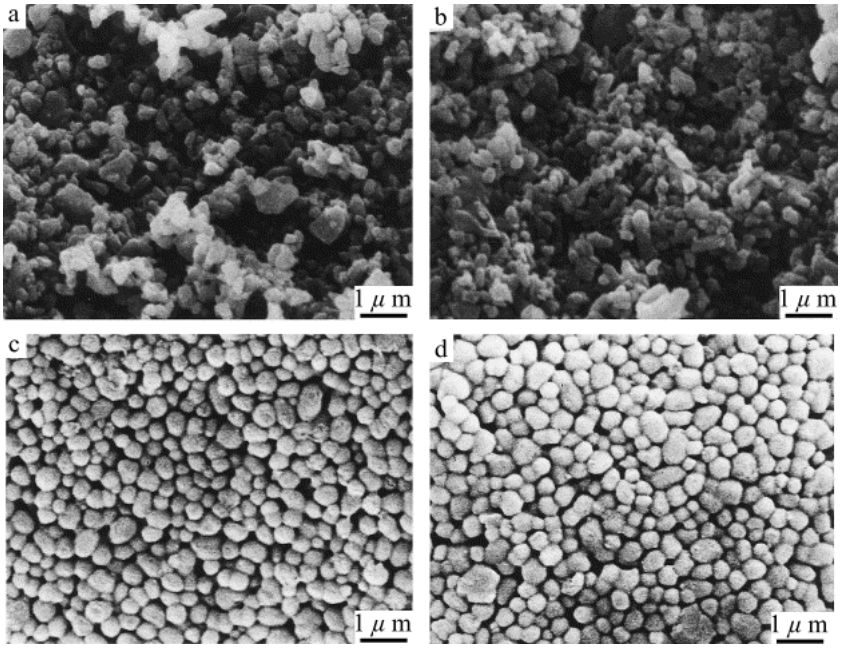

Figure II.10 : The SEM micrographs for the compacts with elongated shape alumina (a) and (b), and spherical shape of alumina particles (c) and (d).
[shui2002origin]

Figure II.10 shows the SEM micrographs for the two types of alumina particles.
In section II.5, the origins of anisotropic behaviour of compacts and ceramics during sintering process are briefly explained. The presented cases are just representative of numerous researches carried out for understanding the anisotropic shrinkage of ceramics. In general, the forming processes and the microstructural properties of materials are responsible for the anisotropy during firing stage of production.
Next section is devoted to a literature review on densification behaviour of ceramic core materials.

II.6 Sintering of silica based ceramic cores

II.6.1 Introduction

Investment casting process is usually used for making complex shaped mechanical parts and structures. In order to produce hollow and complex-shaped components by this process, special cores with complex design are required. There are two options for manufacturing investment casting cores: using soluble wax or using sacrificial ceramic cores.
Soluble wax cores are designed to melt out with the rest of the wax pattern, whereas ceramic cores remain part of the wax pattern and are removed after the workpiece is cast [degarmomaterials].
The ceramic cores used for manufacturing superalloy gas turbine components have been previously fabricated by injection molding process or rapid prototype printing [bagchi1991intelligent]. The investment casting core must be made from a material that exhibits the following properties:

- Chemically compatible with the metal
- Good crushability for removal after casting

- Resistant to thermal shock
- Resistant to dimensional changes

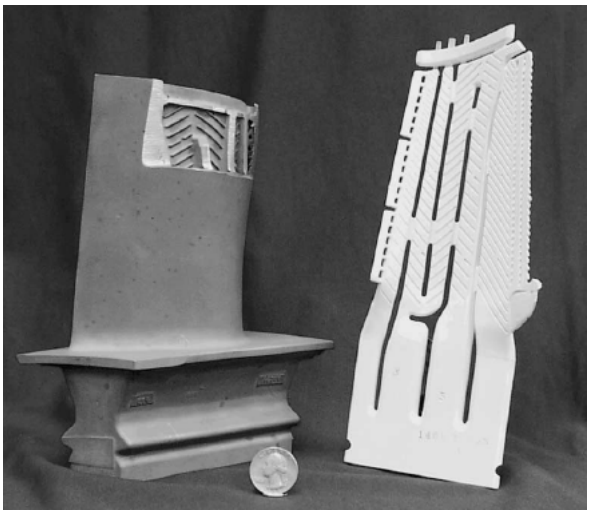

Figure II.11 : A sectioned turbine blade made of superalloy (left) and the corresponding ceramic core (right) used for shaping the complex interior of the blade.
[wereszczak2002dimensional]

Silica based ceramic materials with specific additives generally exhibit the above desired properties.
Figure II.11 shows the usage of ceramic cores in manufacturing of gas turbine components where complex internal structures are needed.

II.6.2 Dimensional changes of ceramic cores during sintering

As mentioned before, a ceramic core material should possess good crushability and high resistance to thermal shock and low dimensional changes during the investment casting process. In other words, an optimum compromise between crushability and thermal stability is necessary. As a result, investigating high temperature deformation and creep performance of the ceramic cores seems to be essential.
Wereszczak *et al* have studied the dimensional changes and creep of silica core ceramics [wereszczak2002dimensional].

Material	Silica	Zircon	Alumina	Initial cristobalite (%)	Final cristobalite (%)
I	74	24	1	8	35
II	93	3	4	13	57

Table II.1 : Chemical composition ($wt\%$) of studied materials with cristobalite contents before and after 30 min at $1530°C$.

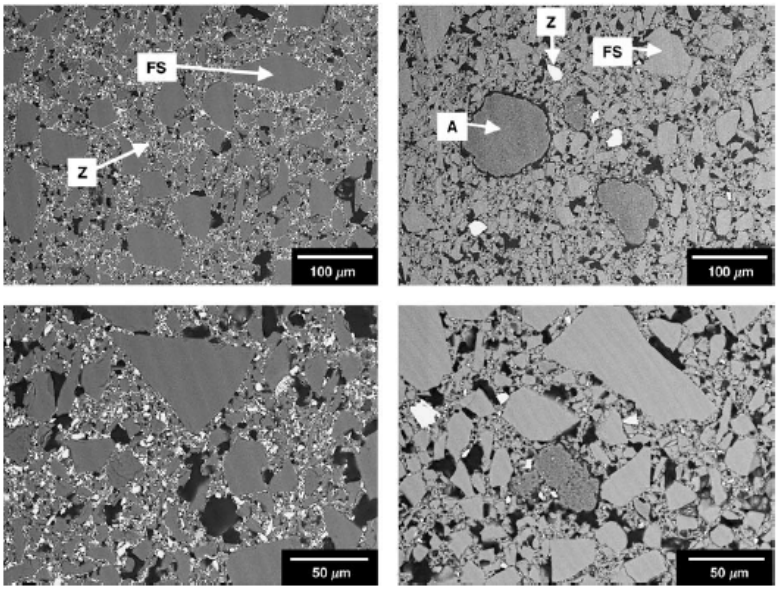

Figure II.12 : SEM micrographs of ceramic cores before thermal treatment at different magnifications. A=alumina, FS=fused silica, and Z=zircon (Left: Material I and right Material II).

[wereszczak2002dimensional]

For this purpose, they have examined two silica-zircon ceramic materials with two different chemical compositions (shown in table II.1) containing silica (SiO_2), zircon ($ZrSiO_4$) and alumina (Al_2O_3).

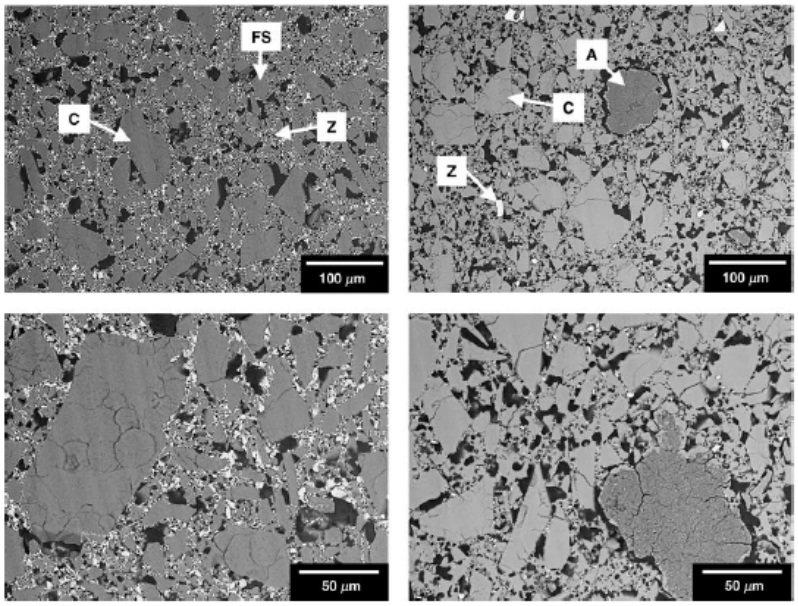

Figure II.13 : SEM micrographs of ceramic cores after creep test at $1530°C$ and 6.21 MPa. A=alumina, C=cristobalite, FS=fused silica, and Z=zircon (Left: Material I and right Material II).

[wereszczak2002dimensional]

The microstructure of studied materials as received is presented in figure II.12. Material

I consists of high content of zircon and fused silica grains with some cristobalite in a fine and porous silica-zircon matrix before the creep test. In addition to these phases, material II contains alumina agglomerates too. Both materials are sintered according to the same sintering cycle.
Figure II.14 shows the dimensional change of samples during the sintering process. Apparent specimen length have been obtained after subtracting the load-train thermal expansion.

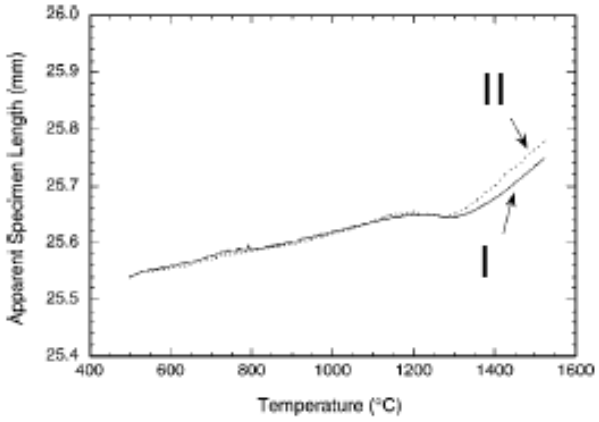

Figure II.14 : Dimensional change of specimens during sintering.
[wereszczak2002dimensional]

As illustrated in figure II.14, both samples show a relatively low thermal expansion. Some important information can be obtained from these curves. The decrease in apparent specimen lengths observed between $1100°C$ and $1300°C$ is probably related to the viscous flow sintering with the start of cristobalite formation around $1300°C$ [huseby1979high, wereszczak2002dimensional].
Wereszczak *et al* and Huseby *et al* concluded that subsequent cristobalite formation during heating stage of sintering dominates the total contraction in fused silica based ceramic cores. Furthermore, the silica-zircon ceramic exhibits less contraction than the high silica core materials for a given test conditions [huseby1979high, wereszczak2002dimensional].
Based on these results, it seems necessary to present a brief literature review on the phase transformation of vitreous silica powders to cristobalite. It seems that the presence of the zircon can influence the dimensional change of ceramic core materials during sintering. In the next two sections, these two phenomena are discussed with regard to ceramic core materials.

II.6.3 The influence of cristobalite on the crystallization of fused silica

The properties of ceramic cores have to be finely adjusted in order to produce parts with precise dimensions by investment casting of nickel and cobalt superalloys. The ceramic core manufacturers frequently add different amounts of cristobalite to their products. Researches have been carried out for studying the influence of cristobalite on the fused silica ceramic cores.
Kato *et al* suggested that the silica based ceramic core material with $10-20$ wt% cristobalite can be used for the oriented solidification casting as it can hinder the softening and the shrinkage of the core at high temperature [kato63ceramic, kato1990ceramic].
Takayanagi *et al* reported that the crystallization control of fused silica influences the hot deformation of the ceramic core during investment casting [takayanagi1988crystallization].
Mild *et al* have studied the relationship between the bend rate of ceramic cores at 1150° C and

the cristobalite content. They have reported that cores with a very low level of cristobalite exhibit poor refractoriness [mild1979].
In another study, Wang *et al* have investigated the effect of cristobalite particles on the crystallization of fused silica ceramic core [wang1995effect]. For this purpose, they have studied two kinds of ceramic core specimens with the following compositions:

- 100 wt% fused silica
- 80 wt% fused silica + 20 wt% cristobalite

Figure II.15 shows the transformation rate of cristobalite as a function of time and of the initial core composition at 1350° C. According to this graph, the transformation rate is independent of composition at low temperature. However, at high temperature (more than 1325° C) the initial cristobalite content influences the transformation rate.

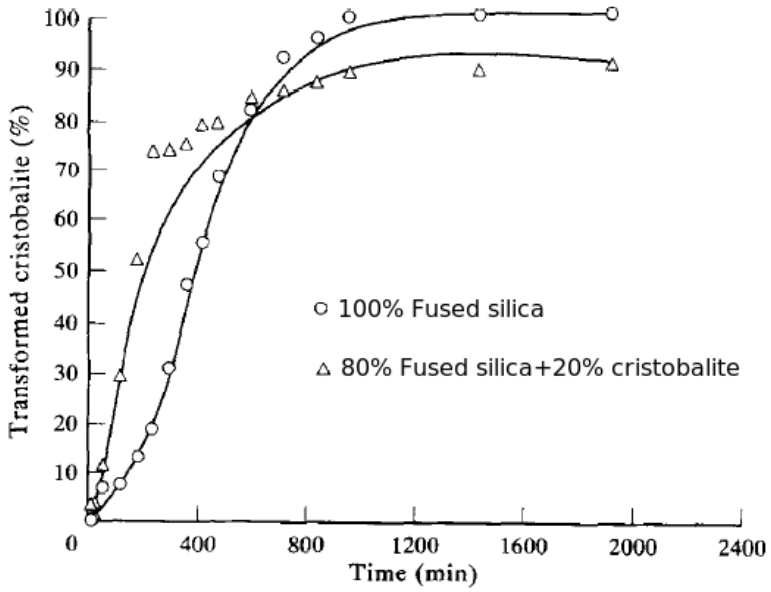

Figure II.15 : Quantity of crystallized cristobalite as a function of time and of the initial core composition at 1350° C.
[wang1995effect]

Figure II.16 illustrates the effect of cristobalite particles on the crystallization of fused silica. Two initial cristobalite particles are surrounded by fused silica fine powders at the primary state of raw materials (figureII.16(a)). During the reaction state of process (figureII.16(b)), a compressive stress is applied on the fine fused silica particles. This compressive stress field is the result of a sudden volume expansion during the cristobalite transformation from α phase to β phase at elevated temperature [wang1995effect].

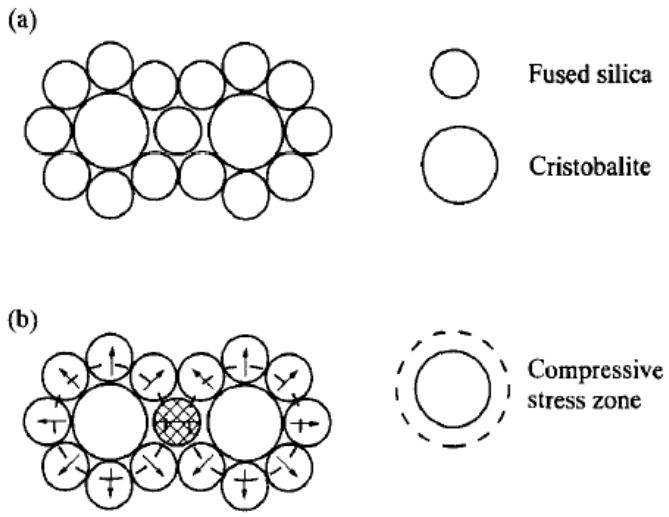

Figure II.16 : The effect of cristobalite on fused silica at initial state of materials (a), and at reaction state of products (b).
[wang1995effect]

In order to better understand the effect of cristobalite particles on transformation rate, another test has been developed which is shown in figure II.17. In this experiment, the transformation rates of cristobalite are measured inside surface layer (FSI) and outside surface layer (FSO). The inside surface layer represents the surface which is in contact with the cristobalite particles. Similarly, the outside surface layer is not in contact with cristobalite particles. Based on the results obtained in this test, the crystallization rate of cristobalite in the outside layer is 15% lower than in the outside layer.

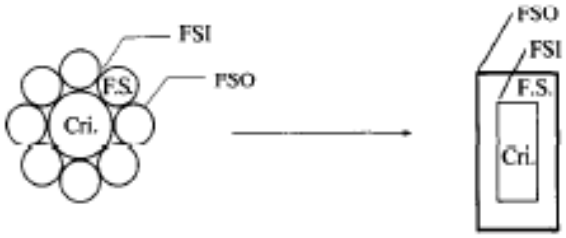

Figure II.17 : Simple model showing the effect of cristobalite on fused silica.
[wang1995effect]

In other words, this experiment demonstrates the inhibition effect of compressive stress field produced during the phase transformation of cristobalite from α phase to β phase at high temperature [wang1995effect].
In conclusion, the presence of cristobalite particles in initial raw materials can influence the transformation rate in two ways:

- At initial stages, cristobalite particles increase the effective free surface and nucleation sites. As a result, they enhance the crystallization of fused silica.
- At elevated temperatures, the compressive stress field due to sudden volume expansion of cristobalite delays the transformation rate.

II.6.4 Influence of zircon

Zircon, or zirconium silicate ($ZrSiO_4$), is an extremely common additive used in the investment casting industry. It is used in ceramic core formulations as well as a face coat for the shell materials that are also used for investment casting [jones2002effect, wilson2011role]. Zircon is useful for investment casting due to its low thermal expansion ($4.1 \times 10^{-6\circ}C^{-1}$ between $25^\circ C$ and $1400^\circ C$), its low heat conductivity ($5.1\ Wm^{-1\circ}C^{-1}$ at $25^\circ C$ and $3.5 Wm^{-1\circ}C^{-1}$ at $1000^\circ C$) and its lack of phase transformations up to $1687 \pm 7^\circ C$ [shi1998synthesis, wilson2011role].
In addition, zircon, as a phase transformation inhibitor, can influence the crystallization rate of fused silica into cristobalite. As mentioned before, the compressive stress due to lattice distortion of cristobalite can also delay the crystallization of cristobalite [mild1979, wilson2011role].
The role of zircon on the properties of silica-zircon ceramic cores has been studied by Wilson *et al* [wilson2011role]. They have investigated the effect of zircon particles on high temperature consolidation of silica-zircon ceramic materials and the crystallisation of fused silica.
According to their study, zircon act as a Zener pinning agent at high temperature and applies a pinning force at the grain boundaries which prevents consolidation and high temperature shrinkage of silica-zircon ceramic materials. In other words, zircon as a non-reactive secondary phase particles prevents grain boundary movement by introducing a drag force at the grain boundaries (F_d):

$$F_d = \frac{3 f_\nu \nu_b}{2r} \tag{II.55}$$

This force depends on the amount of secondary phase (f_ν is the volume fraction of the secondary phase) and on the surface energy of the secondary phase (ν_b). In equation II.55, r is the average particle radius of the secondary phase [wilson2011role, kang2005sintering].

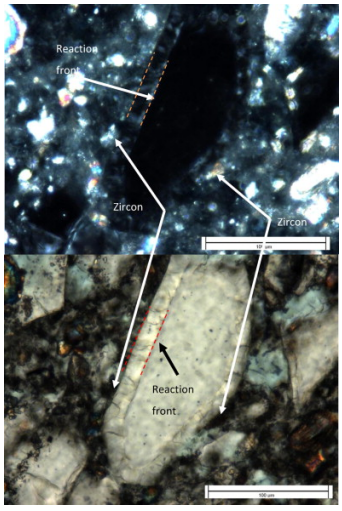

Figure II.18 : Crystallisation of a large silica grain (a) in plain polarised light and (b) in cross polarised light with a 1/4 wavelength advance, both 50x magnification.
[wilson2011role].

Wilson *et al* have also studied the effect of zircon on cristobalite transformation during sintering of silica-zircon ceramic materials. Figure II.18 shows the growth front of a large silica grain in presence of zircon. However, no difference in the morphology of the growth

front is detected. According to their observations, they suggest that zircon is only a nucleator or the crystallisation was not influenced by the zircon surface [wilson2011role].

II.7 Conclusion

This chapter presents a literature review of different constitutive models of sintering. Firstly different modelling methods (microscopic, mesoscopic, macroscopic) have been discussed. Then the continuum mechanics approach to sintering problem has been explained. Afterwards, different constitutive models of sintering using phenomenological approaches have been presented in detail.
A brief literature review of anisotropic densification behaviour during sintering follows, since in chapter IV, an anisotropic model is proposed for densification behaviour of slip cast ceramics.
Finally, a short literature review on sintering silica based ceramic core materials is presented in order to better analyse the results obtained in chapter V.

Summary in French

Dans ce chapitre une étude bibliographique des différentes lois de comportement de matériaux lors du frittage a été brièvement exposée.
D'abord les différentes approches (microscopique, mésoscopique et macroscopique) ont été expliquées. Ensuite les principes de mécanique de milieu continu en frittage ont été presentés. Les aspects phénomenologiques des simulations du frittage ont été évoqués en détail.
Ensuite, les origines de comportement anisotrope des céramiques lors du frittage sont abordées afin de créer une base bibliographique pour expliquer les résultats de chapitre IV.
Finalement, le comportement des noyaux céramiques à base de zircon-silice est présenté pour pouvoir mieux analyser les résultats obtenus dans le chapitre V.

Chapter -III-

Experimental techniques for determining mechanical parameters of the continuum sintering model

Contents

III.1 Introduction

This chapter is dedicated to the measurement techniques actually being used for determining the physical or mechanical parameters of the sintering constitutive model. First, some literature for determining sintering potential, viscosity and Poisson's coefficient will be reviewed. Then the main experimental methods used in this work for identifying materials parameters will be discussed.
Since this research work has been performed in collaboration with industry , all the efforts have been made to propose practical as well as **economical** experimental methods to our industrial partners which allow them to develop the same test platforms in their laboratories. With this aim, thermo-mechanical analysis (dilatometry) has been extensively used in order to determine the parameters of the sintering model. On the other hand, in order to identify the mechanical parameters of the model, a brand new test platform "*Sinter- bending*" as well as a new concept of "*Pyroplasticity*" have been developed.

III.2 Some sintering parameters and their measurement techniques

Thermo-mechanical behaviour of ceramics during sintering can be simulated by one of the constitutive models presented in chapter II. All these models consist in some characteristic properties of material known as continuum mechanical parameters which have to be measured experimentally. In this section, a brief literature review on sintering related parameters and on the experimental techniques used for measuring these parameters are being discussed.

III.2.1 Sintering potential

The first step in stress analysis and strain rate measurement during sintering consists in selecting a constitutive model which links the applied load to resulting deformation rate. For an elastic material, this model is defined by two components ; shear modulus (G_v) and volumic modulus (K_v). For an isotropic linear elastic material, the constitutive model takes the following form:

$$\varepsilon_x = \varepsilon_{sr} + \frac{1}{E}(\sigma_x - \nu(\sigma_y + \sigma_z)) \tag{III.1}$$

In equation III.1 ε_x, is the strain along the x direction, σ_x, σ_y and σ_z are the principal stresses along x, y and z directions respectively, E is the Young modulus, ν is the Poisson's ratio and ε_{sr} is the free sintering strain. G_v and K_v are functions of Young's modulus and Poisson's ratio:

$$G_v = \frac{E}{2(1+\nu)} \tag{III.2}$$

$$K_v = \frac{E}{3(1-2\nu)} \tag{III.3}$$

For an isotropic incompressible linear viscous material, the constitutive model is analogous to equation III.1. It can be obtained by substituting strain with strain rate, E with 3 times deviatoric viscosity and ν by 0.5:

$$\dot{\varepsilon}_x = \dot{\varepsilon}_{sr} + \frac{1}{3\eta}(\sigma_x - 0.5(\sigma_y + \sigma_z)) \tag{III.4}$$

For a porous material, equation III.4 should be modified in order to take into account the compressibility of porosity:

$$\dot{\varepsilon}_x = \dot{\varepsilon}_{sr} + \frac{1}{E_m}(\sigma_x - \nu_m(\sigma_y + \sigma_z)) \tag{III.5}$$

By setting the principal strain rates to zero and assuming $\sigma_x = \sigma_y = \sigma_z = \Sigma$ in equation III.5, the sintering potential can be obtained as:

$$\Sigma = -\frac{E_m \dot{\varepsilon}_{sr}}{1 - 2\nu_m} \tag{III.6}$$

Equation III.6 can be used for the experimental determination of the sintering potential which depends on microstructural aspects (grain size, pore size) and thermodynamical factors (surface energy, grain boundary energy).
In the following table, some examples of sintering potential of different materials are presented.

The sintering potential can be illustrated as the uniaxial sintering stress as a function of

Material	**Sintering Potential**
Sub-micron oxide (Alumina)	few MPa
Nanocrystalline oxide (zirconia)	100 MPa
LTCC [1]	0.1 MPa

Table III.1 : Sintering potential examples of different materials.
[green2008constrained]

different factors like density, grain size, etc. [green2008constrained, svoboda1994equilibrium, kanters2001cosintering, raj1987analysis, zuo2005continuum, guillon2007effect]

III.2.2 Sintering viscosity

The sintering viscosity is defined as the slope of the linear curve between the uniaxial sintering stress and uniaxial strain rate.
For determining this term, in equation III.5, the stresses should be set to $\sigma_y = \sigma_z = 0$:

$$E_m = \frac{\sigma_x}{\dot{\varepsilon}_x - \dot{\varepsilon}_{sr}} \tag{III.7}$$

[cai1997determination,mohanram2005densification,chang2007uniaxial,zuo2003experimental, ollagnier2007effect, zuo2004temperature, ostrowski1999evolution]

III.2.3 Viscous Poisson's coefficient

The viscous Poisson's coefficient is defined through equation III.5:

$$\nu_m = \frac{\dot{\varepsilon}_y - \dot{\varepsilon}_{sr}}{\dot{\varepsilon}_{sr} - \dot{\varepsilon}_x} = \frac{\dot{\varepsilon}_z - \dot{\varepsilon}_{sr}}{\dot{\varepsilon}_{sr} - \dot{\varepsilon}_x} \tag{III.8}$$

Figure III.1 represents the evolution of viscous Poisson's ratio as a function of relative density for three different materials [mohanram2005novel, ollagnier2007effect, salamone2003effect].

[1] Low temperature co-fired ceramic

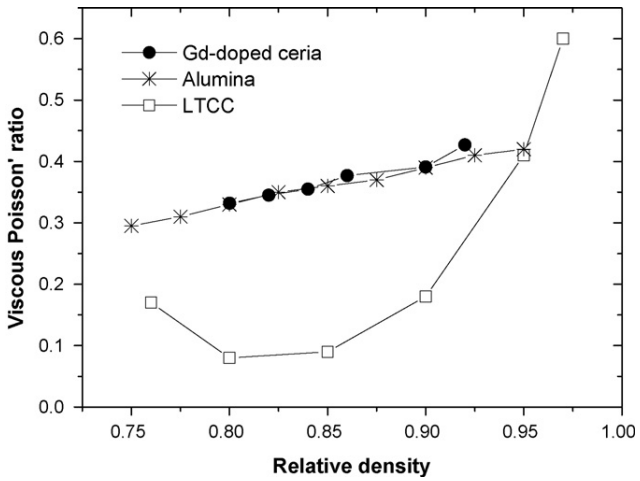

Figure III.1 : Viscous Poisson's ratio as a function of relative density for three different materials.

[green2008constrained]

III.2.4 Curvature measurement

Dimensional instabilities during the firing process of ceramic films and coatings as well as low temperature co-fired ceramics (LTCC) and solid oxide fuel cells (SOFC) appear as a curvature of sintered plates.
Geometry control in SOFC and LTCC components are of highest importance. Many LTCC components, which are used in the microelectronic industry, are sensitive to structural distortion and warpage during sintering. These LTCC components are usually composed of different ceramic layers. As each layer possesses its own densification rate, stresses and warpage arise during sintering, which can be intensified by different expansion coefficients of the layers. These incompatibilities can induce curvature, delamination, cracking and finally warpage of the sintering part.

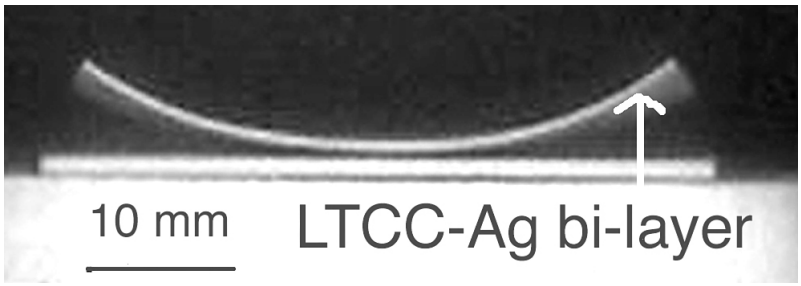

Figure III.2 : Distortion of a bi-layered LTCC during sintering.
[green2008constrained]

The curvature occurring during the firing process can be measured by sophisticated high temperature instruments such as high temperature optical dilatometer or high temperature optical microscope.
In order to measure the shape changes mentioned above which can occur during sintering, an instrument called fleximeter can be used. Some experimental measurement techniques can be developed by combining different thermal measurement apparatus with high temperature laser detectors or optical detection systems. Figures III.3 and III.4 illustrates two mixed techniques for measuring the deformation of glass-ceramics and porcelains during firing

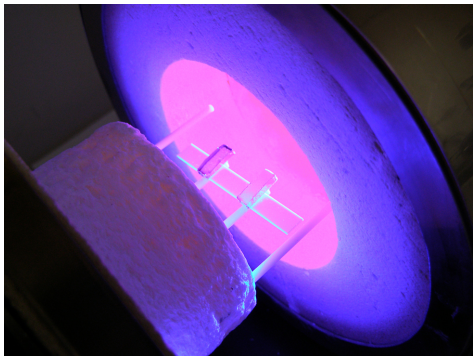

Figure III.3 : Optical dilatometer measuring the deformation of a glass-ceramic. [PaganelliVenturelli09]

process, respectively. This apparatus combines optical techniques (for deformation detection)

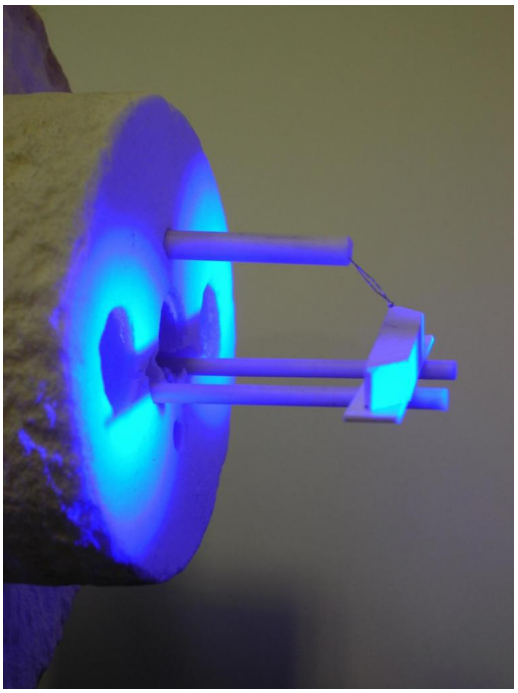

Figure III.4 : Optical dilatometer measuring the deformation of a porcelain. [PaganelliVenturelli09]

with thermal techniques (dilatometry) in order to register the change in shape of ceramics during the firing process.
In this section, experimental techniques for measuring ceramics deformation during sintering process have been discussed briefly. This chapter will further be interested in the experimental techniques used in this research for determining the sintering model coefficients.

III.2.5 Monitoring of the sintering process

The sintering process of ceramics and powder metallurgy parts can be done by measuring the bulk properties such as density, microstructural parameters such as neck size and mechanical properties such as hardness [german2005powder]. However, in situ measurement techniques seem to be the most valuable.

In this section, a literature review on the in situ video-imaging technique used for monitoring the sintering process is reported.
Blaine *et al* have developed a video-imaging technique using synchrotron system which inspired us for developing the sinter-bending test used in our research [blaine2005critical].

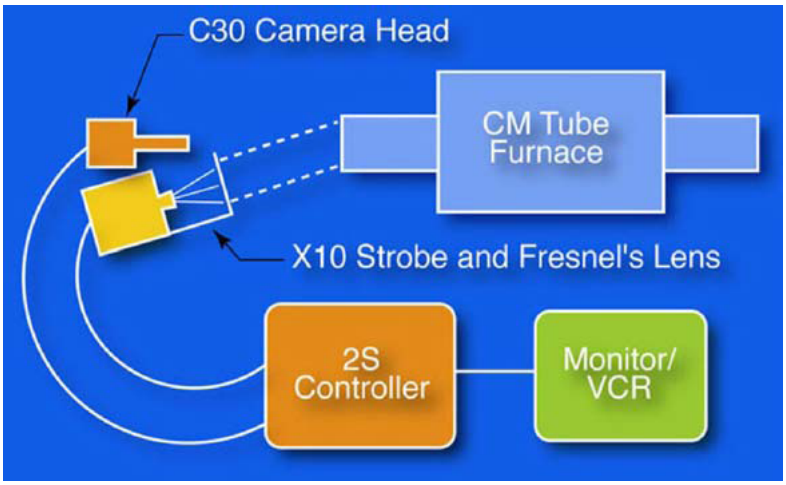

Figure III.5 : In situ video-imaging using synchrotron system.
[blaine2005critical]

Figure III.6 shows a schematic of in situ video-imaging using synchrotron system. By using this measuring system, Blaine *et al* have monitored the in situ deflection of 316L beam during sintering cycle:

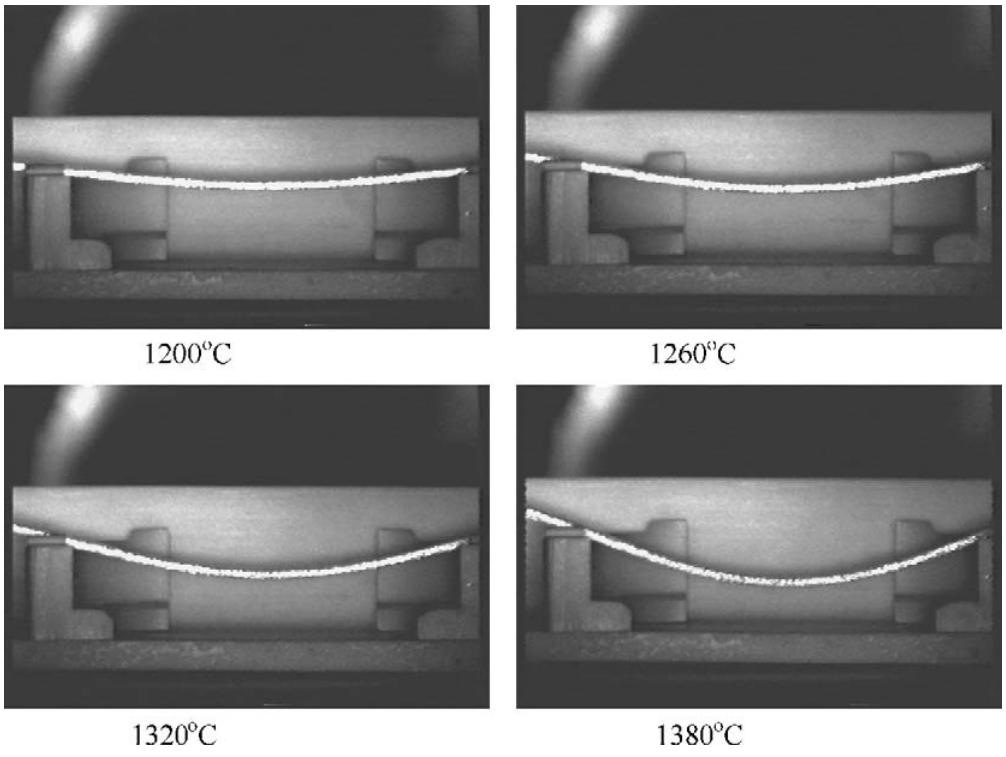

Figure III.6 : In situ bending pictures of 316L with 0.2% boron showing beam deflection at different temperatures along the sintering cycle.
[blaine2005critical]

The apparent viscosity can be determined through in situ video-imaging of a bending beam during sintering and eventually can be used for determining the parameters of constitutive model [blaine2005critical].

III.3 Densification behaviour analysis: Dilatometry

The continuum mechanical parameters for sintering are usually obtained by measuring strain rates at a given applied stress.
Current equipment being used in this research for determining the dimensional changes of porous materials is a vertical connecting rod (push rod) dilatometer which has a resolution of about 2 μm for a cylindrical specimen of 20 mm height and 12 mm diameter. In this apparatus, while the sample is placed in a furnace, a connecting rod transfers the thermal deformation (shrinkage) to a strain gauge (LVDT) which measures the displacement (figure III.7). The sample is normally placed on a matched low-expansion material (here: rigid

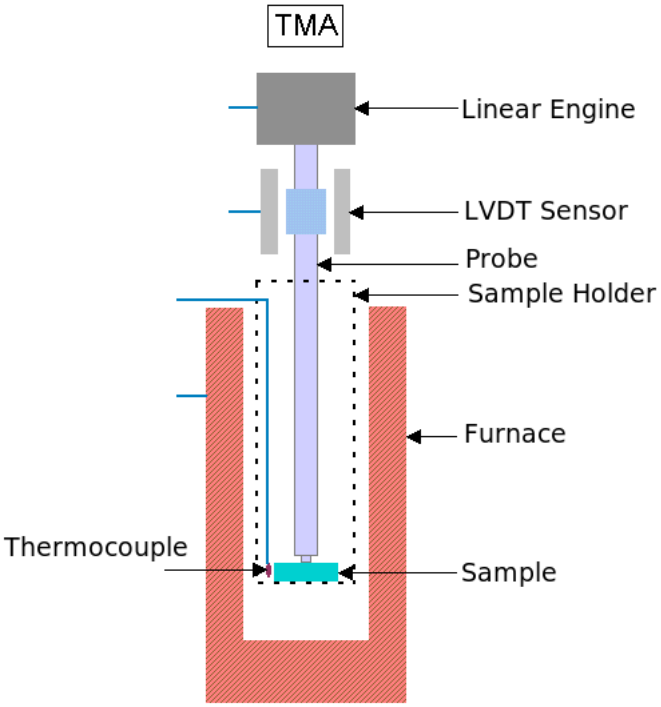

Figure III.7 : Vertical connecting rod (push rod) dilatometer used for thermo-mechanical analysis.

alumina plates) and on the other side is in contact with the connecting rod. To reduce the effect of friction and guarantee uniaxial stress state in the specimen high temperature lubricant such as boron nitride can be used.
The dilatometric test measures the length variation of powder compacts as a function of temperature. Figure III.8 shows the relative dimensional change (linear shrinkage: $\frac{L-L_0}{L_0}$) as a function of temperature. L_0 is the initial length of specimen and L is the length of the sample at temperature T. As shown in figure III.8, the length of specimen increases during heating phase, then at a given temperature a drop can be noticed. Finally it stabilizes and its length increases again. The first rise is associated with the dilatation of the sample during heating phase of sintering cycle. Follows a significant drop which corresponds to the densification of material (sintering shrinkage).

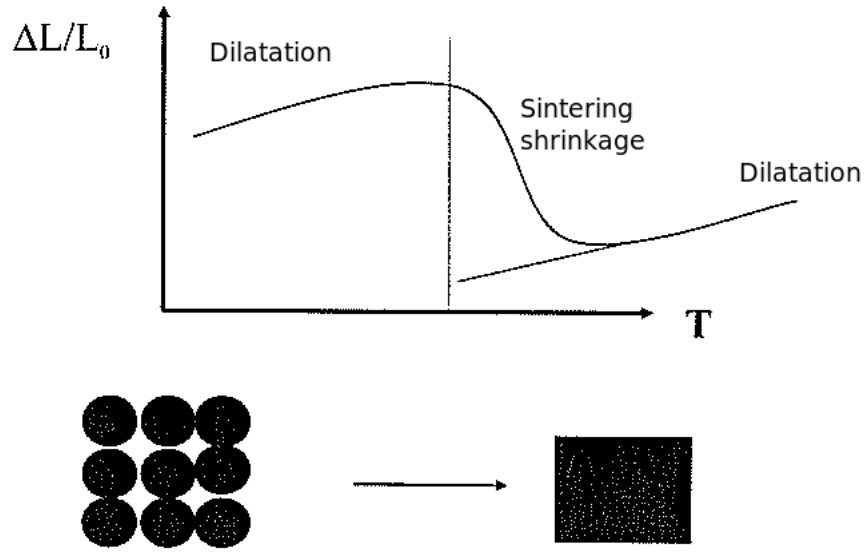

Figure III.8 : Typical densification curve as a function of temperature. [fantozzi2011science]

The increase in material density is the consequence of two processes: soldering of the grains and elimination of the porosity confined by the grains. Grains soldering during sintering does not increase the relative density automatically [fantozzi2011science].
The specific surface of the powder is the free surface developed by entire grains. The specific powder surface decrease can be associated with either the soldering of grains or the grain growth (figure III.9).

During grain growth, the total number of grains decreases whereas the average size of the grains increase. Consequently, the simple sintering demonstration is a drop in the surface of specimen as well as its cohesion increase under the effect of temperature due to intergranular bonding.

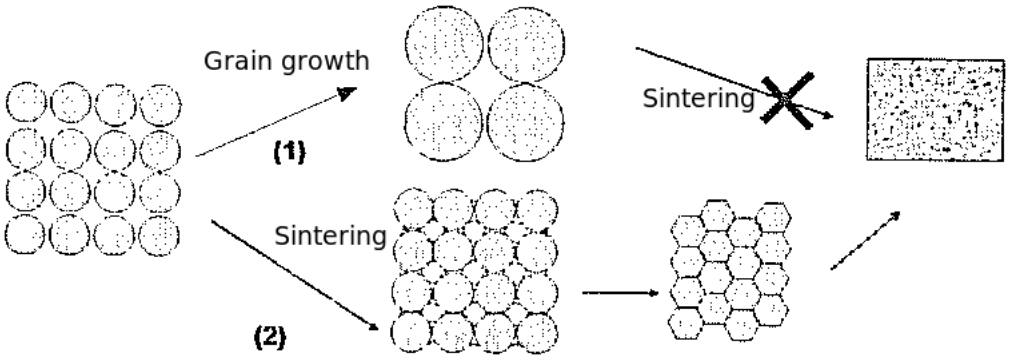

Figure III.9 : Different morphological changes of a dissipated system during heat treatment. [fantozzi2011science]

The thermo-mechanical analysis curve (figure III.8) reveals valuable information and provides data for numerical simulation of sintering. From densification curve, the sintering

strain rate which depends on porosity and temperature can be obtained. Moreover, the thermal expansion coefficient of material can be calculated from the slope of the densification curve during heating or cooling phase.

$$\alpha_L = \frac{1}{L}\frac{dL}{dT} \qquad and \qquad \varepsilon_{th} = \frac{L - L_0}{L_0} = \alpha \Delta T \tag{III.9}$$

In order to study the kinetics of sintering, dilatometric tests can be done by applying different loads as well as different sintering cycles. In this study, all the thermo-mechanical experiments have been performed by using the Setaram vertical dilatometer able to reach a temperature of 1450°C and a load of $150g$.
Obtaining reliable data from this equipment requires laborious attention to minute details. Since the connecting rod is exposed to the same temperature as the sample and thereby expands, a relative value is obtained, which must be corrected afterwards. In other words, for every sintering cycle two conditions should be tested. A first test with sample followed by a second test without sample. The thermal deformation curve obtained from the tests with sample consists in: sample shrinkage, rigid substrate expansion as well as connecting rod thermal expansion. However, the second experiment just measures the thermal deformations of rigid substrate and connecting rod. In order to obtain the pure shrinkage curve of porous sample, the following corrective operation should be done:

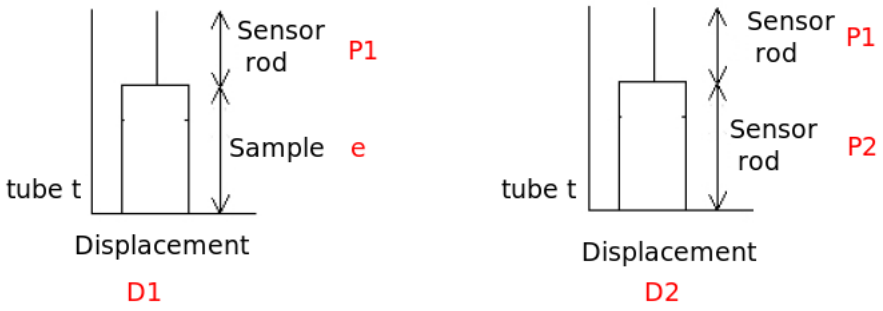

Figure III.10 : Correction procedure for densification analysis by dilatometry.

For the first test with specimen:

$$D_1(T) = P_1.C_r(T) + e.C_s(T) - t.C_t(T) \tag{III.10}$$

$D_1(T)$ is the total displacement (with sample), $C_r(T)$, $C_s(T)$ and $C_t(T)$ are the coefficients of thermal expansion of the connecting rod, the sample and the tube, respectively.
For the second test without specimen:

$$D_2(T) = P_1.C_r(T) + P_2.C_r(T) - t.C_t(T) \tag{III.11}$$

So

$$D_1(T) - D_2(T) = e.C_s(T) - P_2.C_r(T) \tag{III.12}$$

$$D_1(T) - D_2(T) = e.C_s(T) - e.C_r(T) \tag{III.13}$$

$$e.C_s(T) = D_1(T) - D_2(T) + e.C_r(T) \tag{III.14}$$

As a result, this test is very sensitive and small deviations from the above rules can produce erroneous data and, consequently an inaccurate numerical simulation.

In order to determine the viscous parameters of the model, a novel experiment has been developed which is described in the following section. A term called *"pyroplasticity"* has been also introduced as a characteristic of materials.

III.4 Pyroplastic behaviour analysis

III.4.1 Introduction

The constitutive models used for simulating the deformation of powder compacts at high temperature consist in a thermal (sintering) and a mechanical part. Each part has a set of coefficients which should be determined by experiments. The parameters associated with the sintering can be obtained by dilatometric densification tests. However, in order to determine the mechanical parameters (volumetric viscosity K and deviatoric viscosity G) of the sintering constitutive model, a new test device called *sinter-bending* has been developed. First of all pyroplasticity should be defined.

III.4.2 Pyroplasticity

The pyroplastic deformation is the bending of a ceramic specimen caused by gravity during heat treatment (figure III.11). It is similar to the loss of a shape of a product during the firing process. Pyroplasticity is related to liquid phases of low viscosity formed during firing. The pyroplastic deformation occurs more frequently in highly vitrified pastes like porcelain tiles [bernardin2006pyroplasticity].

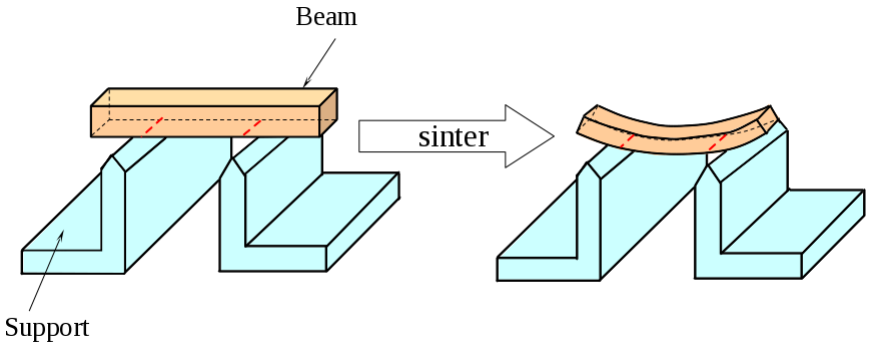

Figure III.11 : Demonstration of pyroplastic behaviour of powder compacts.

The pyroplastic deformation magnitude is determined by the pyroplastic index (PI), pointing out the tendency to deformation of a specimen submitted to gravity during its firing under specific conditions. The procedure used to determine the pyroplasticity index consists in measuring the curvature of a specimen during its firing over two refractory supports [bernardin2006pyroplasticity].

$$PI = \frac{sb^2}{l^4} \tag{III.15}$$

where s is the maximum deformation (cm), b is the bar thickness (cm) and l is the distance between supports (cm).

III.4.3 Sinter-bending test platform

Pyroplasticity can be considered as the deflection of a green ceramic beam during sintering. Therefore, the pyroplastic behaviour can be illustrated as the bending curve of a ceramic beam as a function of temperature or time. In order to measure continuously the deflection of ceramic beams during firing process, a special sinter-bending test platform has been designed and developed.

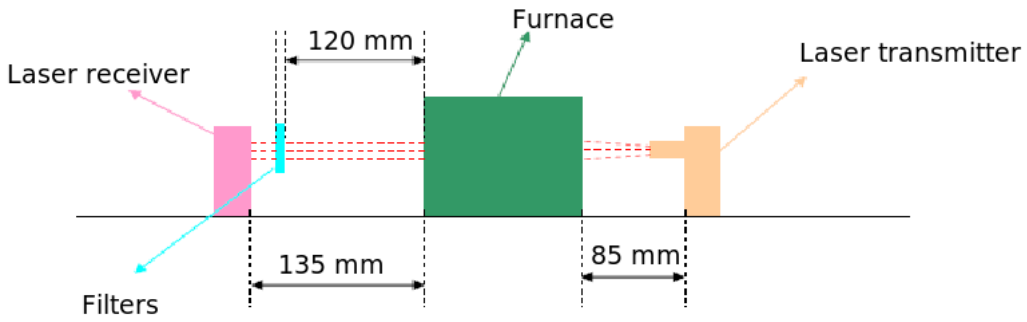

Figure III.12 : Sinter-bending test device.

As illustrated in figure III.12, the sinter-bending test device is equipped with a laser assisted bending measurement system which measures the deflection of the ceramic beam under its own weight during heat treatment. In this apparatus the following materials have been used:

- Laser: Mitutoyo LSM 406V -1mW - 760nm
- Resolution: Gain=10$mV/50\mu m$ and response range=$\pm 5V/25mm$
- Filter: IR cut off
- Furnace: Resistance furnace with 6 heating elements ($MoSi_2$), power 2100W, insulated by alumina fibre boards, water cooling system

The sample is a ceramic beam (cantilever or simply supported structure) placed in the center of the furnace. A laser beam monitors continuously the deflection during sintering through the small slits arranged in the wall of the furnace (figure III.13). The measured deflection data are then transferred to a data processing system in order to extract the deflection curves as a function of time or temperature by the labview program. Furthermore, these curves have been used for identifying the parameters of the sintering model.
At sintering temperatures the green ceramic beam becomes soft and consequently bends under gravity. The criteria used for identifying the creep model parameters can be the maximum deflection of ceramic beam. The initial geometry selected for this purpose was a simply supported beam as shown in figure III.11. The structure assembled in figure III.11 consists in a green ceramic beam laid on two rigid, dense alumina supports. The entire structure is exposed to high temperature sintering cycle during which the beam densifies and bends simultaneously due to its weight.

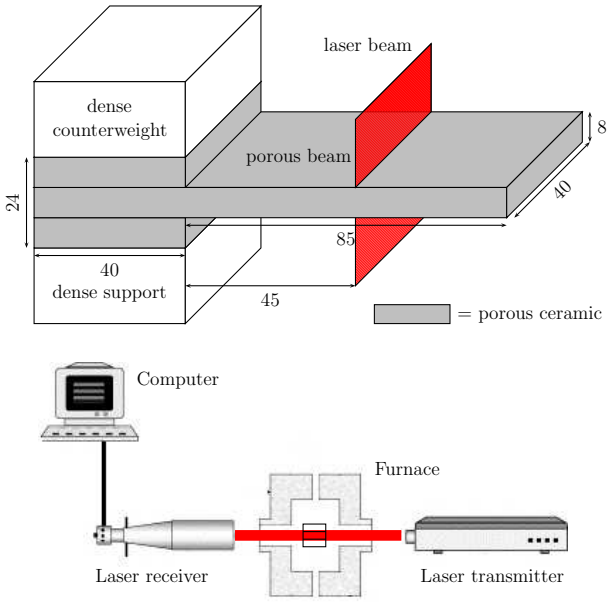

Figure III.13 : Laser assisted deflection measuring apparatus.

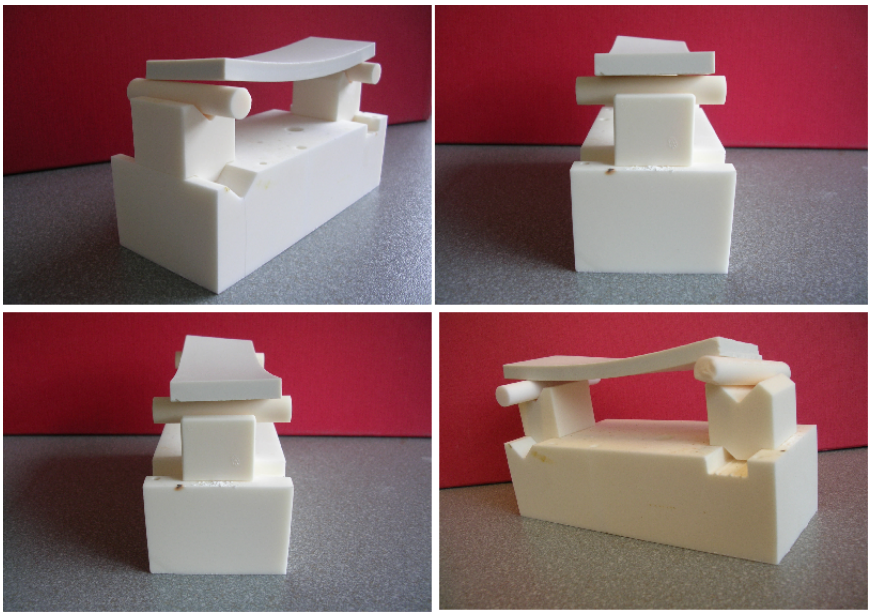

Figure III.14 : Technical problems during sinter-bending experiment of simply supported beam.

The furnace used for firing this structure operates under air atmosphere. The results of first experiments are shown in figure III.14. The green ceramic (alumina) beam has been laid on rigid cylindrical supports and the entire structure has been sintered at 1450°C under air. The contact between the porous plate (beam) and dense ceramic supports affects the final result. As presented in figure III.14, even after using lubricant (boron nitride) in order to reduce adhesion and friction at the contact surfaces, ceramic beam sticks to the cylinder supports during firing process. This phenomena can lead to warping of the beam. The friction between all these surfaces impedes sliding of cylinder supports.
In order to avoid the problem of contact, a cantilever beam structure has been used (Figure

III.15).

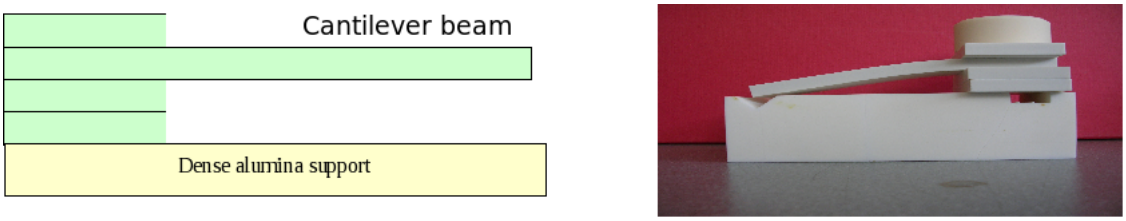

Figure III.15 : Technical problems during sinter-bending experiment of simply supported beam.

In this new structure, as shown in figure III.15, the deflection of a cantilever plate is measured during the sintering. A green ceramic beam has been maintained by two small pieces of the same non-sintered ceramic material. Consequently, there is no contact problems between two different surfaces during sintering. Figure III.15 also shows the entire cantilever structure after sintering.
Finite element geometry and simulation of cantilever sinter-bending test have been presented in figure III.16.

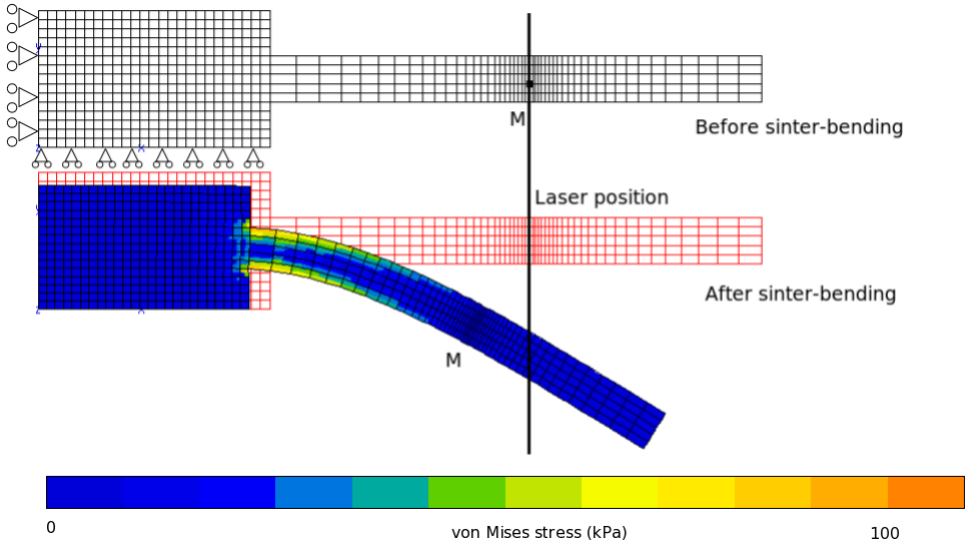

Figure III.16 : Finite element simulation of sinter-bending test.

As shown in figure III.16, the laser beam which measures the bending of the ceramic beam is fixed (point M in figure III.16). On the other hand, as the structure undergoes thermal treatment, the initial point M moves horizontally (due to sintering shrinkage) and vertically (deflection). Consequently, the beam deflection measured by the laser beam does not correspond to the displacement of a given finite element node. Therefore, a post-processing routine was written to mimic the laser beam measurement. In this corrective post processing, the numerically calculated displacement will be modified according to the equations III.16 and III.17:

$$U_1 = U_1^L + \left(\frac{X - X^L}{X^R - X^L}\right)\left(U_1^R - U_1^L\right) \tag{III.16}$$

$$U_2 = U_2^L + \left(\frac{X - X^L}{X^R - X^L}\right)\left(U_2^R - U_2^L\right) \tag{III.17}$$

In these equations X is the laser position, U_1 and U_2 are the corrected displacements, X^L and X^R are the positions of two nodes on the left and right sides of the laser position (node M in figure III.16), and finally U^L and U^R are their displacement respectively.

III.5 Conclusion

In this chapter, the experimental tests used for identifying the sintering model parameters have been presented. The chapter starts by a brief literature review of sintering parameters used in different constitutive models and their identification procedure via experimental tests follows by the experimental test devices used in this research. In this regard, dilatometry (thermo-mechanical analysis) has been explained in detail which is used for investigating the kinetics of sintering as well as determining the parameters associated with the thermal part of the constitutive model of sintering deformation.
Then, the pyroplastic behaviour analysis and the sinter-bending test sit developed for measuring the pyroplastic deformation of materials have been presented.
The experimental test sits used in this research are designed in a way that they meet our technical needs as well as our partners' economic criteria and simplicity. These devices can be easily used in industrial scale and can come up with reliable results for industrial as well as research needs.

Summary in French

Dans ce chapitre, les essais expérimentaux utilisés pour identifier les paramètres du modèle de frittage ont été présentés.
Le chapitre commence par une brève revue de la littérature des paramètres de frittage utilisés dans les différents lois de comportement et de leur procédure d'identification par des essais expérimentaux.
Ensuite, l'essai de dilatométrie (analyse thermo-mécanique) a été expliqué en détail. Cet essai est utilisé pour étudier la cinétique de frittage ainsi que l'identification des paramètres associés à la partie thermique de la loi de comportement de frittage.
Finalement, l'analyse du comportement pyroplastique et l'essai de flexion-frittage mis au point pour mesurer la déformation pyroplastique de matériaux ont été présentés.

Chapter -IV-

Anisotropic constitutive model for traditional porcelain sintering

Contents

IV.1 Introduction

Although free sintering behaviour is often simply considered as isotropic, it seems that, in reality, sintered bodies often shrink in an anisotropic way [green2008constrained]. This anisotropy can be characterized by measuring the longitudinal and transverse dimensions before and after sintering.
This sintering anisotropy arises from many microscopic origins such as: particle packing, alignment of particles, difference in surface energies of crystallographic orientations, presence of oriented inclusions, etc [green2008constrained].
The orthotropic microstructural features in green bodies are usually generated during forming processes such as slip casting, pressing, compaction, dip coating, gravity casting, etc.
In this chapter an anisotropic sintering model is presented to describe the densification behaviour of a slip cast porcelain during the firing process.
The material and the slip casting process are presented briefly. Then, the results of experimental tests used for identifying model parameters are explained.

IV.1.1 Material of the study

The study was carried out on slip cast ceramic plates consisting of particles containing 60% kaolin, 15% feldspath and 25% quartz. The mixture of these powders are milled and mixed with water in order to achieve particles with $7-8\mu m$ diameter. The chemical composition of slurry is reported in table IV.1. The obtained suspension was filtered and pressed in order to

SiO_2	Al_2O_3	TiO_2	Fe_2O_3	MgO	CaO	Na_2O	K_2O
65.5	23.8	0.07	0.21	0.21	0.13	0.61	2.77

Table IV.1 : Chemical analysis (%) of slurry used for slip casting specimens.

get the concentrated suspension which is then used to prepare the casting slurry by adding water and appropriate amount of dispersing agents such as sodium polyacrylate.

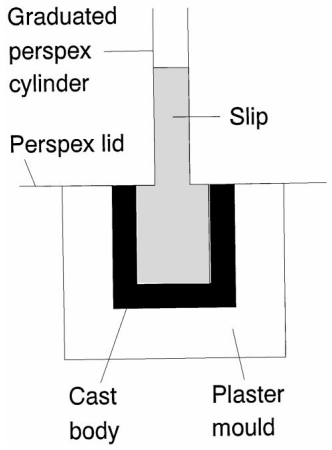

Figure IV.1 : Slip casting of ceramic slurry for manufacturing plate specimens.

The consolidation of concentrated suspensions by slip casting was carried out in a plaster mould to produce bars of $120mm \times 40mm \times 8mm$ which were dried at room temperature for 24 hours and then pre-fired at $990°C$ with a heating rate of $2°C/min$.

IV.2 Process

In this section a short introduction to slip casting process is presented. This method has been used for manufacturing porcelains as well as technical and traditional ceramics for many years. Despite some inconveniences, it provides superior surface quality, density and uniformity in shaping high-purity ceramic raw materials over other ceramic casting techniques.

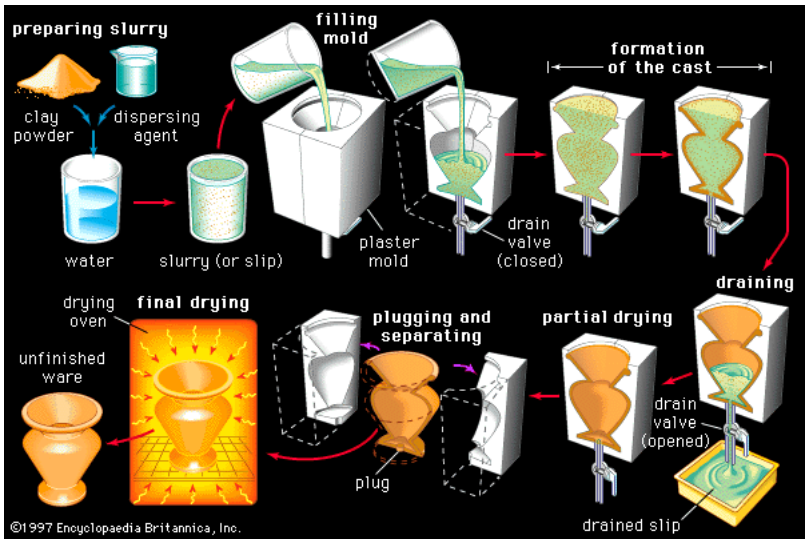

Figure IV.2 : Schematic of the slip casting process.

The first step of the slip casting technique consists in making a slurry with the desired material and solvent. A dispersant and some binding agent must be added in the slurry.
After the slurry is properly prepared it is poured into a mold of a specific design. The mold contains micro-pores all throughout its structure which act as capillaries. These pores use a capillary action to draw the liquid out of the slurry and into the mold. As this happens, a layer of material builds up on the inside of the mold. Figure IV.2 illustrates the slip casting process.
When the desired thickness of solids is built up on the mold walls, the excess liquid is poured out. The material cast and mold are allowed to dry. As the cast dries it shrinks and separates from the mold walls and the cast can then be sintered. Fabrication of complex shaped parts is easily possible by this process [takao2002microstructure,young1991gelcasting, bitterlich2002rheological].
One of the inconveniences met in slip casting process is the preferential orientation phenomenon which is the origin of heterogeneous deformations of slip cast ceramics during the firing process.

IV.3 Preferential orientation in slip casting process

Slip casting process is involved with high density as well as preferential orientation phenomena. These phenomena are the consequence of fluid mechanics.
During casting and drying processes, particles migrate toward the edge of plaster mould where a crust is formed by drying. This crust is analogous to permeable plaster wall absorbing the water from the suspension. As particles approach the wall, they stream in channels and orient with the long dimension parallel to the channel direction because of fluid shear across the channel. As the channel narrows, the particles wedge into the wall with the orientation

geometry, resulting in dense packing. As one channel becomes obstructed, others will open and the process will repeat.
Under different slip casting conditions, green densities up to 60% can be achieved on sub-micrometer slips [evans1982structural, naito1997optimization].
This chapter will continue by presenting the experimental results obtained from slip cast ceramic plates thermo-mechanical analysis.

IV.4 Experimental Analysis

Experimental analysis consists of three different high temperature experiments:

- Study of sintering kinetics by dilatometry
- Densification analysis of samples along different axes
- Pyroplastic behaviour investigation by sinter-bending test of green ceramic as well as pre-sintered (dense) samples

These thermo-mechanical characterizations are essential for developing a phenomenological constitutive model of sintering of slip cast ceramic plates as well as identification of model parameters. Furthermore, the microstructure of porcelain samples has been observed by scanning electron microscope (SEM) and X-ray micro-analysis has been performed on specimens before and after sintering.
The sintering cycles used for experimental tests are shown in figure IV.3.

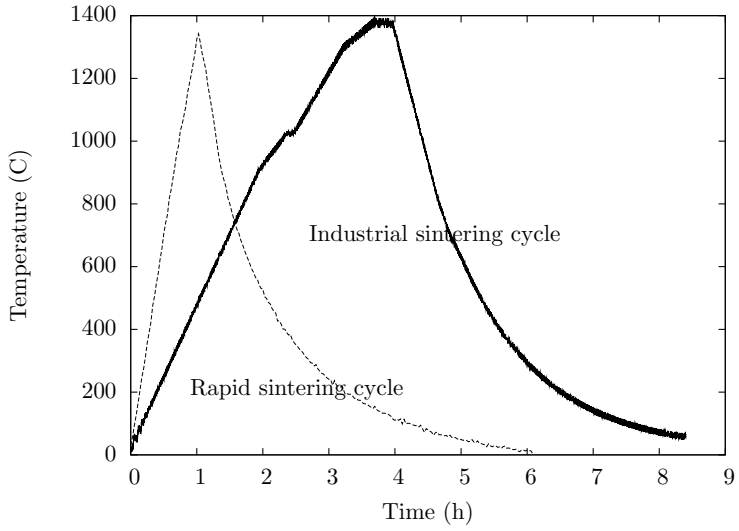

Figure IV.3 : Corresponding sintering cycles for sinter-bending test.

The conventional (industrial) sintering cycle consists of heating, maintain at $1400°C$ and finally cooling stage. However, the rapid sintering cycle consists of a heating and a cooling stages with a heating rate two times faster than that of industrial cycle.

IV.4.1 Free sintering test

In order to highlight the anisotropic behaviour of slip cast ceramic plates, two tests were successively carried out with shrinkage measurement along either X, Y or Z direction. First of all, the slip cast ceramic plate was cut into small cubic specimens. As shown in figure IV.4,

the plate was cut into 4 rows and 12 lines. These 48 cubic samples have been free sintered at the same time in an electric furnace. The shrinkages which have been measured during free sintering along different directions, and also on different rows and lines, have been compared in figures IV.5 and IV.6. The measurements performed at the end of the test lead to different shrinkages along different axes:

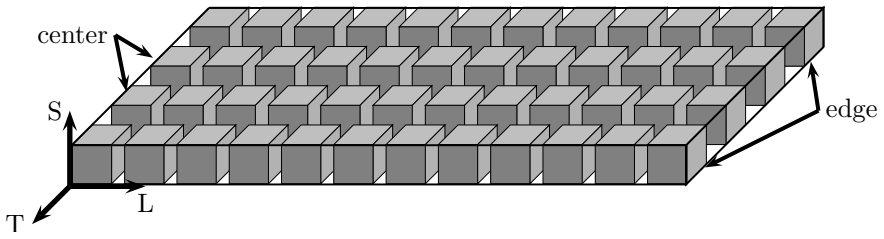

Figure IV.4 : Slip cast ceramic plate after cutting into small cubic samples.

The result of this simple test revealed the anisotropic behaviour of slip cast plates. As shown in figures IV.5 and IV.6, the specimens collected from the middle of the plates, either in the center or the border, present similar amounts of shrinkage. On the other hand, the shrinkage data are more scattered at the two ends of the plates.

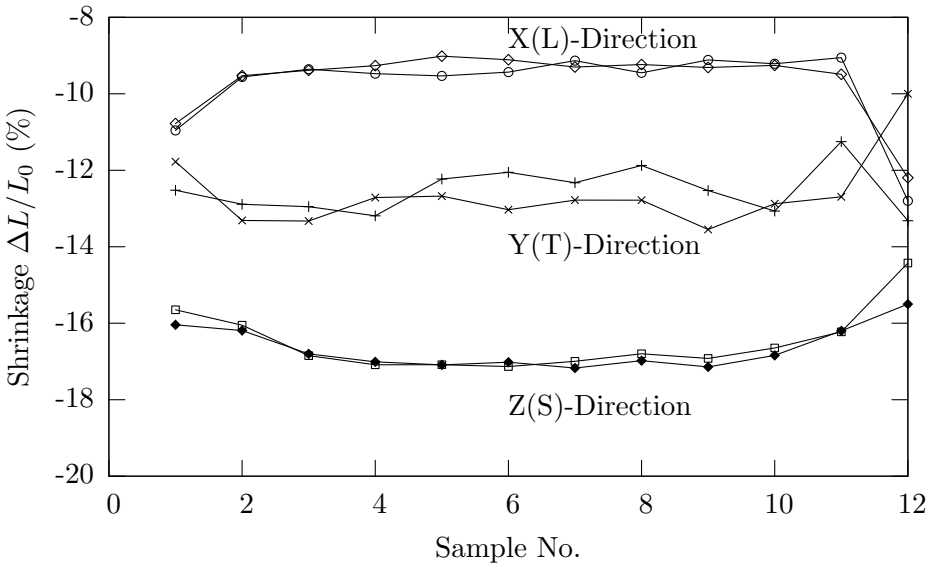

Figure IV.5 : Experimental evidence of anisotropy in slip cast plates. Free sintering shrinkage along different directions on the border of the plate.

Moreover, by comparing figures IV.5 and IV.6, the average shrinkage observed in the border and the center of the plate are almost the same. Hence, the smallest shrinkage has been observed along slip casting direction x $(9 - 10\%)$.

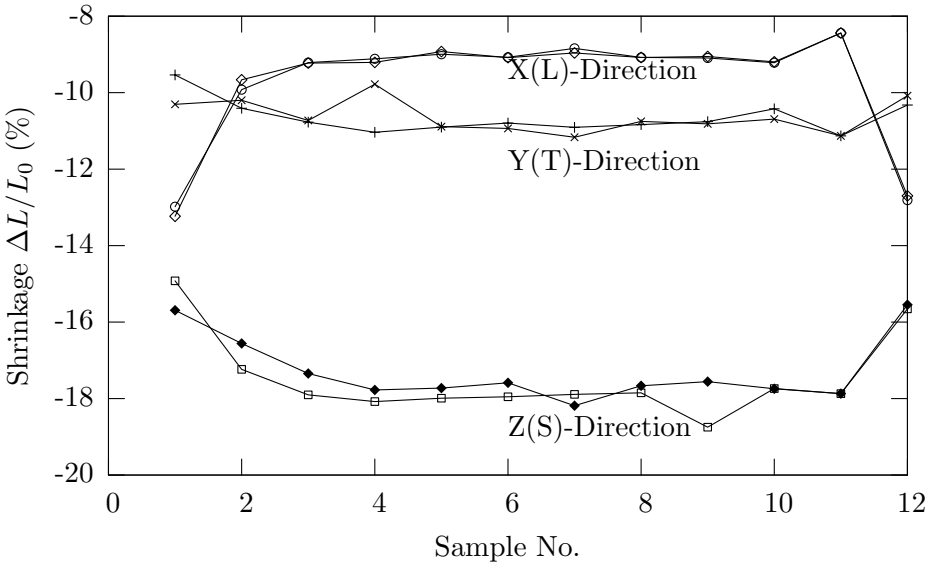

Figure IV.6 : Experimental evidence of anisotropy in slip cast plates. Free sintering shrinkage along different directions in the center of the plate.

The shrinkage along normal axis of slip casting (Z) is about 2 times larger than that of casting direction ($17 - 18\%$). This simple test revealed a strong anisotropic densification behavior in porcelain plates which will be discussed later.

IV.4.2 Densification kinetics

The second test for investigating the anisotropic behaviour of slip cast samples is dilatometric measurements along different directions. These tests have been realized on small samples collected from slip cast plates. All the samples have been collected from the center of the plates in order to avoid data scattering due to edge effects. Shrinkages measured during dilatometric sintering tests along different directions are presented in figures IV.7 and IV.8. All the samples have been sintered using a unique industrial heat treatment cycle.
The densification curve is divided into three stages. After a slight volume increase due to thermal expansion, the principal phase of sintering starts by eliminating open porosities and reducing closed porosities in the final phase. The last phase is related to the thermal shrinkage in the cooling part of the sintering cycle. According to these curves (figures IV.7 and IV.8) the thermal expansion coefficient of porcelain is $\alpha = 8 \times 10^{-6}\ K^{-1}$.
Figure IV.7 illustrates the densification behavior of porcelain specimen under $50g$ compressive load.

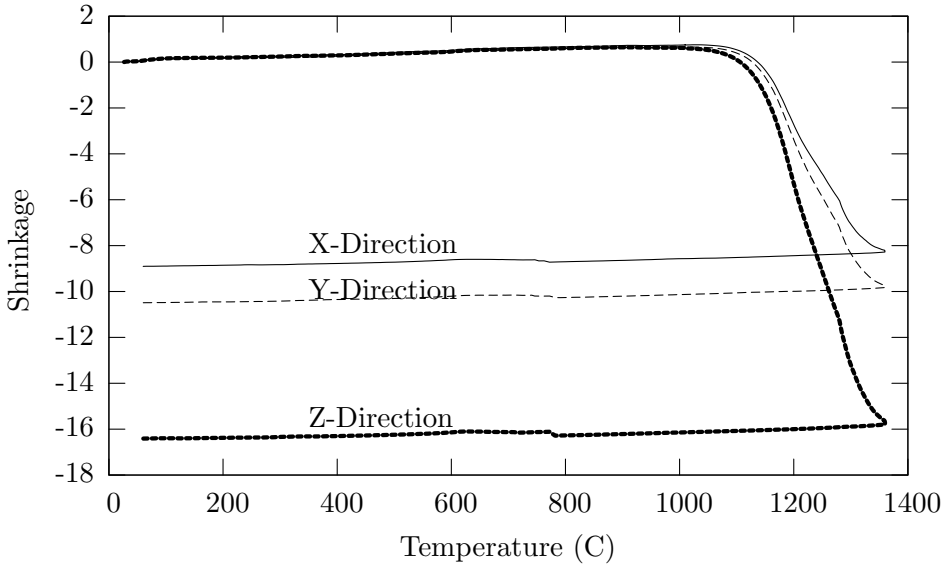

Figure IV.7 : Effect of test direction on shrinkage behaviour of slip cast samples (load=50g).

Similar tests have been carried out by applying $100g$ compressive load (figure IV.8).

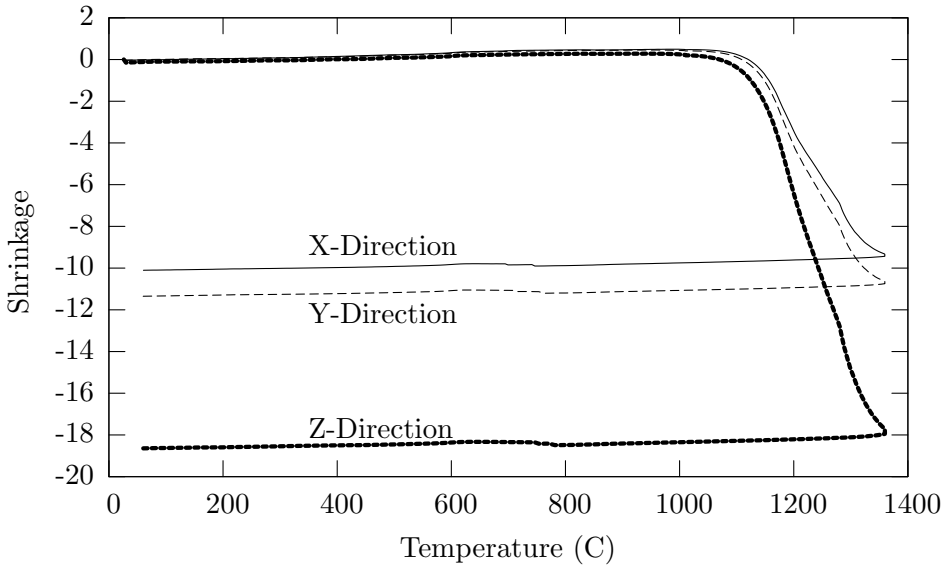

Figure IV.8 : Effect of test direction on shrinkage behaviour of slip cast samples (load=100g).

The comparison of densification curves obtained by applying $50g$ load with those of $100g$ load demonstrates a slight effect of applied load on sintering shrinkage. This fact will later influence the model identification process.
Figures IV.9, IV.10 and IV.11 show the influence of different loads on densification behaviour of specimens along X, Y and Z axes respectively.
In order to perform all these experimental tests, 9 cubic samples have been taken from different locations of one slip cast ceramic plate. The samples, one by one, have been sintered with a unique thermal cycle under 3 different loads: $50g$, $100g$ and $150g$.

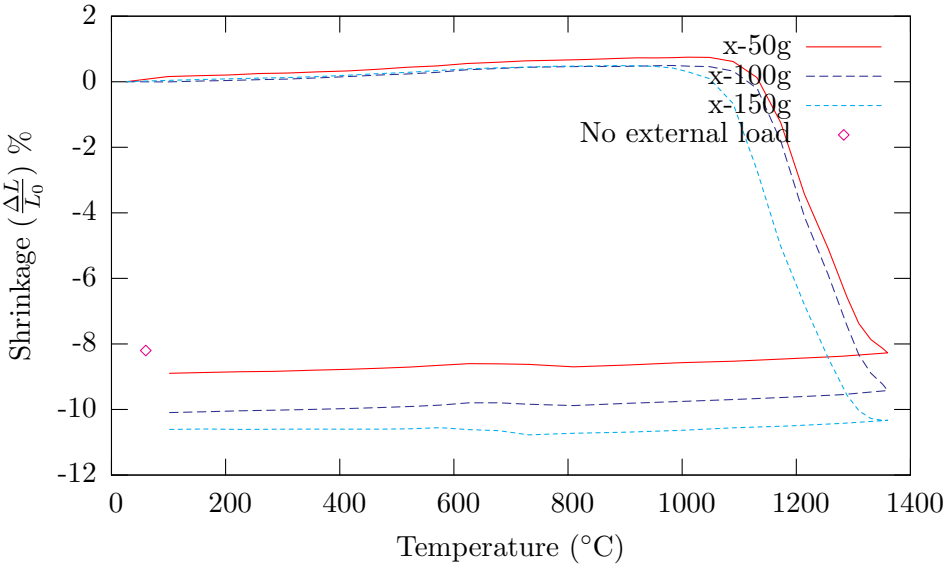

Figure IV.9 : Effect of the applied load on the densification behaviour along X axis.

The densification rates obtained along X, Y and Z axes are $9-10\%$, $11-12\%$ and $17-18\%$ respectively. The scatter observed in these results are related to the fact that every sample has been taken from different locations of the slip cast plate and then presents various densification rates. In addition, it seems that the applied load has a very slight effect on the sintering strain.

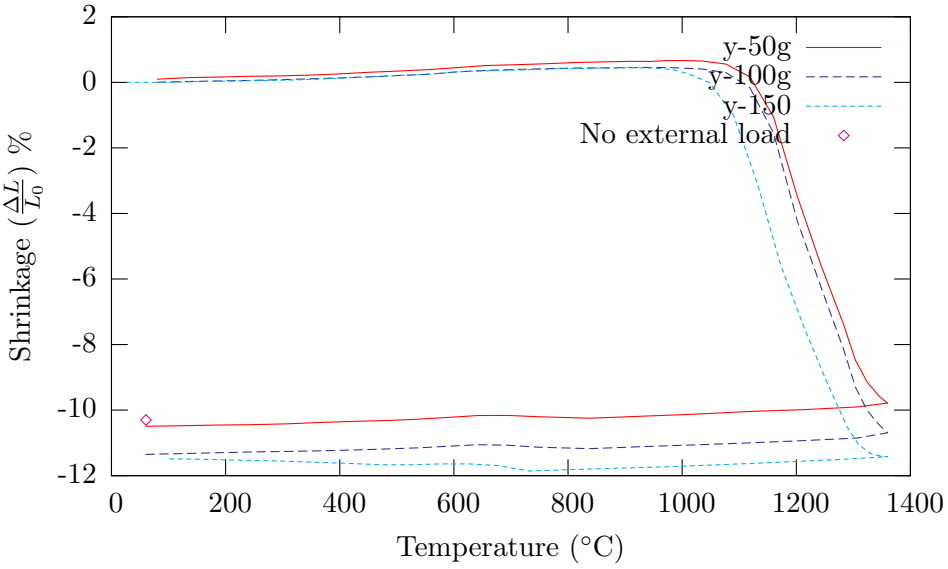

Figure IV.10 : Effect of the applied loads on the densification behaviour along Y axis.

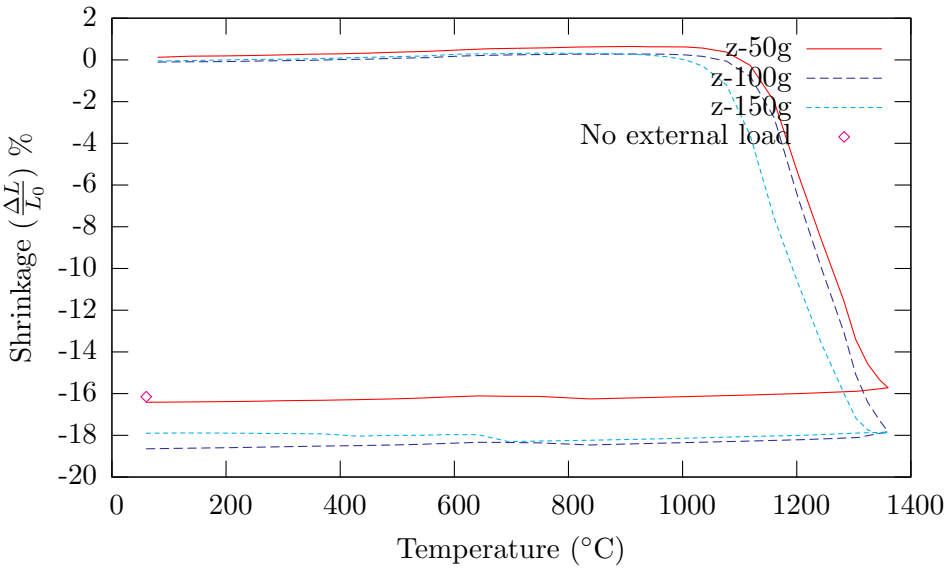

Figure IV.11 : Effect of the applied load on the densification behaviour along Z axis.

IV.4.3 Scanning Electron Microscopy analysis

The microstructure and X-ray micro analysis of traditional porcelain used in this research before and after sintering is shown in figures IV.12 and IV.13 respectively.

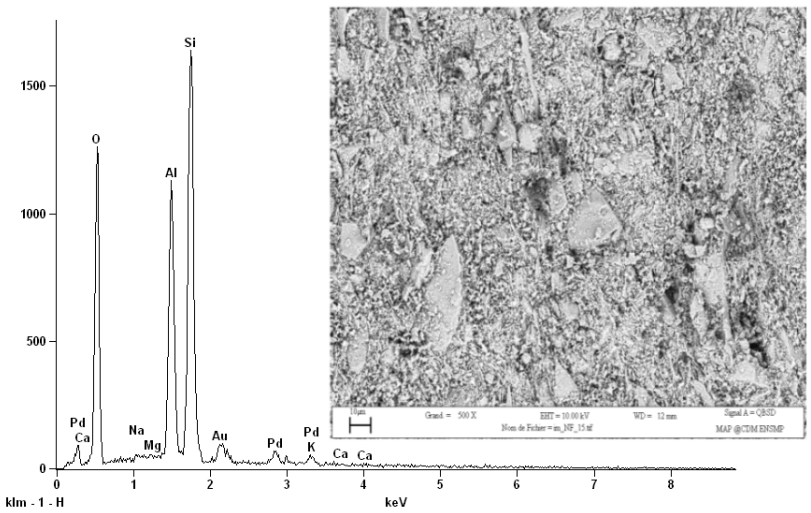

Figure IV.12 : Micro-structure and X-ray diffraction analysis of specimens before sintering.

The initial powders for making slurry are composed of alumina and silica (before sintering).

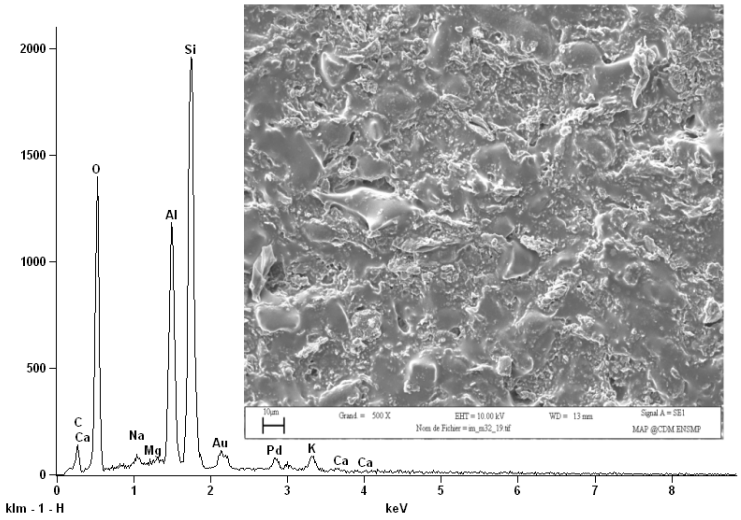

Figure IV.13 : Micro-structure and X-ray diffraction analysis of specimens after sintering.

The microstructure and micro analysis after sintering are presented in figure IV.13.

IV.4.4 Pyroplastic behaviour

Pyroplastic behaviour analysis of slip cast porcelain plates is presented in this part. Figure IV.14 illustrates the beam deflection for two sintering cycles (rapid and conventional). The corresponding sintering cycles are presented in figure IV.3.

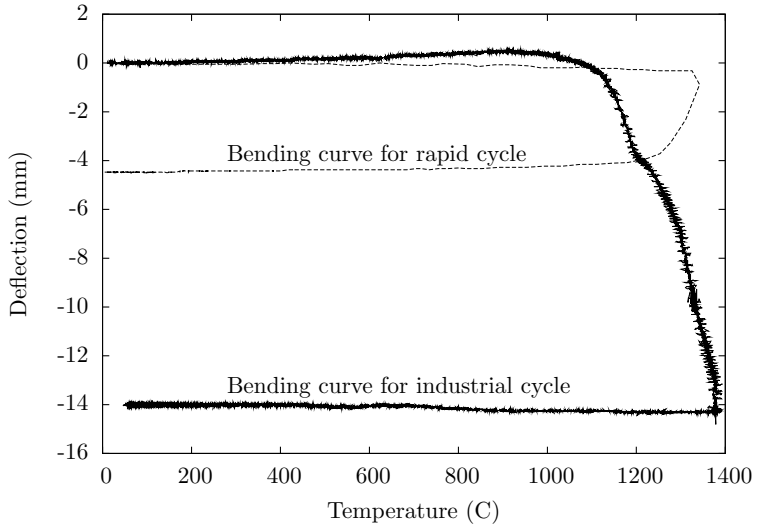

Figure IV.14 : Bending curves detected by laser assisted deflection measuring apparatus.

The beam deflection observed during both sintering cycles demonstrates that the pyroplastic behaviour depends largely on heating rate as well as the holding duration indicating that creep seems to be the dominant mechanism. As shown in figure IV.14, the deflection observed in the industrial sintering cycle is 3 times larger than that of rapid cycle. These results have been completed by another experimental test: sinter-bending of a pre-fired (dense) ceramic plate.

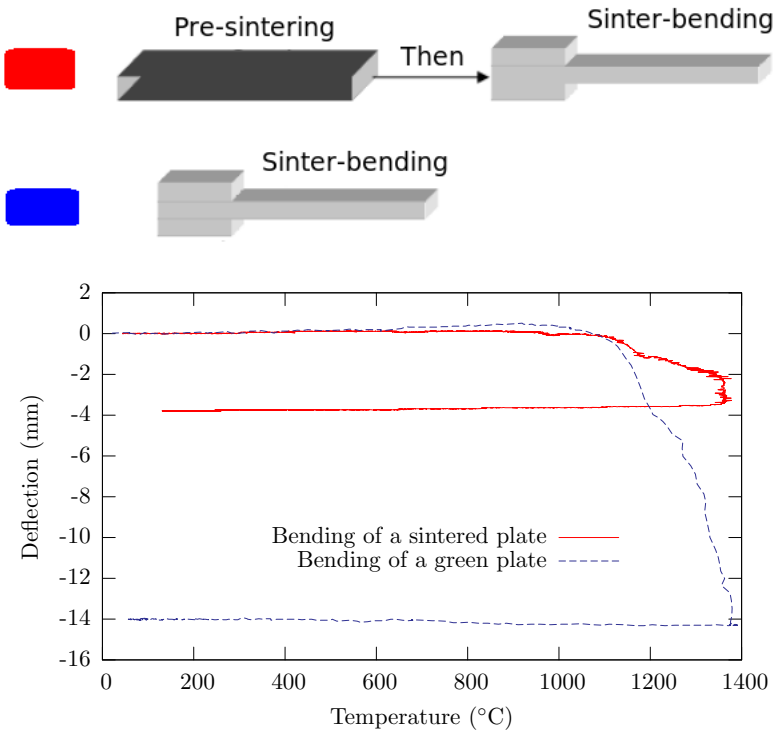

Figure IV.15 : Bending curves detected for a pre-sintered ceramic plate and a green (non-sintered) ceramic plate for a given sintering cycle.

Figure IV.15 shows the deflection curves measured for a green plate and a pre-fired dense plate. The dashed curve represents the deflection of the green (non-sintered) porcelain plate. Thus, the solid line curve is the bending result of a pre-sintered ceramic plate.
In order to prepare the pre-sintered specimen, a green ceramic plate is placed upright on a rigid alumina substrate and this structure has been sintered in an electric furnace.
These results show that the pre-sintered plate has been deflected during sinter-bending test. The amount of deflection is obviously smaller than that of green ceramic beam. The origin of deflection in this case is entirely associated with creep deformation and not sintering deformation since the material is already densified.
The results obtained from this test can be used for determining the viscosity of the material.

IV.5 Anisotropic sintering model

The constitutive equations for the porous ceramic must be able to describe both anisotropic sintering and pyroplasticity. The last phenomenon is caused by the viscoplastic deformation of the body under gravity. Therefore the constitutive equations must also describe stress controlled viscous deformation. Gravity is modelled as a prescribed body force in numerical simulations. The strain rate tensor is written as a sum of three terms as:

$$\underline{\dot{\varepsilon}} = \underline{\dot{\varepsilon}}_{\text{th}} + \underline{\dot{\varepsilon}}_c + \underline{\dot{\varepsilon}}_s \tag{IV.1}$$

where $\underline{\varepsilon}_{\text{th}}$ represents the thermal dilatation, $\underline{\varepsilon}_c$ the stress controlled viscous deformation (creep) and $\underline{\varepsilon}_s$ the sintering deformation. Elastic deformation is neglected. Thermal dilatation ($\underline{\varepsilon}_{\text{th}}$) is expressed as

$$\underline{\varepsilon}_{\text{th}} = \alpha(T)(T - T_{\text{ref}})\underline{1} \tag{IV.2}$$

where $\alpha(T)$ is the secant dilatation coefficient, T_{ref} a reference temperature and $\underline{1}$ the unity second order tensor. The sintering rate ($\underline{\dot{\varepsilon}}_s$) is expressed as a function of both temperature and porosity as:

$$\underline{\dot{\varepsilon}}_s(f,T) = \begin{pmatrix} \dot{\varepsilon}_s^x(f,T) & 0 & 0 \\ 0 & \dot{\varepsilon}_s^y(f,T) & 0 \\ 0 & 0 & \dot{\varepsilon}_s^z(f,T) \end{pmatrix} \tag{IV.3}$$

where x, y and z represent material reference directions. Using different functions for $\dot{\varepsilon}_s^{x,y,z}$ allows to simply model anisotropic sintering. Viscous flow is assumed to depend linearly on stress which is consistent with high temperature diffusional creep or liquid phase assisted creep. However the deformation rate depends on porosity as porous bodies tend to deform more easily than fully sintered dense bodies. Accordingly creep deformation rate is given as:

$$\underline{\dot{\varepsilon}}_c = \frac{1}{\eta(T)} \underline{\underline{M}}(f) : \underline{\sigma} \tag{IV.4}$$

where η represents the viscosity of the dense body. The fourth order tensor $\underline{\underline{M}}$ is introduced to model the effect of porosity on deformation rate. For the sake of simplicity $\underline{\underline{M}}$ is assumed to depend on porosity only and to be isotropic. Anisotropic creep could be modelled using a more generic expression for $\underline{\underline{M}}$ but this would require a complex experimental procedure and would increase the number of parameters. A similar methodology was adapted in [sarbandi2010anisotropic, BessonAbouaf91a, BessonAbouaf91b, song2006experiments] together with isotropic sintering. $\underline{\underline{M}}$ is then expressed as:

$$\underline{\underline{M}}(f) = \frac{3}{2} C(f) \underline{\underline{J}} + F(f) \underline{\underline{K}} \tag{IV.5}$$

C and F are functions of the porosity such that, for a rigid body, $C(0) = 1$ and $F(0) = 0$. $\underline{\underline{J}}$ is the fourth order tensor such that:

$$\underline{\underline{J}} : \underline{\sigma} = \underline{s} = \underline{\sigma} - \frac{1}{3} \text{trace} \underline{\sigma} \underline{1} \tag{IV.6}$$

$\underline{s}$ is the stress deviator.
$\underline{\underline{K}}$ is the fourth order tensor such that:

$$\underline{\underline{K}} : \underline{\sigma} = \frac{1}{3} \text{trace} \underline{\sigma} \underline{1} \tag{IV.7}$$

These constitutive equations were implemented in the finite element code Zset [BessonFoerch97]. Finite deformations were accounted for using a co-rotational reference frame [SidoroffDogui01]. This simple formulation allows the additive strain decomposition to be used.
Following specific expressions were used for the various material parameters. C and F are expressed as:

$$C = 1 + C_0 f^{n_C} \qquad F = F_0 f^{n_F} \tag{IV.8}$$

Viscosity is assumed to obey an Arrhenius law as:

$$\eta = \eta_0 \exp\left(\frac{Q}{RT}\right) \tag{IV.9}$$

The same activation energy (Q) is assumed to control sintering (i.e. similar physical phenomena are assumed to control creep and sintering), so that the $\dot{\varepsilon}_s^{x,y,z}$ coefficients are expressed as:

$$\dot{\varepsilon}_s^{x,y,z} = -f^{n_s} \dot{\varepsilon}_{s0}^{x,y,z} \exp\left(-\frac{Q}{RT}\right) \tag{IV.10}$$

This expression also respects the fact that for a fully sintered body ($f = 0$), the sintering strain rate should be zero $\dot{\varepsilon}_s(f = 0) = 0$.

IV.6 Parameter identification

Several material parameters need to be identified: η_0, Q, C_0, n_C, F_0, n_F, $\dot{\varepsilon}_{s0}^{x,y,z}$ and n_s.
The parameters associated with sintering have been identified using densification curves. On the other hand, creep related parameters have been determined by correlating sinter-bending experimental curve with corresponding numerical simulation results.
The experimental results obtained from free sintering experiment (section IV.4.1) can be used in order to modify the parameter identification process. The parameters (F_0, n_F) of the volumic part of the model (F) can be related to the mean volume strain of free sintered samples (section IV.4.1). Mean volume strain (ε_m) can be evaluated for each sample as:

$$\varepsilon_m = \frac{1}{3}\left(\log\left(1+\frac{\Delta L_x}{L_{0x}}\right)+\log\left(1+\frac{\Delta L_y}{L_{0y}}\right)+\log\left(1+\frac{\Delta L_z}{L_{0z}}\right)\right) \tag{IV.11}$$

Results of mean volume strain are presented in fig. IV.16. It is shown that the volume change is almost constant. A small difference is observed between the center (mean value -0.135) and the border (-0.139). It can be concluded that the initial porosity gradient is negligible and the observed shrinkage anisotropy is to be related to local grain arrangement.

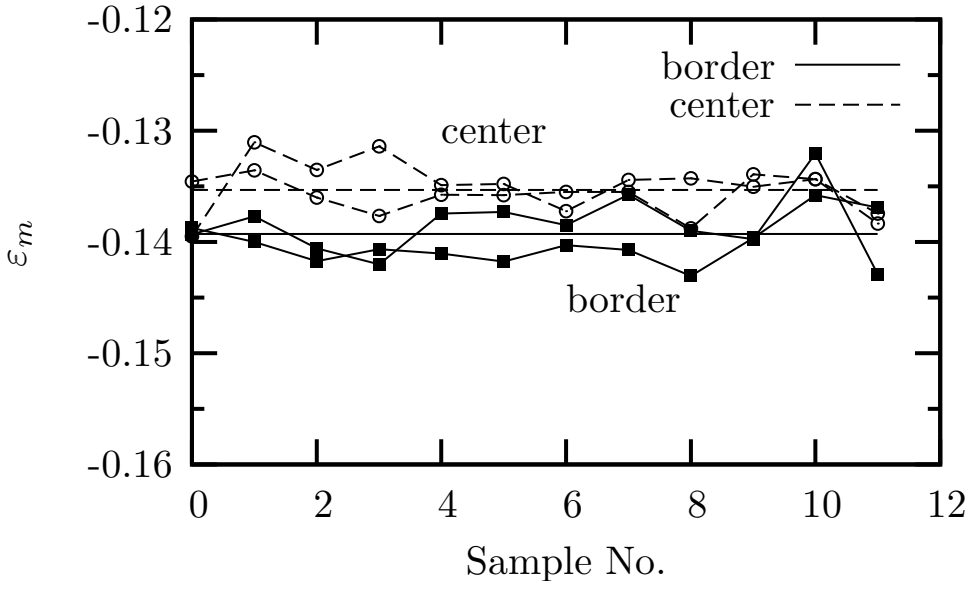

Figure IV.16 : Mean volume strain after free sintering test.

In addition, the load only slightly affects the shrinkage and measurements carried out on samples after sintering showed that the mean volume strain is unaffected. Consequently it can be assumed that $F \simeq 0$, so that the material can be considered as pressure independent within the experimental range. As running numerical simulation with $F \simeq 0$ is impossible, two solutions can be considered:

- Considering $F = 0.001$
- Considering $F = 0$ and using special finite elements called *mixed elements* $(\vec{U}, p)$.

The identification and the numerical simulation have been performed using mixed elements. An automatic identification algorithm was used to obtain the numerical coefficients. The optimisation is performed by simulating the various tests and correlating the simulated results

with experimental ones.

Sintering		Creep / Dilatation	
$\dot{\varepsilon}_s^x$	1783 s^{-1}	C_0	1.46
$\dot{\varepsilon}_s^y$	2024 s^{-1}	n_C	1.063
$\dot{\varepsilon}_s^z$	3390 s^{-1}	η_0	$1.06\,10^{-3}$ $MPa.s$
n_s	1.45	α	$8.\,10^{-6}$ K^{-1}
Activation energy Q : 206 kJ			

Table IV.2 : Optimized model parameters.

The same activation energy Q is supposed to control both sintering and creep deformation. Optimized parameters are given in tab. IV.2.

IV.6.1 Comparison of experimental and simulated tests: Dilatometry

Sintering parameter identification process has been performed by correlating shrinkage curves (experimental dilatometric result) with corresponding numerical graphs (figure IV.17).
In order to obtain the numerical shrinkage curves, an eight-node brick element (8 integration points and full integration mode) has been simulated according to the sintering cycle (thermal loading). The symmetrical and multi-point constraints boundary conditions are taken into account. The displacement graph of the upper nodes represents the mentioned numerical curve which is used for optimisation process.

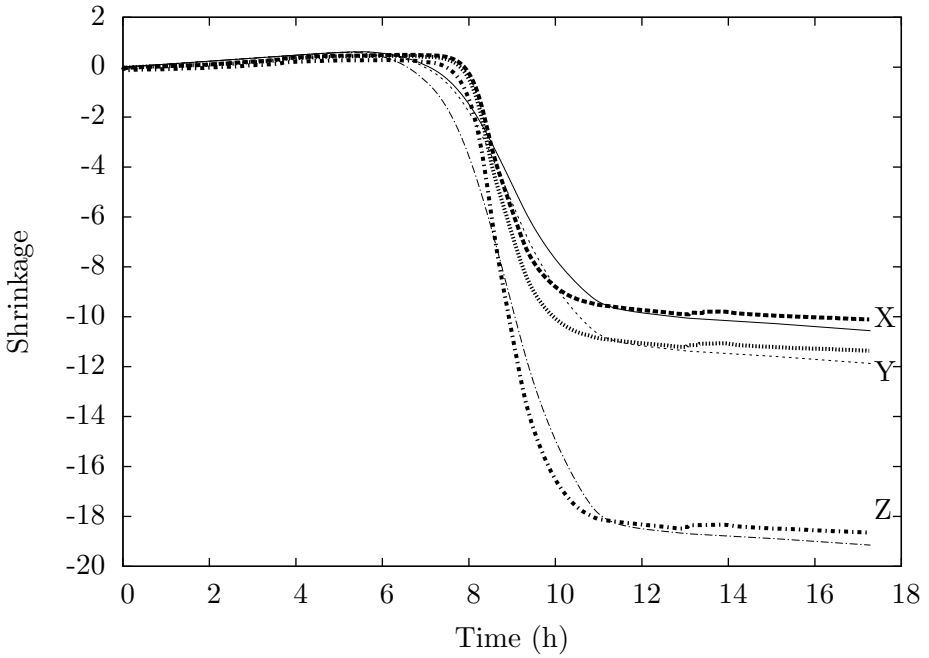

Figure IV.17 : Experimental and numerical densification curves along X,Y and Z directions after optimisation .

Figure IV.17 compares experiments and numerical simulations (optimised curves) along different directions for determining the sintering parameters of the constitutive model.

IV.6.2 Comparison of experimental and simulated tests: Sinter-bending

The same optimization algorithm has been used for identifying the mechanical parameters of the model by adjusting numerical and experimental curves of sinter-bending tests. Figure IV.18 presents the numerical and experimental curves after optimization for a green ceramic specimen.

Mixed elements with full integration were used to simulate sinter-bending test. Adjusted

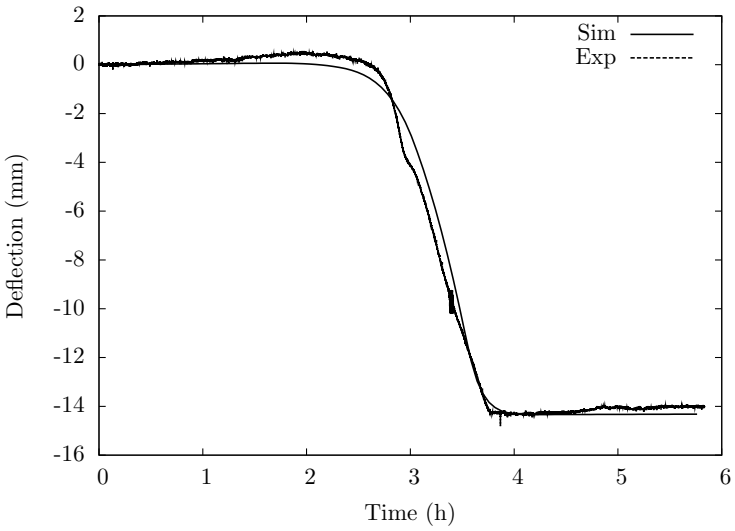

Figure IV.18 : Experimental and numerical deflection (sinter-bending) curves after optimisation.

mechanical parameters of the model are presented in table IV.2. The von Mises stress level observed during sinter-bending simulation does not exceed some kPa. Moreover, comparison

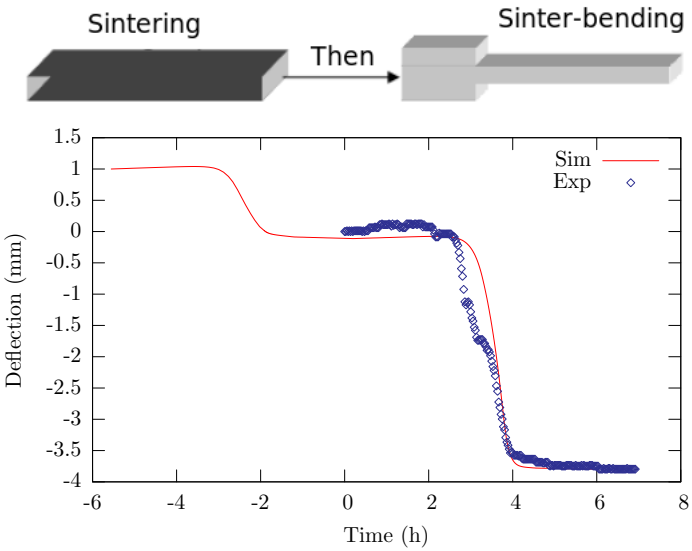

Figure IV.19 : Experimental and numerical deflection (sinter-bending) curves after optimisation for rigid (sintered) specimen.

of sinter-bending test result of fully sintered ceramic beam with corresponding numerical simulation results is shown in Figure IV.19. The optimised parameters have been presented in table IV.2.

IV.7 Finite element simulation of porcelain sintering

The identified model parameters have been used to simulate the deformation of a lampshade base made of the same material by slip casting process. The lampshade geometry and the associated mesh are shown in figure IV.20. In order to consider the anisotropic behaviour, a local coordinate system has been defined in a way that slip casting direction and its normal be respected. Mixed field formulation elements have been used in order to take into account the incompressibility [Taylor00].

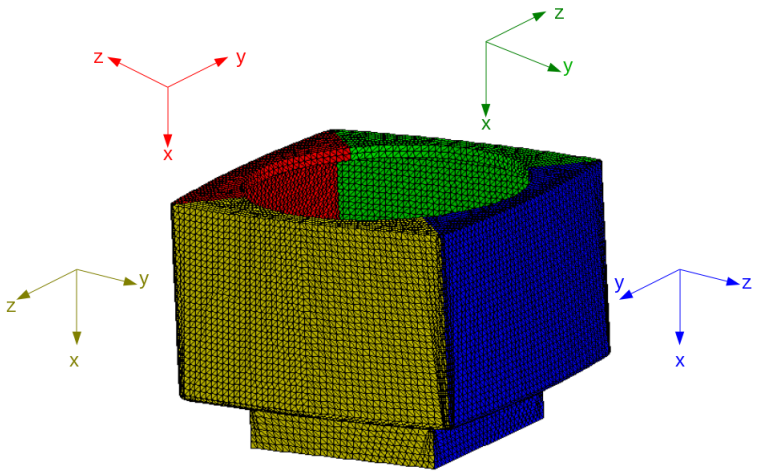

Figure IV.20 : Definition of a local coordinate system.

Numerical simulation of the lampshade porcelain is also shown in figure IV.21. The von Mises stresses developed during numerical simulation of the lampshade reach a level of some kPa, close to the stress level applied during dilatometric tests.

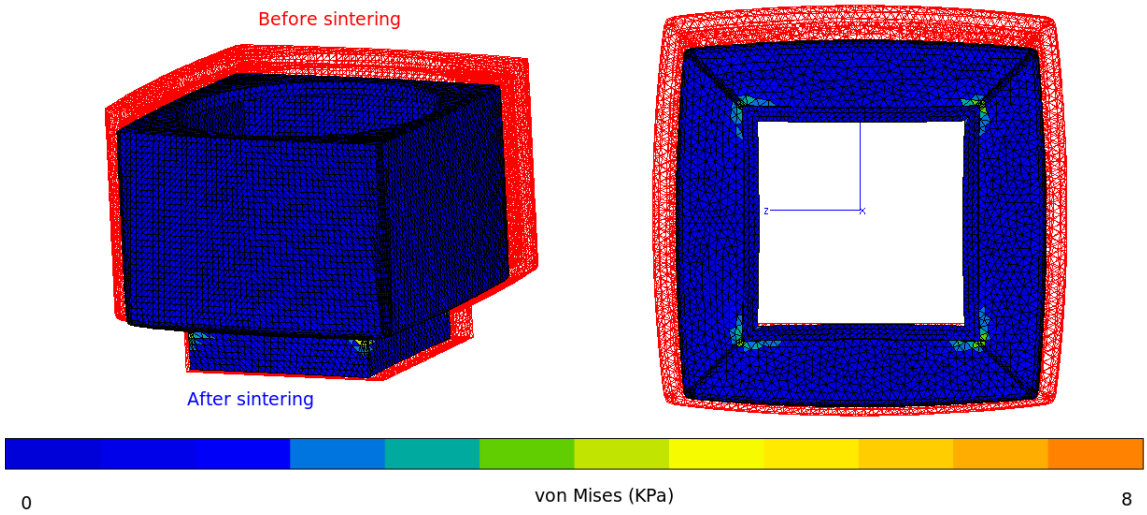

Figure IV.21 : Finite element simulation result.

Finite element simulation has been carried out by applying the following boundary conditions: (i) fixing the bottom of the lampshade along x direction, and (ii) preventing

any rigid body motion by fixing other points along y and z directions.

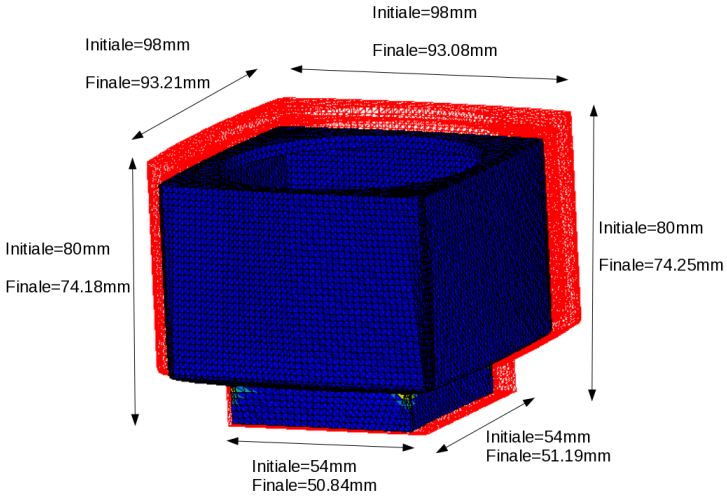

Figure IV.22 : Dimensional change during sintering.

High levels of stress only develop at the sharp-ended corners. Also during sintering straight square sides of lampshade are curved towards the center. The same deformation (curvature of straight square sides) has been observed during the sintering of the lampshade. This part can be sintered on a rigid substrate or it can be suspended in a sintering furnace without the use of rigid substrates. The numerical simulation results presented in figures IV.22 and IV.21 are related to the latter case. For modelling the sintering of lampshade on a rigid substrate, the interactions between the lampshade and its support should be taken into account. Figure IV.22 shows the dimensional changes of the part during numerical simulation. Unfortunately, the experimental dimensional change during firing process of the lampshade has not been provided by the industrial partners of the project.

IV.8 Conclusion

In this chapter, the densification and pyroplastic behaviour of a slip cast traditional porcelain have been presented.
In addition, an anisotropic phenomenological constitutive sintering model has been proposed, according to the thermomechanical test results. Different experimental tests have been used in order to identify the sintering model parameters. The proposed set of constitutive equations can be used to simulate the sintering of actual parts manufactured by slip casting process. Mixed field formulation elements have been used in order to deal with the incompressibility of studied material.

Summary in French

Dans ce chapitre, le comportement thermo-mécanique, la densification et le comportement pyroplastique d'une porcelaine traditionnelle fabriquée par coulage ont été présentés.
Basée sur ces résultats, une loi de comportement anisotropique de frittage a été proposée. Différents essais expérimentaux ont été utilisés afin d'identifier les paramètres de la loi de frittage.
La loi de comportement peut être utilisée pour modéliser les déformations des pièces réelles fabriquées par coulage.
Des éléments spéciaux avec une formulation mixte ont été utilisés afin de traiter le comportement incompressible de matériau.

Chapter -V-

Constitutive model for sintering of investment casting ceramic core

Contents

V.1 Introduction

In this chapter, the thermo-mechanical characterization of ceramic core (shell) used in investment casting of superalloys is discussed. Furthermore, an original constitutive model for predicting deformation of a ceramic core during sintering is developed.
Finally model parameters identification from experimental results as well as finite element simulation will be presented.
Silica based ceramic cores have been used for the investment casting of superalloys parts in the aerospace industry. Recent developments in ceramic core research have been devoted to composition and process modification [lequeux1994low, greskovich1979alumina].

V.2 Investment casting ceramic cores

Ceramic cores used for investment casting of Ni based super-alloys (for turbine blades) are usually fabricated by injection moulding process.
The ceramic core is used to make hollow parts or complex geometries (figure V.1). The lost wax process is often selected for its very high dimensional accuracy.

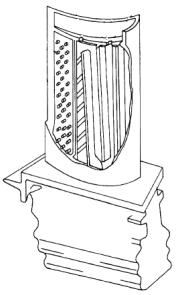

Figure V.1 : Perspective cut-away view of an investment cast turbine engine blade structure.

These ceramic cores (figure V.2) have various sizes and complexity levels: from some millimetres to nearly 1 meter, and from very simple to more complex shapes (figure V.2).

Figure V.2 : Various ceramic cores for turbine blade and vanes.

Ceramic core manufacturing process consists of:

- Mixing; according to technical characteristics of the part to be obtained mixture of various ceramic powders are selected.
- Injection; High or low pressure injection can be used.
- Sintering; Each part is fired according to a standard thermal cycle, in order to obtain desired mechanical properties.

- Finishing and machining

- Impregnation and coating; Ceramic cores are brittle. Therefore, they should be impregnated with a special substance in order to increase their strength and also prevent any risk of breakage during handling. In case of use of the ceramic core with reactive alloys (such as Inconel 718) a specific alumina-based inert coating has to be applied, in order to prevent any reaction between metal and ceramic [shah2001cores, miller1978cores, beals2003investment, shah2008cores].

V.3 Material

The technology of manufacturing ceramic cores is highly protected by patents. However, it is known that the major components of ceramic cores used for investment casting of superalloys in aerospace industry are silica, zircon and minor quantities of oxide additives [chao2002optimal].
The chemical composition of a typical ceramic core used in investment casting is outlined in table V.1 [hennige1999shrinkage].

Material	**Formula**	**Typical %**
Silica	SiO_2	96.
Zircon	$ZrSiO_4$	1.5
Alumina	Al_2O_3	1.5
Trace elements	$Fe\ Bi\ Pb\ Ag\ Sb\ Sn\ Zn$	1.

Table V.1 : Chemical composition of a typical ceramic used for making cores in metal casting.

This chemical composition is similar to the material used in this research but does not exactly correspond to it. The exact chemical composition of the studied material is not presented due to confidential restriction imposed by the project partner.
In order to study the pyroplastic and densification behaviour of cores during sintering, plate-shaped and cylindrical-shaped specimens have been used respectively. They have been manufactured by injection moulding process (Figure V.3).

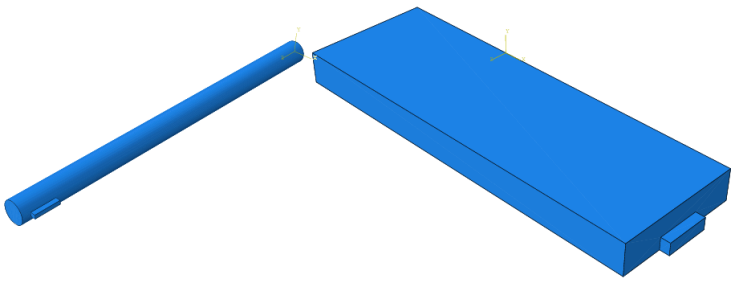

Figure V.3 : Injected moulded samples used for characterizing the densification behaviour and the pyroplastic behaviour.

A brief introduction of ceramic injection moulding process is presented in next section.

V.4 Ceramic injection moulding process

Thanks to advanced injection moulding technologies used in plastics and polymer materials, the use of injection moulding process for manufacturing ceramics has become prevalent during the recent decades.
Injection moulding consists in pushing a ceramic paste into the cavity of a closed mould by applying pressure.

binder	Polyethylene, polypropylene, polystyrene, paraffin, polyacetal
plasticizers	dibutyl phthalate, wax
binder	oleic acid, stearic acid

Table V.2 : Additive composition in ceramic injection moulding process.

In this process, the rheological characteristics of the ceramic paste must be perfectly controlled in order to fill the cavity homogeneously and insure the coherence of semi-finished injected part after removal from the mould.
Generally, during the injection process, the temperature of the thermoplastic ceramic paste is around $120 - 150°C$, in order to reduce its viscosity during the mould filling stage.
According to the applied pressure, this process is divided into two categories:

- High pressure injection (P$\simeq 50 - 300$MPa);
- Low pressure injection (P$\simeq 1 - 5$MPa).

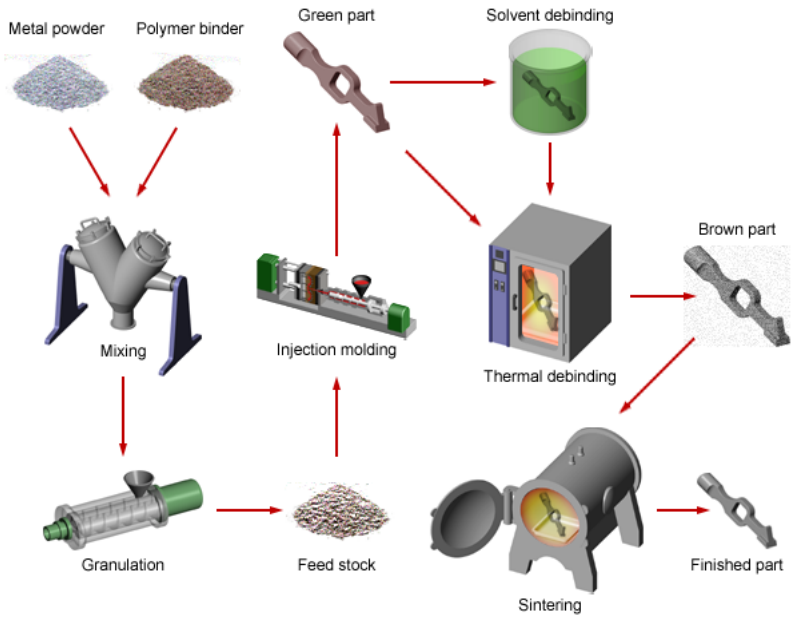

Figure V.4 : Ceramic injection moulding process.

In the high pressure injection process, special polymers which are used for increasing the viscosity of ceramic pastes, have high melting temperatures.

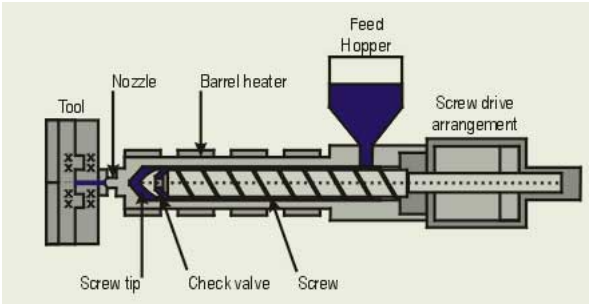

Figure V.5 : High pressure ceramic injection moulding process.

Injection of pastes through the nozzle of the mould introduces high shear stress fields ($1000 Pa.s^{-1}$) as well as high pressure. However, the ceramic paste temperature remains higher than the binder melting point ($100 - 220°C$, according to polymer nature). In order to guarantee the gradual solidification of the binder, the mould temperature is always kept lower than $60 - 80°C$.
Low pressure injection moulding is a cheap forming process as the applied pressure and temperature in this process are relatively low.

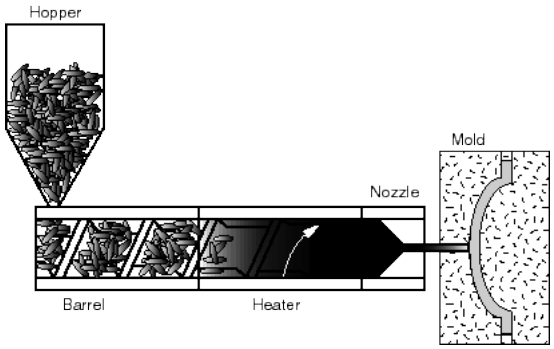

Figure V.6 : Low pressure ceramic injection moulding process.

The additives consist of low melting point and less viscous binders, such as wax and paraffin. Also, the injection temperature does not exceed $130°C$.
The main disadvantage of injection moulding process, especially for the high pressure category, is its expensive tooling cost. Consequently, this process is mostly used for high added value as well as large quantity products.

V.5 Experimental Analysis

Experimental analysis consists of different thermo-mechanical experiments:

- Densification analysis by dilatometry
- Pyroplastic behaviour analysis by sinter-bending test device of
  - Green ceramic plate-shaped samples
  - Pre-sintered (rigid) plate-shaped specimens

These experiments are essential for model parameters identification.
Furthermore, the microstructures of studied specimens have been observed by scanning

electron (SEM) microscopy and their compositions before and after sintering have been analysed by X-ray diffraction test.

V.5.1 Densification behaviour by dilatometry

The thermo-mechanical behaviour of injection moulded cylindrical-shaped specimens has been investigated by using the Setaram dilatometer.
For this purpose, small cylinders have been machined from larger cylinders to be tested in the dilatometer.

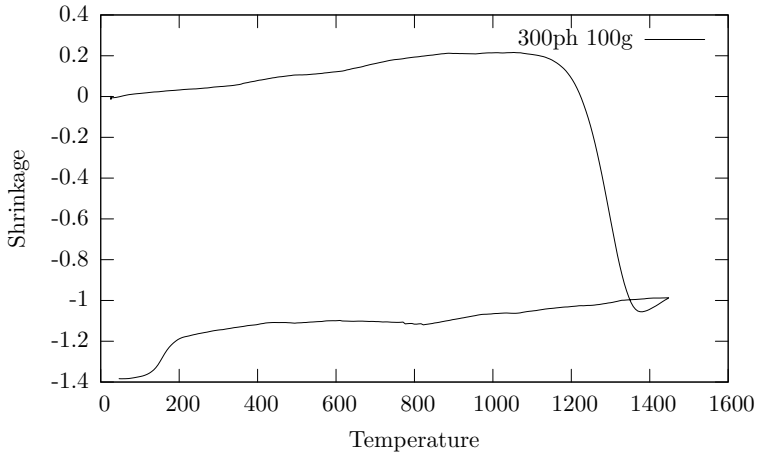

Figure V.7 : Shrinkage-temperature curve of an injection moulded sample. Applied load: 100g. Heating-cooling rate of thermal cycle: $300°C/$hour.

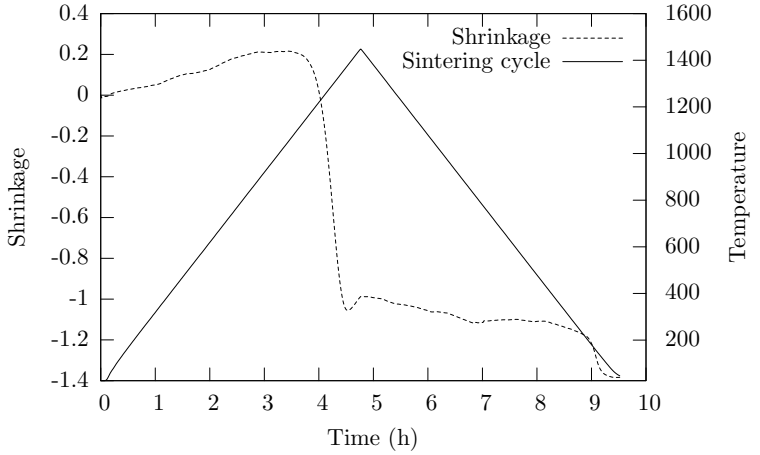

Figure V.8 : Shrinkage-time curve of cylindrical injection moulded sample and associated thermal cycle. Applied load: 100g. Heating-cooling rate of thermal cycle: $300°C/$hour.

Figures V.7, V.9, V.11 present the linear shrinkage (%) on function of temperature during the firing process. Figures V.8, V.10, V.12 show the linear shrinkage (%) as a function of time and the sintering cycle during the firing process.

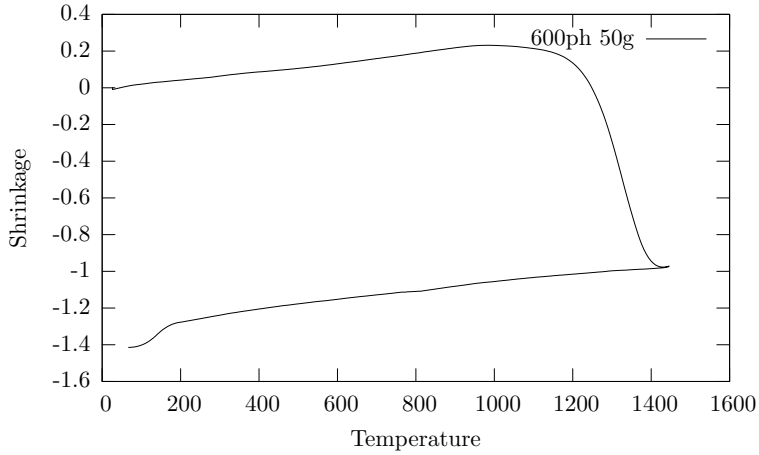

Figure V.9 : Shrinkage-temperature curve of an injection moulded sample. Applied load: 50g. Heating-cooling rate of sintering cycle: $600°C$/hour.

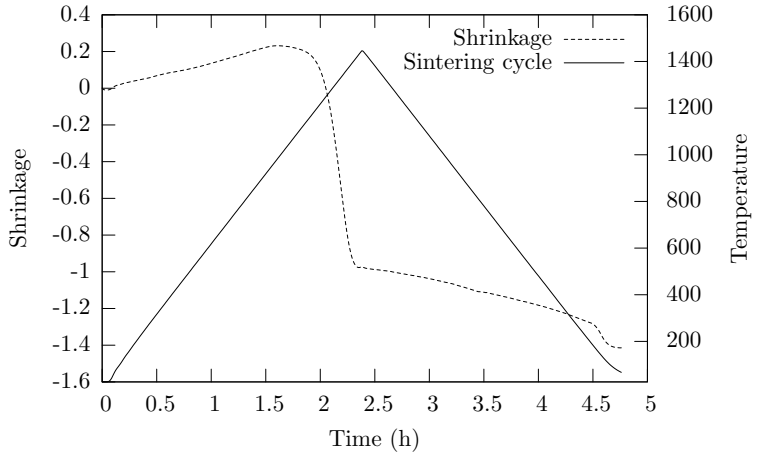

Figure V.10 : Shrinkage-time curve of cylindrical injection moulded sample and associated thermal cycle. Applied load: 50g. Heating-cooling rate of thermal cycle: $600°C$/hour.

As shown in these figures, two sintering cycles with different heating-cooling rates have been used. In both thermal cycles, the samples have been heated till $1450°C$.
Then, without any step stages, the samples have been cooled with the same rate used in the heating stage. The heating rates are $300°C$/hour and $600°C$/hour.
Moreover, in order to study the effect of an external force, two different loads have been applied during the firing process: $50g$ and $100g$.

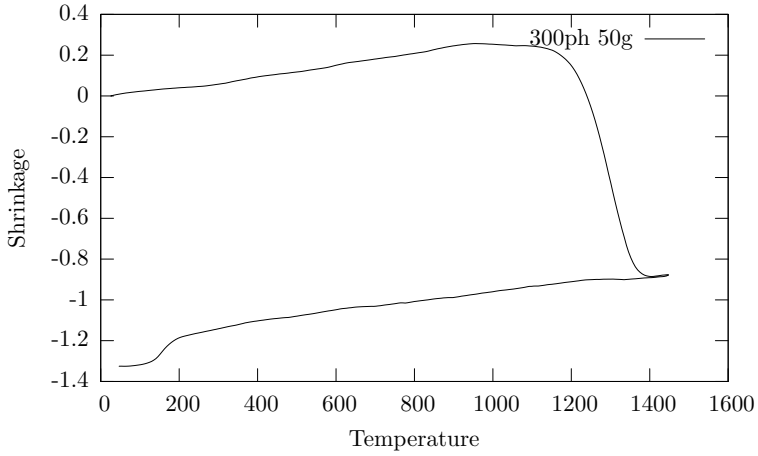

Figure V.11 : Shrinkage-temperature curve of an injection moulded sample. Applied load: 50g. Heating-cooling rate of thermal cycle: $300°C$/hour.

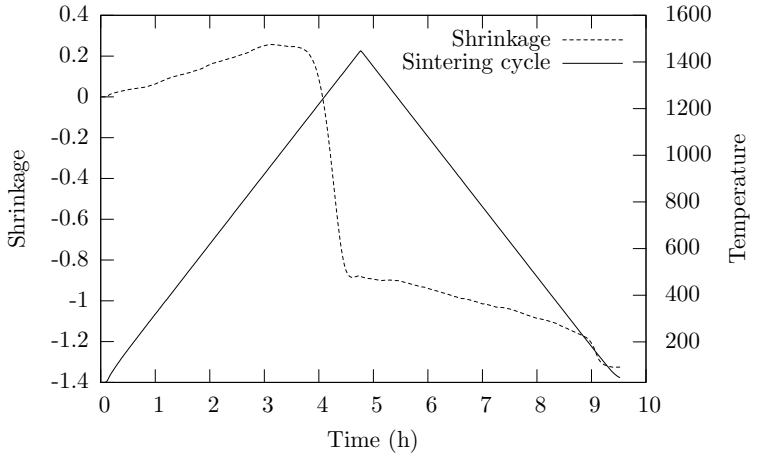

Figure V.12 : Shrinkage-time curve of cylindrical injection moulded sample and associated thermal cycle. Applied load: 50g. Heating-cooling rate of thermal cycle: $300°C$/hour.

The linear shrinkage curve of ceramic core material can be divided into 4 regions:

- Slight volume increase due to thermal expansion ($\alpha = 2.8 \times 10^{-6}\ K^{-1}$)
- Sharp drop mainly due to the sintering shrinkage which is stopped later by reactive sintering.
- Thermal shrinkage in cooling stage of sintering
- Phase transformation due to Cristobalite formation

The amount of linear shrinkage observed in all experiments with different loads and different sintering cycles is small (about 1.3%).

V.5.2 SEM observation and X-ray diffraction analysis

The microstructures of the specimens before and after thermo-mechanical analysis test have been observed by scanning electron microscopy. In order to identify the phases observed

in SEM images, X-ray diffraction analyses have been carried out on samples, before and after firing. As shown in SEM images and X-ray diffraction patterns, zircon ($ZrSiO_4$) and silica($SiO_2(\alpha)$) have been observed before and after sintering. The intensities of zircon peaks remained almost unchanged during sintering. However, the silica ($SiO_2(\alpha)$) peak increased its intensity after the sintering.

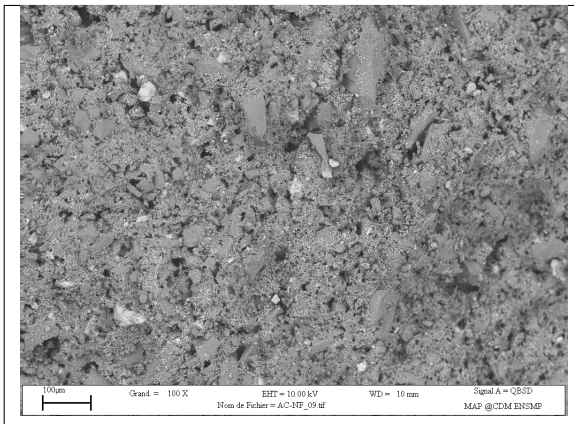	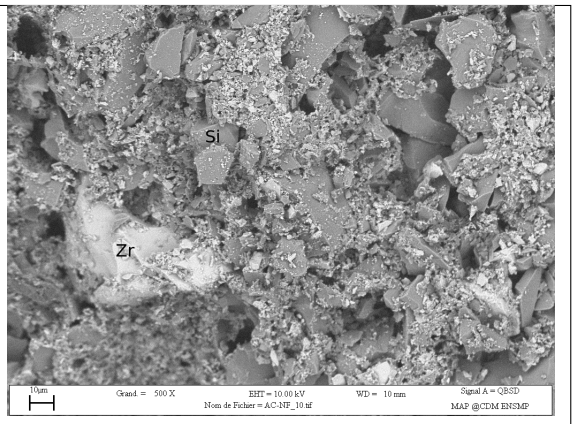
Before Sintering (100μm)	Before Sintering (10μm)
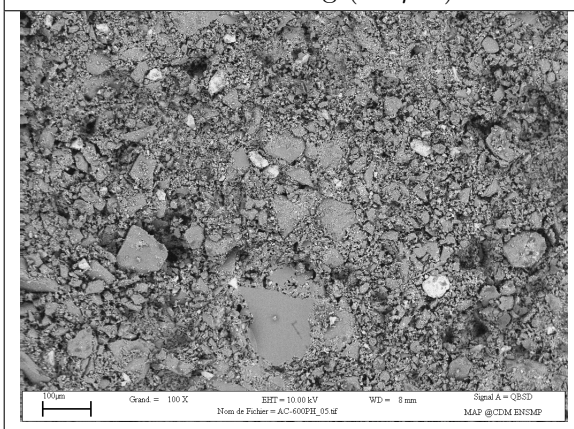	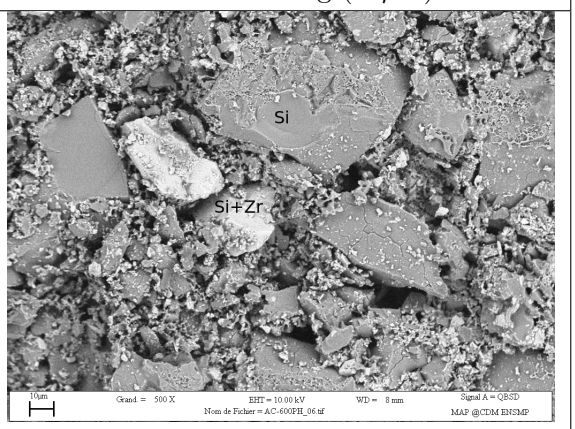
After rapid sintering (100μm)	After rapid sintering (10μm)
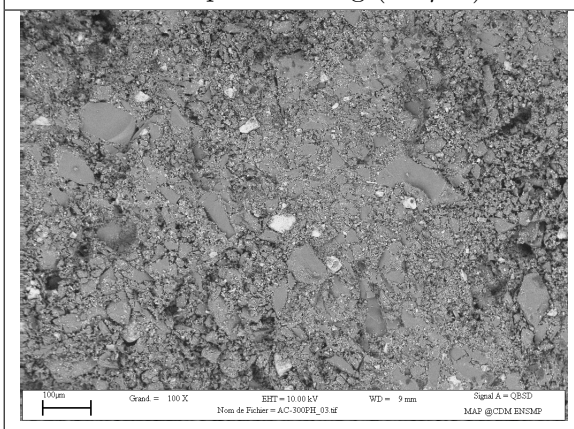	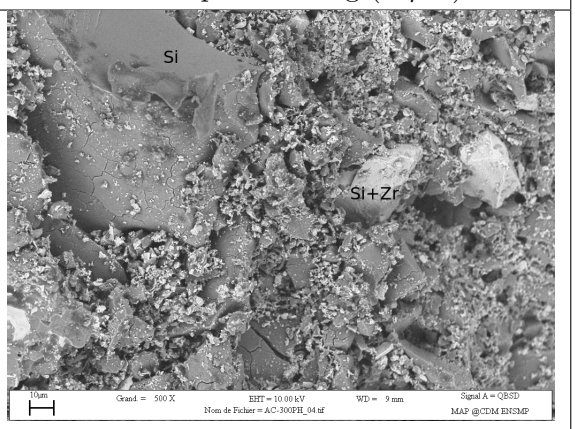
After sintering (100μm)	After sintering (10μm)

Table V.3 : Microstructure of specimens before and after sintering. In these SEM images, Si represents silica and Zr represents zircon.

The intensities of zircon peaks remain almost unchanged by the sintering. However, the silica peak increases its intensity during the sintering. The increase in the intensity of silica

phase and the expansion of silica phases observed by SEM after sintering is due to the phase transformation during which fused, amorphous silica transforms into cristobalite:

$$Fused\ amorphous\ silica \rightarrow Cristobalite \tag{V.1}$$

During the crystallization of the fused silica at high temperature, cristobalite nucleates at the surface of fused silica particles. Consequently a crystalline shell is produced which impedes further viscous flow of fused silica grains and stops the shrinkage .

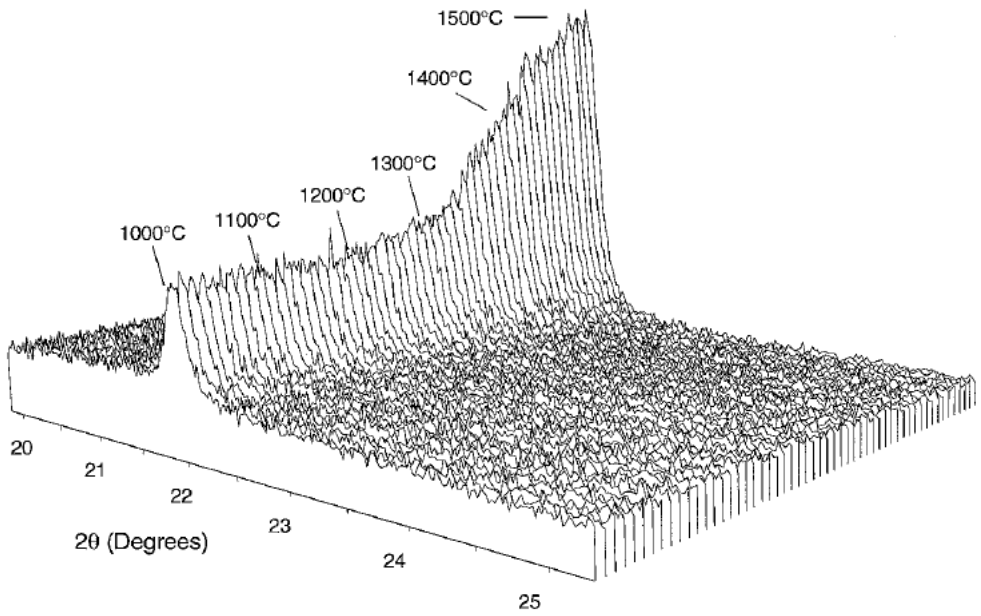

Figure V.13 : High temperature X-ray diffraction data for cristobalite. Increasing peak intensity is the evidence of cristobalite content increase during firing [wereszczak2002dimensional].

Consequently, during this phase transformation, silica undergoes a volume expansion by which the sinter shrinkage is compensated.
Other ways for limiting the shrinkage during sintering consist in using reaction-bonding process or reactive sintering. During this processes, one component undergoes a volume expansion due to a chemical reaction which compensates the shrinkage induced by sintering [hennige1999shrinkage, kaiser2008thermal].

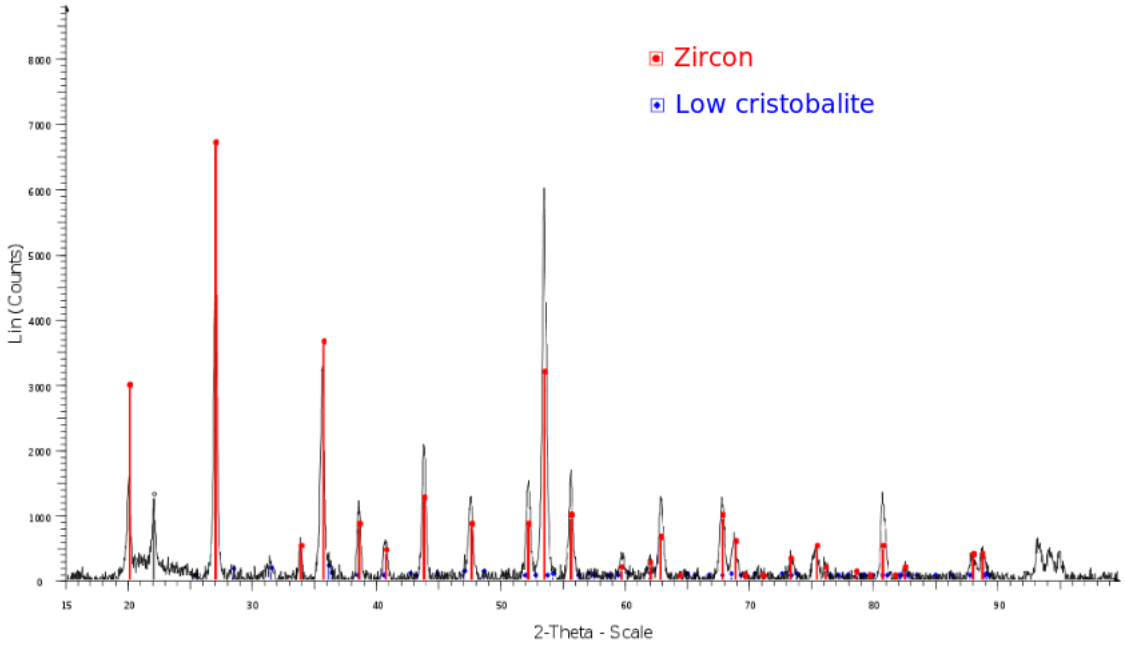

Figure V.14 : X-ray diffraction pattern of sample before sintering.

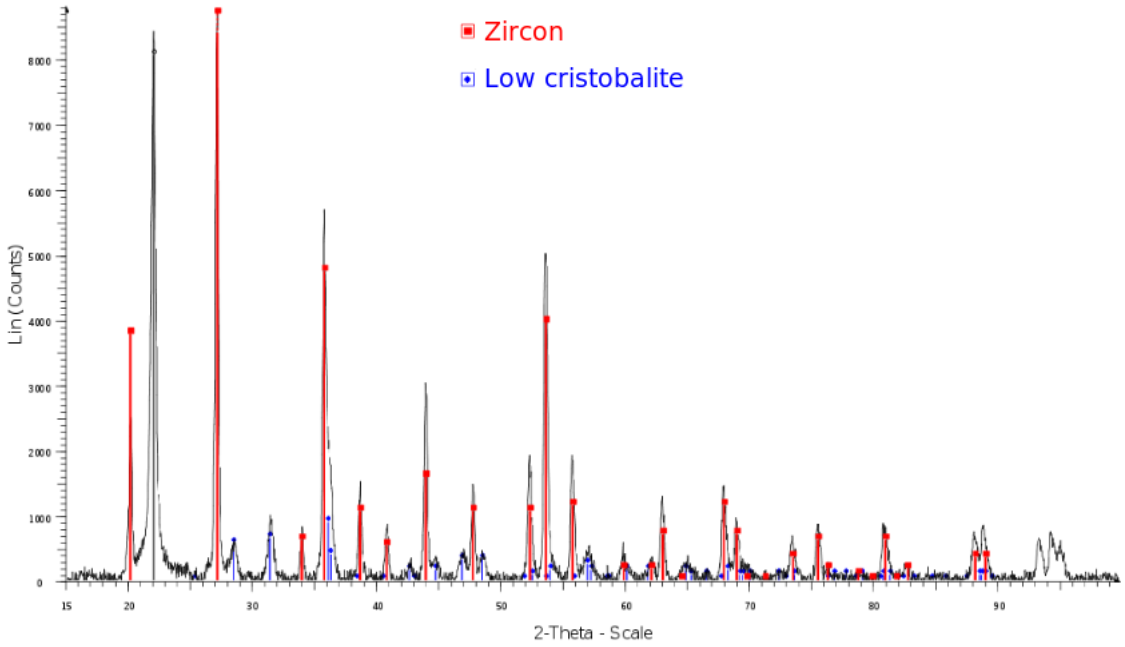

Figure V.15 : X-ray diffraction pattern of sample after sintering.

In order to analyse the silica transformation during the firing process, high-temperature X-ray diffraction analysis is a powerful tool. Chao *etal* and Wereszczak *etal* have studied the transformation of silica based ceramic cores as a function of sintering temperature. Figure V.16 and V.13 illustrate the variation of α-cristobalite quantity in sintered ceramic cores [chao2002optimal, wereszczak2002dimensional].

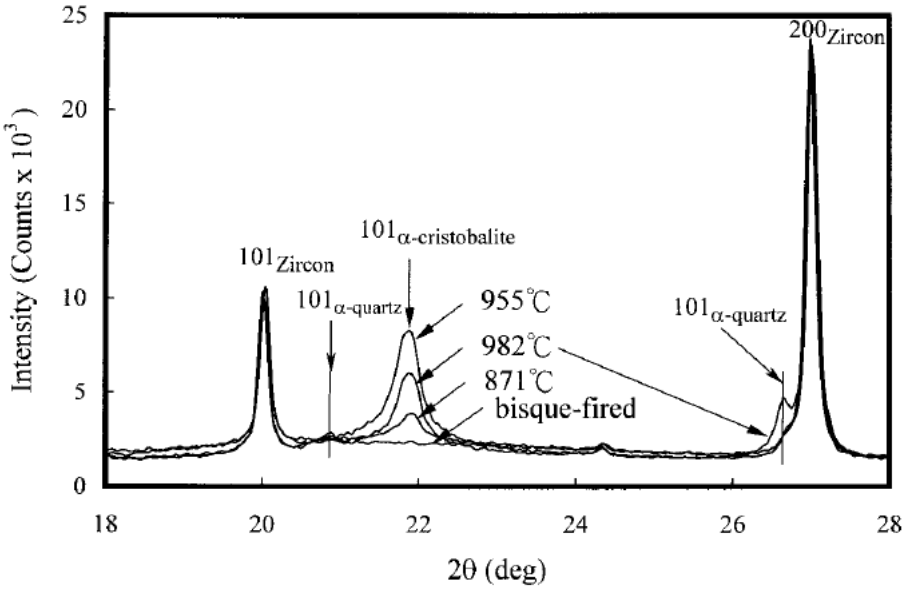

Figure V.16 : X-ray diffraction pattern illustrating the variation of α-cristobalite quantity during sintering of ceramic cores
[chao2002optimal].

This X-ray diffraction pattern indicates that the amount of crystalline silica phase increases during the firing process while zircon stays almost unaffected. The same phenomenon can be observed in our X-ray diffraction results (Figures V.14 and V.15).
In conclusion, the crystallisation rate of cristobalite during sintering should be used as the internal variable of the constitutive model instead of porosity change.

V.5.3 Pyroplastic behaviour of ceramic cores

The pyroplastic behaviour analysis of injection moulded ceramic cores is presented in this part. Figures V.17 and V.18 show the ceramic beam sample before and after sintering respectively.

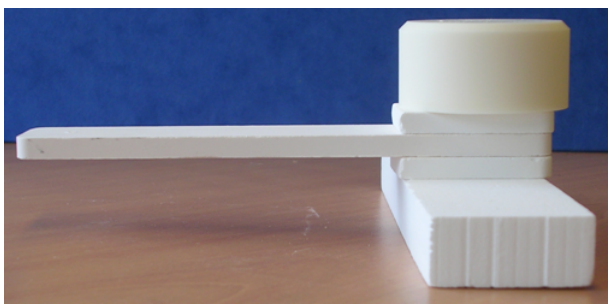

Figure V.17 : Cantilever beam before sintering.

This cantilever structure prepared by assembling three non-sintered plates, has been fired in an electrical furnace while the beam deflection is measured by laser beam.

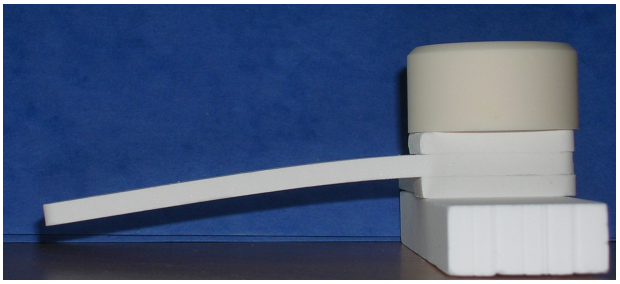

Figure V.18 : Cantilever beam after sintering.

Three different sintering cycles have been used in order to analyse the effect of sintering time and temperature as well as heating-cooling rate on beam deflection. Deflection graphs measured during these three experiments and the associated sintering cycles have been plotted in the following figures:

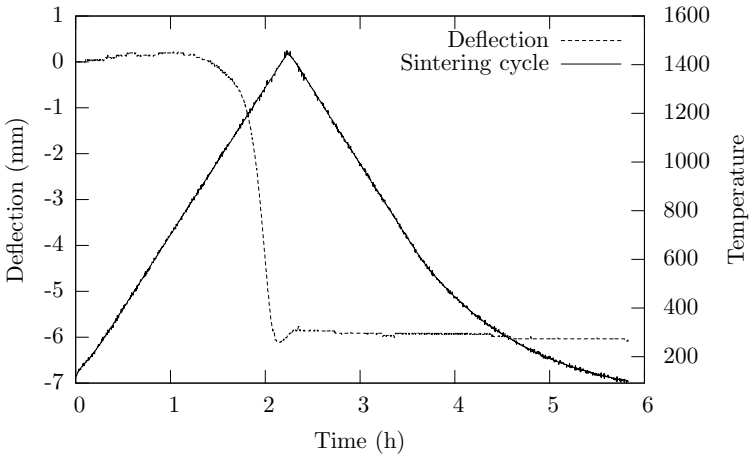

Figure V.19 : Sinter-bending experiment; Maximum temperature: 1400°C and heating rate: 600°C/hour.

The first sintering cycle represented in figure V.19 consists of a heating stage till 1400°C and a cooling stage with a rate of 600°C/hour. In this test, the deflection starts at 1100°C and reaches a maximum bending of 6 mm at the end of the firing process.

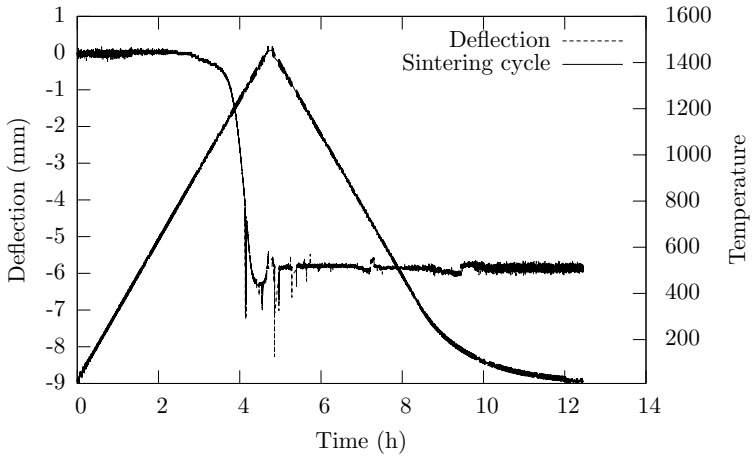

Figure V.20 : Sinter-bending experiment; Maximum temperature: 1400°C and heating rate: 300°C/hour.

The second test is presented in figure V.20. The sintering cycle has a heating and a cooling stages with a maximum temperature of 1400°C and a heating rate of 300°C/hour.

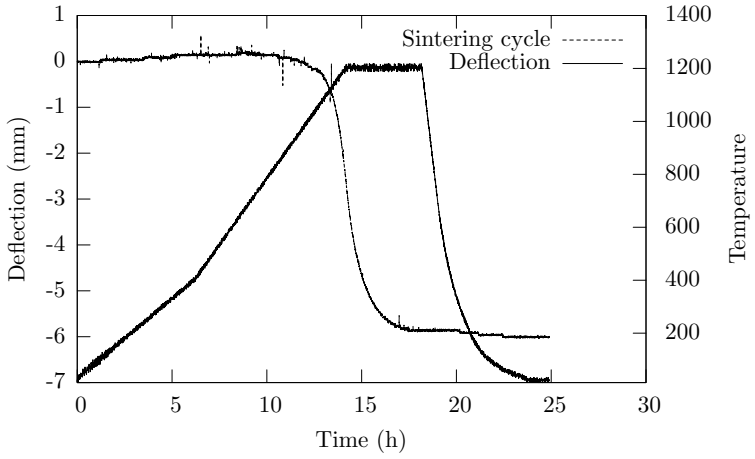

Figure V.21 : Sinter-bending experiment with 5h step stage at 1200°C.

The third sintering cycle is composed of a heating stage, 5 hours step stage at 1200°C and a natural cooling part (Figure V.21).
In all these sinter-bending tests, the deflection is about 6 mm. It seems that the high temperature bending of the ceramic core beam has been blocked by an external cause such as a phase transformation. This phase transformation can be associated with the crystallisation of cristobalite which blocks the viscous flow of the ceramic beam during sintering.
In order to perform a more detailed analysis, another experiment has been performed in which a rigid (fully fired) ceramic beam with a cantilever structure undergoes a sinter-bending test. It should be noted that this plate has been previously sintered on a flat rigid substrate.

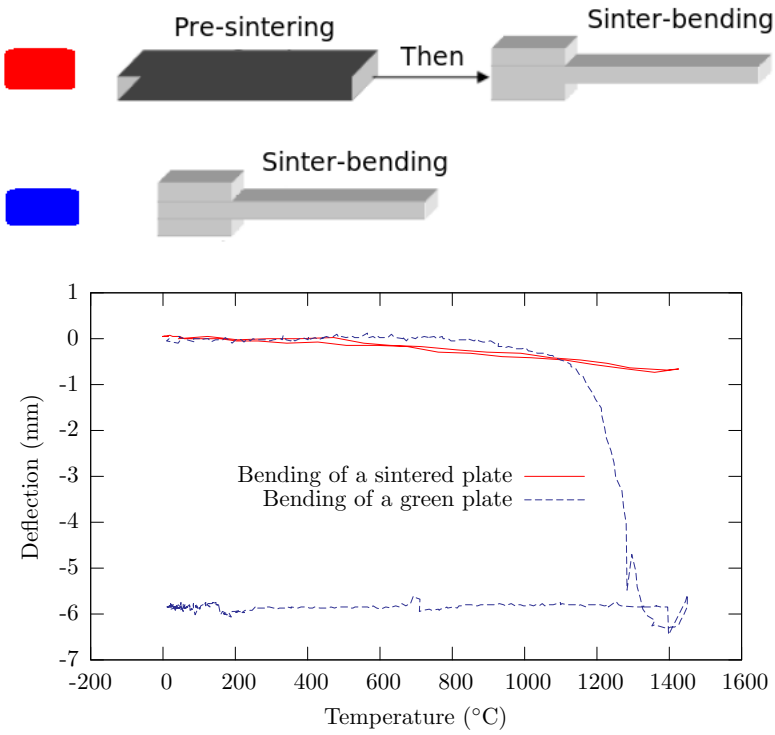

Figure V.22 : Bending curves recorded for a sintered ceramic plate and a green (non-sintered) ceramic plate for a given sintering cycle.

As illustrated in figure V.22, the fully sintered beam does not deform during sinter-bending test.
Experimental results of pyroplastic analysis and thermo-mechanical analysis can be summarized as:

- Heating rate does not influence the deflection of beam during sinter-bending test.
- The amount of deflection is the same for different firing cycles till 1400°C.
- A pre-fired ceramic beam does not deform during sinter-bending experiment.
- Ceramic core materials undergo little shrinkage (1.3%) during sintering.
- Sintering stops at 1400°C.
- External applied loads does not influence sintering deformation.

According to these results, a constitutive model has been proposed which is described in the next part.

V.6 Constitutive model of reactive sintering

The strain tensor $\underline{\dot{\varepsilon}}$ is assumed to be a sum of different terms and is expressed as:

$$\underline{\dot{\varepsilon}} = \underline{\dot{\varepsilon}}_e + \underline{\dot{\varepsilon}}_{th} + \underline{\dot{\varepsilon}}_s + \underline{\dot{\varepsilon}}_c \tag{V.2}$$

$\underline{\dot{\varepsilon}}_{th}$ is the thermal strain tensor:

$$\underline{\varepsilon}_{\text{th}} = \alpha(T)(T - T_{\text{ref}})\underline{1} \tag{V.3}$$

It is assumed that a chemical reaction occurs within the material (cristobalite formation). The advancement of this chemical reaction is denoted as χ. The evolution for χ is expressed as:

$$\dot{\chi} = \beta \left(\chi_\infty - \chi\right)^\alpha \tag{V.4}$$

in which χ_∞ is the maximum advancement of reaction ($\chi_\infty = 1$)and χ is the instantaneous reaction progress. β may also depend on temperature:

$$\beta = \beta_0 exp(\frac{-Q}{RT}) \tag{V.5}$$

The elastic strain tensor $\underline{\varepsilon}_e$ is related to the stress tensor $\underline{\sigma}$ by the Hooke's law :

$$\underline{\sigma} = \underline{\underline{C}} : \underline{\varepsilon}_e \tag{V.6}$$

where $\underline{\underline{C}}$ is the fourth order elasticity tensor.
The sintering strain is assumed to be fully controlled by the chemical reaction:

$$\underline{\varepsilon}_s = \chi \underline{\varepsilon}_s^0 \tag{V.7}$$

where $\underline{\varepsilon}_s^0$ is the sintering strain after completion of the chemical reaction.
Similarly creep can only occur while the chemical reaction is occurring. Consequently the creep strain rate tensor is given by:

$$\dot{\underline{\varepsilon}}_c = \frac{3}{2} \mu \dot{\chi} \underline{s} \tag{V.8}$$

where $\underline{s}$ is the stress deviator. This equation implies that creep deformation occurs only if the chemical reaction is occurring (i.e. $\dot{\chi} > 0$) and stresses exist (i.e. $\underline{s} \neq \underline{0}$). μ is a material parameter.
The following parameters should be identified by optimisation method: $\underline{\varepsilon}_s^0$, α, β_0, μ and activation energy Q.
The parameter identification from experimental results (dilatometry and sinter-bending test) is presented in the next section.

V.7 Model parameter identification

The experimental results have been used for determining the reactive sintering model parameters. An optimisation algorithm is used to determine the coefficients of the model by adjusting numerical simulations to experimental result. For this purpose, the densification curves (shrinkage) have been used for determining the coefficients associated with sintering part of the model: $\underline{\varepsilon}_s^0$, α, β_0 and activation energy Q.
Similarly, deflection curves derived from sinter-bending experiment are used in order to obtain μ.
The numerical and experimental graphs after optimisation are illustrated in the following figures:

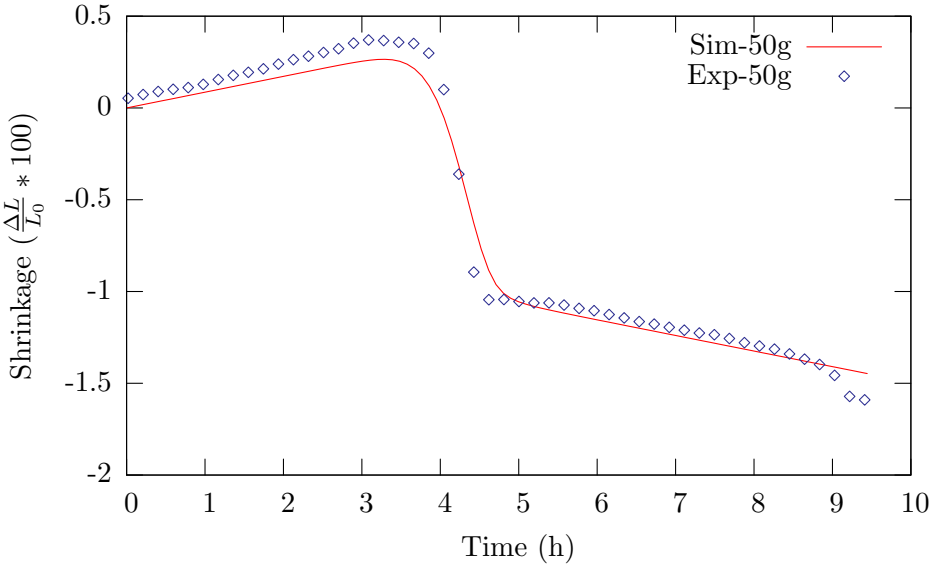

Figure V.23 : Numerical and experimental densification curves after optimization (Dilatometry with 50g load).

Figure V.23 shows the numerical and experimental curves of densification experiment using 50g load. The same experiment with 100g load is shown in figure V.24

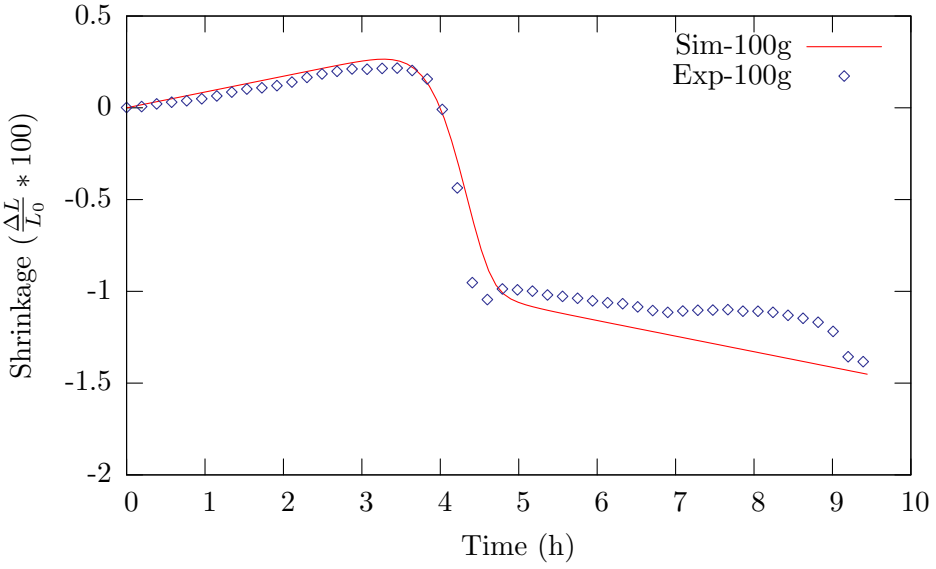

Figure V.24 : Numerical and experimental densification curves after optimization (Dilatometry with 100g load).

The experimental beam deflection curve obtained from sinter-bending test and the associated numerical graph after optimisation are shown in figure V.25.

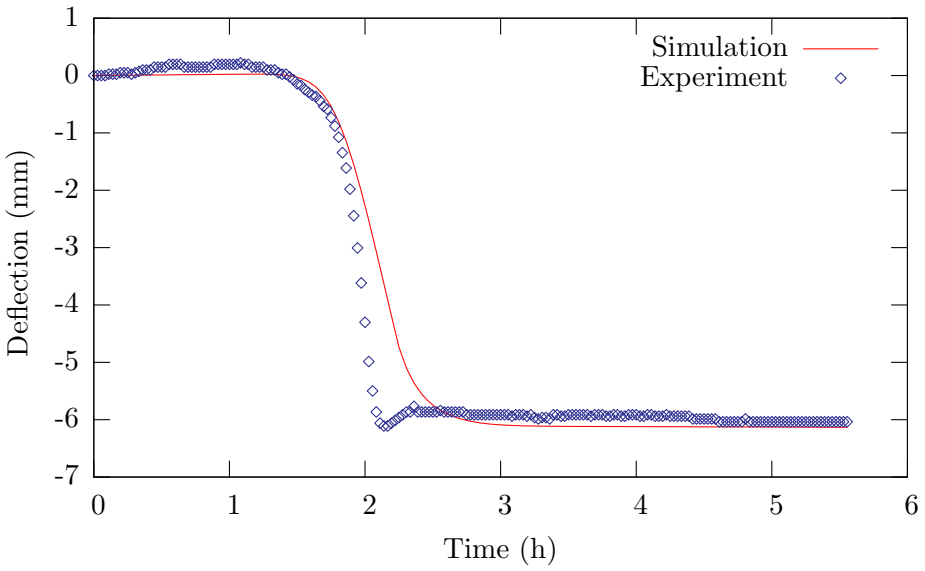

Figure V.25 : Numerical and experimental sinter-bending curves after optimization.

The five model parameters identified by adjusting numerical simulations to experimental results are presented in table V.4. The thermal expansion coefficient has been also calculated from densification (dilatometry) curves.

Parameter	Values
$\varepsilon_s^0 \underline{1}$	-0.242
α	56
$\beta 0$	$3.991e+02\ s^{-1}$
μ	7.808
Activation Energy	$2.032e+05\ J$
Thermal expansion coefficient	$2.85e-06\ K^{-1}$

Table V.4 : Model parameters after optimisation.

The numerical simulation of a step shaped part made by injection moulding of ceramic core material (zircon-silica) is presented in the next section. This simulations have been carried out using the mentioned optimised parameters.

V.8 Finite element simulation of a step-shaped test part

In this section, the finite element simulation of a step shaped industrial test part manufactured by injection moulding process is discussed. As the computer aided design of a real investment casting core is complicated and restricted by confidentiality, it has been decided to simulate a test part representative of a real ceramic core during sintering.

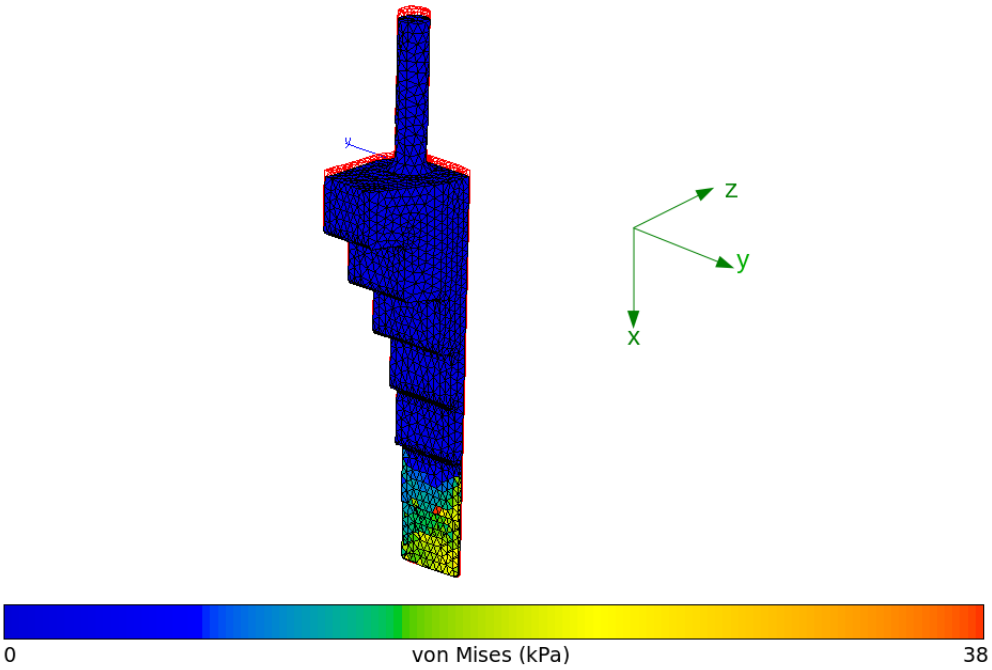

Figure V.26 : Numerical simulation of a step-shaped test part representative of a turbine blade ceramic core.

Sintering of ceramic cores is carried out in large containers of powders. The core surrounded by powder materials is sintered in special furnaces. Due to confidential restrictions no accurate technical information has been transferred to us by our industrial partner.
Figure V.26 shows the von Mises stress field and the deformation during sintering of a step-shaped test part. As shown, the test part undergoes a little shrinkage and it deforms while the chemical reaction is happening. The von Mises stress varies between zero and some kPa. In this simulation, gravity is applied along x direction.

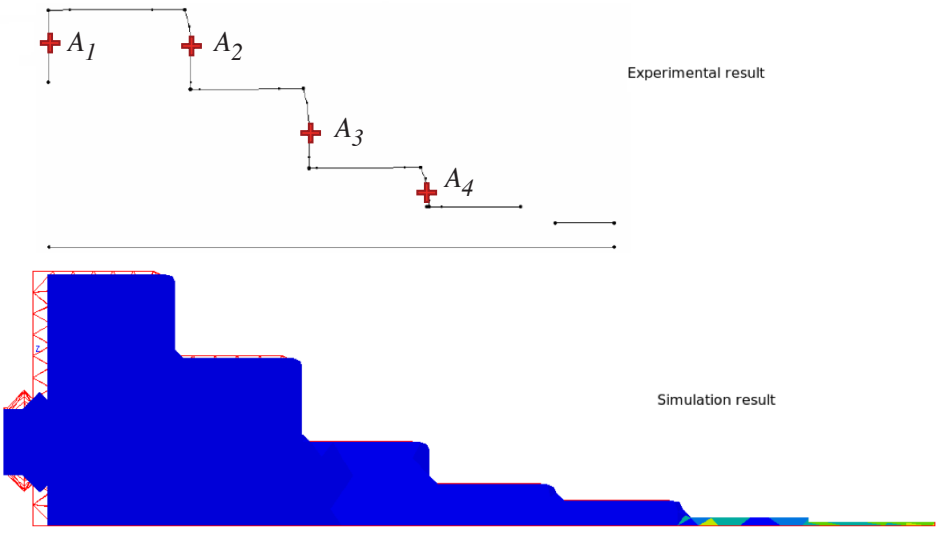

Figure V.27 : Comparison between the numerical simulation and the experimental result.

Figure V.27 shows the comparison between the numerical simulation and experimental result after firing process. The experimental result is obtained by scanning the sintered body after firing process using a digital CMM (Coordinate Measurement Machine) laser scanner. As shown in this figure, the final shape of the step-shaped part is quite similar to the numerical results obtained by finite element simulation. Unfortunately, the right end of the part has been broken during transport and is not available for comparison with numerical simulation.

Relative Errors
$\frac{\lvert(A_1A_2)_{FE}-(A_1A_2)_{exp}\rvert}{(A_1A_2)_{exp}}$ 7.7 %
$\frac{\lvert(A_1A_3)_{FE}-(A_1A_3)_{exp}\rvert}{(A_1A_3)_{exp}}$ 1.7 %
$\frac{\lvert(A_1A_4)_{FE}-(A_1A_4)_{exp}\rvert}{(A_1A_4)_{exp}}$ 0.8 %

Table V.5 : The relative errors of the prediction of the length.

The relative errors of the prediction of the length $(A_1A_i)_{i=1}^4$ are shown in table V.5. The greater the index i, the lower the error. The creep term of the total strain being higher in the lower part of the step (i.e. higher between A_3 and A_4 than between A_1 and A_2), these results show a good agreement when creep strains are significant. But here the strain prediction is not satisfactory in case of almost pure sintering strains (between A_1 and A_2).

V.9 Conclusion

This chapter is devoted to the study of ceramic cores used for investment casting of turbine blade super-alloys. It begins by a brief description of investment casting and injection moulding processes as well as a short literature review of ceramic material composition used for manufacturing high temperature resistant cores and shells.
Experimental results of the thermo-mechanical and the pyroplastic analyses obtained by dilatometry and sinter-bending tests are explained. According to these results, a phenomenological constitutive model of reactive sintering has been developed and implemented in Zset finite element program. Finally, the parameter identification process and a finite element simulation of a step-shaped test part have been discussed.

Summary in French

Ce chapitre est consacré à l'étude des noyaux céramiques utilisés pour la fonderie en cire perdue de superalliages d'aubes de turbine.
Il commence par une brève description des procédés de fonderie en cire perdue et du moulage par injection, ainsi qu'une introduction aux matériaux céramiques utilisés pour la fabrication des noyaux résistants à haute température.
Ensuite les résultats expérimentaux des analyses thermo-mécanique et pyroplastique obtenus par des essais de dilatométrie et de flexion-frittage sont expliqués. A partir de ces résultats, une loi de comportement phénoménologique de frittage réactif est développée et implémentées dans le code de calcul par éléments finis ***Zset****.*
Enfin, les paramètres du modèle ont été identifiés par ajustement des résultats expérimentaux et le calcul par éléments finis d'une pièce en forme d'escalier représentative d'un noyau céramique a été réalisé.

Chapter -VI-

APHR application and model parameter sensitivity of isotropic sintering constitutive law

Arch Comput Methods Eng (2010) 17: 455–463
DOI 10.1007/s11831-010-9055-0

ORIGINAL PAPER

Truncated Integration for Simultaneous Simulation of Sintering Using a Separated Representation

B. Sarbandi · S. Cartel · J. Besson · D. Ryckelynck

Received: 15 March 2010 / Accepted: 15 March 2010 / Published online: 6 October 2010

Abstract Recent developments of multidimensional solvers using separated representation make it possible to account for the multidimensionality of mechanical models in materials science when doing numerical simulations. This paper aims to extend the separated representation to inseparable equations using an efficient integration scheme. It focuses on the dependence of constitutive equations on material coefficients. Although these coefficients can be optimized using few experimental results, they are not very well known because of the natural variability of material properties. Therefore, the mechanical state can be viewed as a function depending not only on time and space variables but also on material coefficients. This is illustrated in this paper by a sensitivity analysis of the response of a sintering model with respect to variations of material coefficients. The considered variations are defined around an optimized value of coefficients adjusted by experimental results. The proposed method is an incremental method using an extension of the integration scheme developed for the Hyper Reduction method. During the incremental solution, before the adaptation of the representation, an assumed separation representation is used as a reduced-order model. We claim that a truncated integration scheme enables to forecast the reduced-state variables related to the assumed separated representation. The fact that the integrals involved in the formulation can not be written as a sum of products of one-dimensional integrals, this approach reduces the extent of the integration domain.

B. Sarbandi · S. Cartel · J. Besson · D. Ryckelynck (✉)
Centre des Materiaux, Mines ParisTech, CNRS UMR 7633,
BP 87, 91003 Evry, France
e-mail: david.ryckelynck@ensmp.fr

1 Introduction

Sintering is a key part for producing materials in a useful and robust form, especially ceramics and generally porous materials, and involves heating the porous structure or a powder compact. During this thermal treatment cycle, the part tends to increase in density as sintering proceeds and this still further improves the mechanical properties. Density increasing implies, of course, an overall shrinkage which leads to complex deformations. The shrinkage and deformation of ceramic body during this firing process can be simulated by sintering deformation constitutive model [1]. The thermal and mechanical parameters of the constitutive model should be determined experimentally and introduced in corresponding finite element analysis. It is obvious that whereas the results of finite element simulation of sintering deformation will be significantly affected by variations in some of these parameter values, the effect of similar variations in other parameter values will be of little consequences. Consequently, investigation of the effect of parameter variations are important in so far as they provide a guide to the level of uncertainty of the parameters. In other words, the parameters that have the smallest effect could be identified for a large class of materials. The parameters having a greater effect should be specified with greater accuracy for each considered materials. We propose to quantify how sensitive the results of a finite element analysis were to disturbance of the mechanical parameters of the sintering constitutive model. Therefore, the mechanical state can be viewed as a function depending not only on time and space variables but also on material coefficients, in the framework of multidimensional modeling.

Multidimensional modeling of materials seems to be an appealing approach thanks to the recent works of F. Chinesta, A. Ammar and co-authors [2, 3] on separated-

representation-based algorithms. This kind of representation was applied in numerous contexts: (i) quantum chemistry [4]; (ii) Brownian dynamics [5]; (iii) kinetic theory description of polymers solutions and melts [6]; and kinetic theory descriptions of rods suspensions [7]. In this paper the multidimensionality of the model is related to the variability of the material properties.

By using a separated representation it is assumed that equilibrium equations are not rigorously fulfilled. The purpose of this work does not concern the convergence of such representation. It is shown the ability of the proposed method to efficiently estimate the mechanical variables using a separated representation and a truncated integration scheme. For this reason the residue of the equilibrium equations is introduced in the following formulations. The goal of numerical simulation is to forecast a mechanical state related to residue small enough or as small as possible. Considering inseparable equation the method is quite generic. The second section is about the generic formulation of the mechanical problem. The third section explains the truncated integration scheme involved in the separated-representation-based algorithm. The fourth section gives the details of the constitutive model of sintering and the related parameters. The fifth section presents the numerical results and a comparison to a classical FEM. And finally the conclusion is discussed in the sixth section.

2 Formulation of the Continuous Model Using Separated Representation

A generic form of continuous mechanical model is considered, which is a parameterized nonlinear model. $\{p\}$ denotes the column of the model parameters, which are material coefficients. The purpose of the proposed method is to estimate the mechanical state as a function defined in the multidimensional space $\Omega^0 \times \mathcal{P} \times]t_0, t_f]$, where Ω^0 is the reference configuration of the mechanical system, $\mathcal{P}$ is the manifold related to the model parameters and $]t_0, t_f]$ is the time interval. The continuous model is described using the finite strain formalism. The reference configuration Ω^0 can be the domain either at time $t = 0$ (total Lagrangian formulation) or at time t (updated Lagrangian formulation). In order to facilitate the implementation of the method into an existing code, we preserve an incremental scheme. At time instant t, the continuous medium is occupying a domain Ω. The approximated displacement field at time t is defined on $\Omega^0 \times \mathcal{P}$ and it is denoted by $\underline{\boldsymbol{u}}(\underline{\boldsymbol{X}}, \{p\}, t)$. $\underline{\boldsymbol{X}}$ is denoting the initial position of a material point in Ω^0. It is represented using the following separated representation:

$$\underline{\boldsymbol{u}}(\underline{\boldsymbol{X}}, \{p\}, t) = \sum_{j=1}^{j=\gamma} \underline{\boldsymbol{\phi}}_j(\underline{\boldsymbol{X}}) g_j(\{p\}) a_j(t) + \underline{\boldsymbol{u}}_c(\underline{\boldsymbol{X}}, t)$$
$$\forall \underline{\boldsymbol{X}} \in \Omega^0 \; \forall \{p\} \in \mathcal{P} \; \forall t \in]0, T] \tag{1}$$

where $\underline{\boldsymbol{u}}_c(\underline{\boldsymbol{X}}, t)$ is a given function such that Dirichlet conditions defined on $\partial_U \Omega^0 \times \mathcal{P}$ are fulfilled, $\underline{\boldsymbol{\phi}}_j(\underline{\boldsymbol{X}})$ is a displacement field defined in $H^1(\Omega^0)$, $g_j(\{p\})$ is a scalar function defined in $L^2(\mathcal{P})$, and $a_j(t)$ is a scalar continuous time function. $\underline{\boldsymbol{u}}_c$ is a continuous function of the variable $\underline{\boldsymbol{X}}$ equal to zero almost everywhere in Ω^0 such that $\underline{\boldsymbol{u}}_c$ is equal to the given Dirichlet conditions at any point of $\partial_U \Omega^0 \times \mathcal{P}$. Therefore $\underline{\boldsymbol{\phi}}_j(\underline{\boldsymbol{X}}) = 0$ over $\partial_U \Omega^0$. The displacement field belongs to an affine function space $\mathcal{U}$ defined by:

$$\mathcal{U} = \left\{ \begin{array}{l} \underline{\boldsymbol{u}}(.,.,t) \in H^1(\Omega^0) \otimes L^2(\mathcal{P}) | \\ \exists (\underline{\boldsymbol{\phi}}_j)_{j=1,\ldots,\gamma}, \exists (g_j)_{j=1,\ldots,\gamma}, \exists (a_j)_{j=1,\ldots,\gamma}, \\ \underline{\boldsymbol{u}}(\underline{\boldsymbol{X}},.,t) = \underline{\boldsymbol{u}}_c(\underline{\boldsymbol{X}}, t) \; \forall \underline{\boldsymbol{X}} \in \partial_U \Omega^0 \\ \underline{\boldsymbol{u}}(\underline{\boldsymbol{X}}, \{p\}, t) = \sum_{j=1}^{j=\gamma} \underline{\boldsymbol{\phi}}_j(\underline{\boldsymbol{X}}) g_j(\{p\}) a_j(t) + \underline{\boldsymbol{u}}_c(\underline{\boldsymbol{X}}, t) \end{array} \right\} \tag{2}$$

A vector space denoted $\mathcal{V}$ is introduced such that:

$$\mathcal{V} = \left\{ \underline{\boldsymbol{u}}^*(.,.,t) \in H^1(\Omega^0) \otimes L^2(\mathcal{P}) | \; \underline{\boldsymbol{u}}^*(\underline{\boldsymbol{X}},.,t) = 0 \; \forall \underline{\boldsymbol{X}} \in \partial_U \Omega^0 \right\} \tag{3}$$

The second Piola-Kirchhoff stress tensor $\underset{\sim}{\boldsymbol{S}}$ is a nonlinear function of the deformation gradient history depending on the parameters $\{p\}$:

$$\underset{\sim}{\boldsymbol{S}} = \underset{\sim}{\boldsymbol{\Sigma}}(\underset{\sim}{\boldsymbol{F}}_\tau, \tau \leq t; \{p\}) \tag{4}$$

where $\underset{\sim}{\boldsymbol{\Sigma}}$ is a formal operator that must be defined by constitutive equations and $\underset{\sim}{\boldsymbol{F}}_\tau$ is the deformation gradient at time instant τ. Consequently the following general relations are fulfilled:

$$F_{ij} = \delta_{ij} + \frac{\partial u_i}{\partial X_j} \tag{5}$$

$$\underset{\sim}{\boldsymbol{\sigma}} = \frac{1}{\det(\underset{\sim}{\boldsymbol{F}})} \underset{\sim}{\boldsymbol{F}} . \underset{\sim}{\boldsymbol{S}} . \underset{\sim}{\boldsymbol{F}}^T, \tag{6}$$

where $\underset{\sim}{\boldsymbol{\sigma}}$ is the Cauchy stress tensor and δ_{ij} is the Kronecker delta.

The boundary $\partial \Omega^0$ of Ω^0 is denoted by $\partial_U \Omega^0 \cup \partial_f \Omega^0$. On $\partial_f \Omega^0$, there is a given force field $\underline{\boldsymbol{f}}(.,t)$ depending on time t. The statement of the mechanical problem is presented in the following equations whose purpose is to find an

estimation of the displacement field $\underline{\boldsymbol{u}} \in \mathcal{U}$ related to a given degree of precision ϵ_r which is defined by the constitutive equations and the principle of virtual work:

$$\begin{aligned}&\int_{\Omega^0\times\mathcal{P}} \underset{\sim}{\boldsymbol{\varepsilon}}(\underline{\boldsymbol{u}}^*,\underline{\boldsymbol{u}}) : \underset{\sim}{\boldsymbol{\Sigma}}(\underset{\sim}{\boldsymbol{F}}(\underline{\boldsymbol{u}}),\tau\le t,\{p\})\,d\Omega^0\,dp \\ &\quad -\int_{\partial_f\Omega^0\times\mathcal{P}} \underline{\boldsymbol{u}}^*.\underline{\boldsymbol{f}}(\underline{\boldsymbol{X}},t)\,d\Gamma^0\,dp \\ &= \int_{\Omega^0\times\mathcal{P}} \underline{\boldsymbol{u}}^*.\underline{\boldsymbol{r}}_v\,d\Omega^0\,dp \\ &\quad +\int_{\partial_f\Omega^0\times\mathcal{P}} \underline{\boldsymbol{u}}^*.\underline{\boldsymbol{r}}_b\,d\Gamma^0\,dp \quad \forall \underline{\boldsymbol{u}}^*\in\mathcal{V}\ \forall t\in\,]t_0,t_f] \end{aligned} \tag{7}$$

with the following accuracy condition:

$$\begin{aligned}&\int_{\Omega^0\times\mathcal{P}} \underline{\boldsymbol{r}}_v.\underline{\boldsymbol{r}}_v\,d\Omega^0\,dp \\ &\quad +\int_{\partial_f\Omega^0\times\mathcal{P}} \underline{\boldsymbol{r}}_b.\underline{\boldsymbol{r}}_b\,d\Gamma^0\,dp \le \epsilon_r \quad \forall t\in\,]t_0,t_f] \end{aligned} \tag{8}$$

where $\underline{\boldsymbol{u}}^*$ is a test function and $\underset{\sim}{\boldsymbol{\varepsilon}}$ is linear function of $\underline{\boldsymbol{u}}^*$ such that:

$$\begin{aligned}&\varepsilon_{ij}(\underline{\boldsymbol{u}}^*,\underline{\boldsymbol{u}}) \\ &= \frac{1}{2}\left(\frac{\partial u_i^*}{\partial X_j}+\frac{\partial u_j^*}{\partial X_i}+\sum_{k=1}^{k=3}\left(\frac{\partial u_k^*}{\partial X_i}\frac{\partial u_k}{\partial X_j}+\frac{\partial u_k}{\partial X_i}\frac{\partial u_k^*}{\partial X_j}\right)\right) \end{aligned} \tag{9}$$

The smaller the residuals $\underline{\boldsymbol{r}}_v$ and $\underline{\boldsymbol{r}}_b$ the better the equilibrium conditions (7) are fulfilled. According to the framework of the irreversible thermodynamic processes, a constitutive law can be defined by a choice of: internal variables $\underset{\sim}{z}$ and a free energy $w(\underset{\sim}{\boldsymbol{\varepsilon}},\underset{\sim}{z},\{p\})$ [8]. Some conjugated variables $\underset{\sim}{\boldsymbol{Z}}$ are associated with the internal variables $\underset{\sim}{z}$ using the definition of the dissipation. Examples of elastoplastic or elastoviscoplastic constitutive models can be found in [9, 10]. The detailed equations of the constitutive law related to sintering transformation are given in Sect. 4. It is clear that the existence of the solution of the approximate problem defined by (7) to (9) depends on the value of ϵ_r when the solution of the exact problem can not be represented using a finite sum as proposed in (1). The convenient choice of ϵ_r is an open question which is not addressed in this paper. We assume that ϵ_r is such that a solution of the approximate problem exists.

3 Formulation Using a Truncated Integration Scheme

The solution (1) is not given in advance but is computed adaptively. The key point of an efficient determination of the separated representation is the use of convenient test functions. Usually, the set of equations involved in (4) to (7) are not separable equations because no separated representation of the stress tensor $\underset{\sim}{\boldsymbol{S}}$ can be chosen without introducing new error approximation. Therefore, it is not possible to simplify the computation of the integrals defined over $\Omega^0\times\mathcal{P}$ or $\partial_f\Omega^0\times\mathcal{P}$ as a sum of products of integrals defined over $\mathcal{P}$ and Ω^0 or $\partial_f\Omega^0$ as proposed in [3] and [11]. This is the reason why we propose to extend the Hyper Reduction method proposed in [12] and [13] for adaptive reduced-order methods. The simplified integration scheme is coined by the truncated integration method. One can notice that similar truncated integration scheme are also used in Earth science as an approximation of a complete integration scheme [14]. The particularity of the proposed approach is the extension of the truncated integration scheme to boundary value problems.

The adaptive algorithm used to construct the separated representation (1) is a predictor-corrector algorithm. As it is mentioned above, this algorithm is also an incremental algorithm. The time interval is split into time increments. The mechanical state has to be forecast at the end of each time increment knowing the state at the beginning of the time increment. The separated representation is adapted at each time increment, if necessary. The proposed algorithm is very similar to the one proposed in [11] the fact that it is applied step by step over the time interval using a truncated integration scheme. At time instant t, a separated representation is assumed to be known. During the prediction step, the known separated representation of the fields defined over $\Omega^0\times\mathcal{P}$ represents a reduced-order model. The values of the time functions $(a_j(t))_{j=1..\gamma}$ at the end of the time increment are the reduced state variable of this model. We claim that, if the amount of reduced state variables is small enough, a truncated integration domain can be introduced to formulate the equilibrium equations in order to estimate the reduced state variables. This truncated integration domain is denoted $\mathcal{W}_\Pi$, which is a submanifold of $\Omega^0\times\mathcal{P}$. The truncated integration domain is the support of truncated test functions related to the known separated representation.

In the formulation of the equilibrium equation proposed above the test functions belong to wide vector space. But various equilibrium conditions can be introduced using different vector spaces provided that the rank of these equations is equal to the number of unknowns. During the prediction step, the number of unknowns is equal to γ, which is the dimension of the reduced-order model defined by the separated representation. Therefore, as proposed in [12] and in [13], we propose to introduce the vector space of truncated test functions denoted $\mathcal{V}_\Pi$ is introduced such that:

$$\begin{aligned}\mathcal{V}_\Pi = \Big\{ &\underline{\boldsymbol{u}}^*(.,.)\in H^1(\Omega^0)\otimes L^2(\mathcal{P}) | \\ &\underline{\boldsymbol{u}}^*(\underline{\boldsymbol{X}},.,t)=0\ \forall \underline{\boldsymbol{X}}\in\partial_U\Omega^0 \end{aligned}$$

$$\left.\begin{aligned}
&\underline{\boldsymbol{u}}^*(\underline{\boldsymbol{X}},\{p\},t) = h(\underline{\boldsymbol{X}},\{p\})\sum_{j=1}^{j=\gamma}\underline{\boldsymbol{\phi}}_j(\underline{\boldsymbol{X}})g_j(\{p\})a_j^*\\
&h(\underline{\boldsymbol{X}},\{p\}) \in C^\infty(\Omega^0\times\mathcal{P})\\
&h(\underline{\boldsymbol{X}},\{p\}) = 0\ \forall(\underline{\boldsymbol{X}},\{p\}) \notin \mathcal{W}_{\Pi}\\
&h(\underline{\boldsymbol{X}},\{p\}) = 1 \text{ almost everywhere over } \mathcal{W}_{\Pi}
\end{aligned}\right\} \quad (10)$$

Using this vector space for test functions, the integrals over the complementary part of $\mathcal{W}_{\Pi}$ are equal to zero. Therefore the prediction problem is: knowing $(\underline{\boldsymbol{\phi}}_j)_{j=1,\ldots,\gamma}$ and $(g_j)_{j=1,\ldots,\gamma}$ find $(a_j(t))_{j=1,\ldots,\gamma}$ such that $\underline{\boldsymbol{u}} \in \mathcal{U}$ minimizes η_{Π} and such that:

$$\text{and } \eta_{\Pi} = \int_{\mathcal{W}_{\Pi}} \underline{\boldsymbol{r}}_v.\underline{\boldsymbol{r}}_v\, d\Omega^0\, dp + \int_{\partial_f\Omega^0\times\mathcal{P}\cap\mathcal{W}_{\Pi}} \underline{\boldsymbol{r}}_b.\underline{\boldsymbol{r}}_b\, d\Gamma^0\, dp \quad (11)$$

$$\begin{aligned}
&\int_{\mathcal{W}_{\Pi}} \underset{\sim}{\boldsymbol{\varepsilon}}(\underline{\boldsymbol{u}}^*,\underline{\boldsymbol{u}}) : \underset{\sim}{\boldsymbol{\Sigma}}(\underset{\sim}{\boldsymbol{F}}(\underline{\boldsymbol{u}}),\tau\le t,\{p\})\, d\Omega^0\, dp\\
&\quad - \int_{\partial_f\Omega^0\times\mathcal{P}\cap\mathcal{W}_{\Pi}} \underline{\boldsymbol{u}}^*.\underline{\boldsymbol{f}}(\underline{\boldsymbol{X}},t)\, d\Gamma^0\, dp\\
&= \int_{\mathcal{W}_{\Pi}} \underline{\boldsymbol{u}}^*.\underline{\boldsymbol{r}}_v\, d\Omega^0\, dp\\
&\quad + \int_{\partial_f\Omega^0\times\mathcal{P}\cap\mathcal{W}_{\Pi}} \underline{\boldsymbol{u}}^*.\underline{\boldsymbol{r}}_b\, d\Gamma^0\, dp \quad \forall\underline{\boldsymbol{u}}^* \in \mathcal{V}_{\Pi}
\end{aligned} \quad (12)$$

This prediction step is followed by the correction step if $\text{mes}(\Omega^0\times\mathcal{P})\eta_{\Pi} > \text{mes}(\mathcal{W}_{\Pi})\epsilon_r$. The correction step consists of finding an adapted separated representation solving (7). This equation being nonlinear with respect to $\underline{\boldsymbol{u}}$, finding its solution takes advantage of the prediction step. This solution is performed using a Newton-Raphson algorithm, which is an iterative algorithm. Several corrections $\underline{\boldsymbol{\delta u}}$ are added to the prediction $\underline{\boldsymbol{u}}$ solving the following linear problem with respect to $\underline{\boldsymbol{\delta u}}$: find $\underline{\boldsymbol{R}}_X(\underline{\boldsymbol{X}})$ and $R_p(\{p\})$ such that:

$$\underline{\boldsymbol{\delta u}} = \underline{\boldsymbol{R}}_X(\underline{\boldsymbol{X}})R_p(\{p\}) \quad (13)$$

$$\begin{aligned}
&\int_{\Omega^0\times\mathcal{P}} \underset{\sim}{\boldsymbol{\varepsilon}}(\underline{\boldsymbol{u}}^*,\underline{\boldsymbol{u}}) : (\underset{\sim}{\boldsymbol{\Sigma}}(\underset{\sim}{\boldsymbol{F}}(\underline{\boldsymbol{u}}),\tau\le t,\{p\})\\
&\quad + \underset{\sim}{\boldsymbol{K}} : \underset{\sim}{\boldsymbol{\varepsilon}}(\underline{\boldsymbol{\delta u}},0))\, d\Omega^0\, dp\\
&\quad - \int_{\partial_f\Omega^0\times\mathcal{P}} \underline{\boldsymbol{u}}^*.\underline{\boldsymbol{f}}(\underline{\boldsymbol{X}},t)\, d\Gamma^0\, dp\\
&= \int_{\Omega^0\times\mathcal{P}} \underline{\boldsymbol{u}}^*.\widehat{\underline{\boldsymbol{r}}}_v\, d\Omega^0\, dp\\
&\quad + \int_{\partial_f\Omega^0\times\mathcal{P}} \underline{\boldsymbol{u}}^*.\widehat{\underline{\boldsymbol{r}}}_b\, d\Gamma^0\, dp \quad \forall\underline{\boldsymbol{u}}^* \in \mathcal{V}_R
\end{aligned} \quad (14)$$

$$\int_{\Omega^0\times\mathcal{P}} \widehat{\underline{\boldsymbol{r}}}_v.\widehat{\underline{\boldsymbol{r}}}_v\, d\Omega^0\, dp + \int_{\partial_f\Omega^0\times\mathcal{P}} \widehat{\underline{\boldsymbol{r}}}_b.\widehat{\underline{\boldsymbol{r}}}_b\, d\Gamma^0\, dp \le \epsilon_r \quad (15)$$

where $\underset{\sim}{\boldsymbol{K}}$ is the classical tangent stiffness tensor. As proposed in [11] $\mathcal{V}_R$ is the set of test functions expressed as:

$$\underline{\boldsymbol{u}}^* = \underline{\boldsymbol{R}}_X^*(\underline{\boldsymbol{X}})R_p(\{p\}) + \underline{\boldsymbol{R}}_X(\underline{\boldsymbol{X}})R_p^*(\{p\}) \quad (16)$$

Due to this choice of test functions the previous problem is a nonlinear problem with respect to $\underline{\boldsymbol{R}}_X$ and R_p. The new functions $\underline{\boldsymbol{\phi}}$ and g are obtained by normalizing the functions $\underline{\boldsymbol{R}}$ and R_p respectively. A convenient approximate solution of (13) to (15) is provided by a fixed point algorithm. The first guess field $\underline{\boldsymbol{R}}_X$ is given by the equilibrium condition related to the point of $\mathcal{P}$ having the highest equilibrium residue. Concerning the numerical implementation of the method, $\underline{\boldsymbol{R}}_X$ is approximated using the classical 3D finite element description. R_p is a piecewise constant function. Therefore the multidimensional simulation can be viewed as a simultaneous simulation of similar mechanical problems. The problem to solve in order to find $\underline{\boldsymbol{R}}_X$ has the same dimension as a classical finite element model related to a unique value of parameters. Due to the separated representation of the displacements and due to the use of the finite element representation of the functions of the variable $\underline{\boldsymbol{X}}$, it is not always possible to choose ϵ_R as small as expected. We refer the reader to [15] for the analysis of the residue of the equilibrium equation depending on the finite element description.

4 Constitutive Law for Sintering Deformation

The proposed separated representation, the truncated integration scheme and the algorithm are generic. They can be applied to various mechanical problems. To illustrate the fact that complexity of the constitutive equations has no consequences on the applicability of the proposed method we applied it to simulate sintering transformations. These transformations can be viewed as irreversible thermal transformations coupled with viscoplastic transformations. The temperature is assumed to be uniform over the multidimensional domain $\Omega^0\times\mathcal{P}\times]t_0,t_f]$. In this paper, the multidimensional simulation aims to estimate the sensitivity of mechanical response to variations of material coefficients.

In general, the strain rate during sintering cycle of a ceramic body, consists of three terms: a reversible thermal strain rate, an irreversible sintering strain rate, and a viscoplastic strain rate, as shown in the following equation [1, 16–18]:

$$\dot{\underset{\sim}{\boldsymbol{\varepsilon}}} = \dot{\varepsilon}_{th}\underset{\sim}{\mathbf{1}} + \dot{\varepsilon}_s(f,T)\underset{\sim}{\mathbf{1}} + \dot{\underset{\sim}{\boldsymbol{\varepsilon}}}_{vp} \quad (17)$$

where $\underset{\sim}{\mathbf{1}}$ is the 2nd order unit tensor. The strain rate tensor is defined using the polar decomposition of the deformation gradient:

$$\begin{aligned} &\underset{\sim}{\boldsymbol{F}} = \underset{\sim}{\boldsymbol{R}}.\underset{\sim}{\boldsymbol{U}} \quad \text{and} \\ &\dot{\underset{\sim}{\boldsymbol{\varepsilon}}} = \frac{1}{2}\underset{\sim}{\boldsymbol{R}}^T.(\dot{\underset{\sim}{\boldsymbol{F}}}.\underset{\sim}{\boldsymbol{F}}^{-1} + \underset{\sim}{\boldsymbol{F}}^{-T}.\dot{\underset{\sim}{\boldsymbol{F}}}^T).\underset{\sim}{\boldsymbol{R}} \end{aligned} \tag{18}$$

where $\underset{\sim}{\boldsymbol{R}}$ is a pure rotation tensor. The conjugate stress $\underset{\sim}{\boldsymbol{G}}$ is such that:

$$\underset{\sim}{\boldsymbol{\sigma}} = \underset{\sim}{\boldsymbol{R}}.\underset{\sim}{\boldsymbol{G}}.\underset{\sim}{\boldsymbol{R}}^T \tag{19}$$

The sintering strain rate is a function of the temperature (T) and the porosity (f) as expressed in the following term:

$$\dot{\varepsilon}_s(f,T) = -f^y A_s \exp\left(\frac{-Q_s}{RT}\right) \tag{20}$$

The viscoplastic strain rate induced by the mechanical stress $\underset{\sim}{\boldsymbol{G}}$ is described as:

$$\underset{\sim}{\boldsymbol{G}} = \eta(T)\underset{\sim}{\boldsymbol{M}}^{(4)}(T,f) : \dot{\underset{\sim}{\boldsymbol{\varepsilon}}}_{vp} \tag{21}$$

Where η is the viscosity, $\underset{\sim}{\boldsymbol{M}}^{(4)}(T,f)$ is the 4th order tensor which does not generally depend on the stress tensor $\underset{\sim}{\boldsymbol{\sigma}}$ since the stress level is very small:

$$\underset{\sim}{\boldsymbol{M}}^{(4)}(T,f) = F(f)\underset{\sim}{\boldsymbol{I}}^{(4)} + \frac{3}{2}C(f)\underset{\sim}{\boldsymbol{J}}^{(4)} \tag{22}$$

where $\underset{\sim}{\boldsymbol{I}}^{(4)}$ and $\underset{\sim}{\boldsymbol{J}}^{(4)}$ are fourth order tensors that respectively extract the trace and the deviatoric part of a second order tensor:

$$\underset{\sim}{\boldsymbol{I}}^{(4)} : \dot{\underset{\sim}{\boldsymbol{\varepsilon}}}_{vp} = \mathrm{Tr}(\dot{\underset{\sim}{\boldsymbol{\varepsilon}}}_{vp})\underset{\sim}{\mathbf{1}} \tag{23}$$

$$\underset{\sim}{\boldsymbol{J}}^{(4)} : \dot{\underset{\sim}{\boldsymbol{\varepsilon}}}_{vp} = \dot{\underset{\sim}{\boldsymbol{\varepsilon}}}_{vp} - \frac{1}{3}\mathrm{Tr}(\dot{\underset{\sim}{\boldsymbol{\varepsilon}}}_{vp})\underset{\sim}{\mathbf{1}} \tag{24}$$

The coefficients C and F depend on the porosity (f). In a dense body case where $f = 0$, $C = 1$ and $F = 0$. They are assumed as the following form:

$$C(f) = 1 + xf^n, \qquad F(f) = zf^m \tag{25}$$

The viscosity is expressed as:

$$\eta(T) = B_s \exp\left(\frac{-Q_s}{RT}\right) \tag{26}$$

Where Q_s and T are activation energy and absolute temperature respectively. The change of porosity is governed by the strain rate such that:

$$\dot{f} = (1-f)\,\mathrm{Tr}(\dot{\underset{\sim}{\boldsymbol{\varepsilon}}} - \dot{\varepsilon}_{th}\underset{\sim}{\mathbf{1}}) \tag{27}$$

A_s, B_s, Q_s, m, n, x, y and z are the intrinsic coefficients of the material which have to be identified by experimental tests.

5 Numerical Results of the Multidimensional Simulation

5.1 The Finite Element Representation

As mentioned in the previous section, the isotropic sintering deformations consist of various parameters associated with either sintering (thermal) or mechanical solicitations. Due to the variability of the material properties, it is interesting to study the sensitivity of the mechanical response to different material coefficients. One can imagine that the parameters that have the smallest effect could be identified for a large class of materials. Otherwise, the parameters having a greater effect should be specified with greater accuracy for each considered materials.

In this study, the effect of perturbations of mechanical input parameters have been investigated on the bending of a cantilever beam as the response. The response of two results to the input perturbation were investigated: (i) Maximum deflection of the cantilever beam due to sintering (U_2); (ii) Maximum horizontal displacement (U_1) of the cantilever beam during thermal treatment. The column of responses is denoted $\{Y\}$, $\{Y\}^T = \{U_2, U_1\}$. Two levels full factorial design experiment is considered on 5 mechanical parameters of the model. In other words, 2^5 points of $\mathcal{P}$ have been investigated in order to create a Latin hypercube sampling. We propose to simulate simultaneously these 32 numerical cases. The representation of the parameters being piecewise constant, it turns out that the numerical model is a discontinuous finite element model defined in a virtual Euclidean space $\widehat{\Omega}^0$ which mimics the domain $\Omega^0 \times \mathcal{P}$. The mechanical system defined in $\widehat{\Omega}^0$ contains 32 cantilever beams which are associated with every perturbation case studies. This geometry is presented in Fig. 1 which possesses 12800 quadrangular elements (32×400).

The Reduced Integration Domain has been built using the method proposed in [12] and adding all the element of the first beam into the RID. Figure 2 shows the elements in red over which the function h in (10) is not null.

5.2 Parameter Assignation

The parameters whose values were constant throughout the investigation were all associated with sintering (thermal) aspect of the model. These fixed parameters and the values assigned to them are listed in Table 1.

The influence of $\pm 5\%$ perturbation of mechanical parameters of the model is examined using the proposed separated-representation-based algorithm. The corresponding model coefficients and their physical-based optimized values have been presented in Table 2.

The first two parameters (x and n) are associated with the deviatoric part of the model ($C(f)$) which represents the

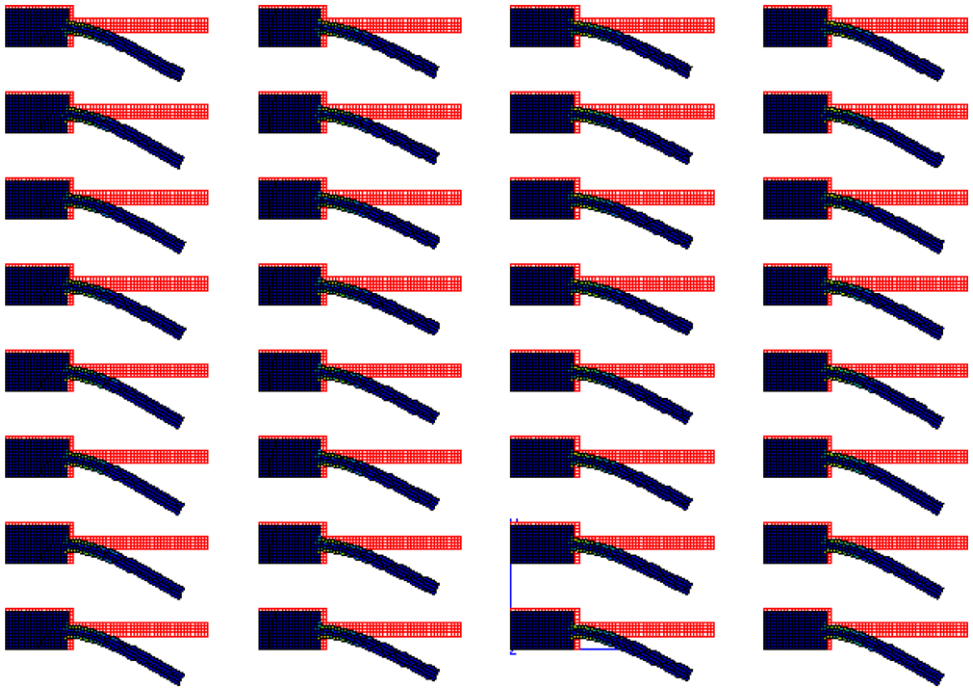

Fig. 1 Mesh and example of Von Mises stress related to the multidimensional problem viewed in virtual 2D space $\widehat{\Omega}^0$ that mimic $\Omega^0 \times \mathcal{P}$

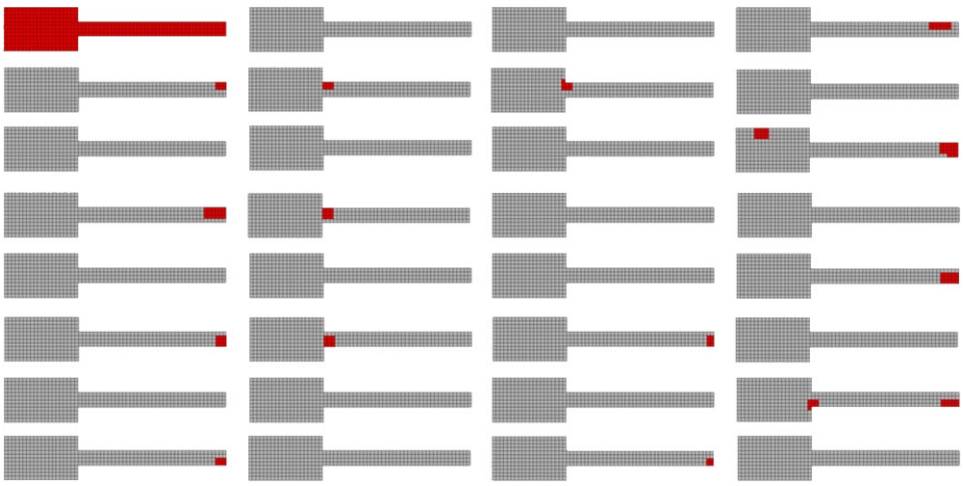

Fig. 2 (Color online) Finite element mesh and reduced integration domain (*red* or *dark gray*) used for mechanical parameters sensitivity analysis with the separated representation

Table 1 Sintering parameters after optimisation

Model parameters	Optimised values
A_S	1.2548274354e+3
y	4.5206134869
Q_S	1.8133327934e+5

Table 2 Mechanical parameters after optimisation

Model parameters	Optimised values
x	1.45386139054
n	1.06450577625
z	9.16276723203e−1
m	1.2735633572
B_S	8.76336201142e−3

distortion due to shear solicitation during sintering. The next couple of input parameters (z and m) which are related to the spherical part of the model ($F(f)$) represent the volume change (shrinkage due to sintering) of the porcelain. The last influential parameter (B_s) is representative of the viscosity of powder made body during thermal treatment.

5.3 Construction of the Sensitivity Matrix

Each of the five variable parameters of the model was assigned high and low values and a unique simulation was run

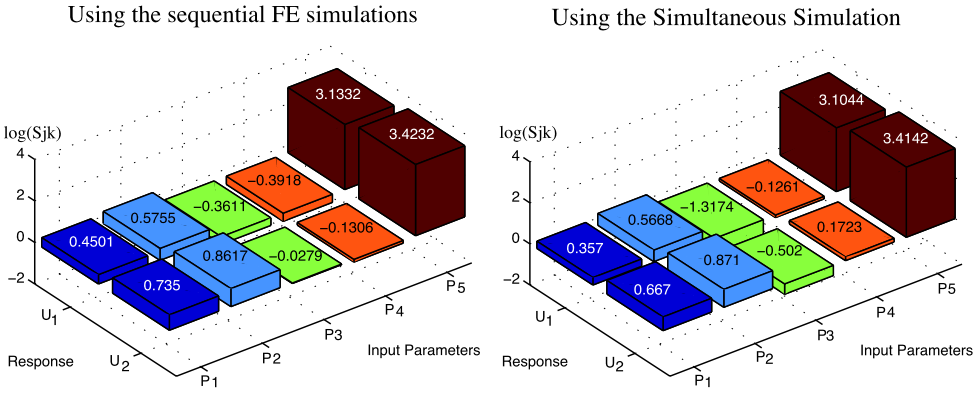

Fig. 3 Sensitivity of response to parameters perturbation in full FEM simulation

with every possible combination of parameter assignments, i.e. a 2^5 samplings:

$$\{p\} = \begin{pmatrix} x \\ n \\ z \\ m \\ B_s \end{pmatrix} = \{p_0\}, \{p_1\}, \{p_2\}, \ldots, \{p_{32}\} \tag{28}$$

After the simultaneous simulation, it is possible to use standard techniques to analyse the variance of the response variables which was performed on a PC using spreadsheet and matlab. We assume that the two responses of interest are linearly linked to the five parameters by a sensitivity matrix $[S]$. The response deviation from the reference case was calculated for all the possible cases by:

$$\{\delta Y_i\} = \{Y_i\} - \{Y_0\} \tag{29}$$

In the same way, the coefficient deviation from the reference value was also determined:

$$\{\delta p_i\} = \{p_i\} - \{p_0\} \tag{30}$$

Then the sensitivity matrix is decomposed into two different matrixes and related to the parameters deviation matrix:

$$\{\delta Y_i\} = [G_i].\{\widehat{S}\} = [S].\{\delta p_i\} \tag{31}$$

The matrix $[G_i]$ involves the values of $\{\delta p_i\}$ in order to introduce a column form of the sensitivity matrix. By minimizing the following term, the non-dimensionalised modulus ($d(\widehat{S})$) used as sensitivity index was obtained:

$$J(\widehat{S}) = \sum_{i=1}^{32} (\{\delta Y_i\} - [G_i].\{\widehat{S}\})^T.(\{\delta Y_i\} - [G_i].\{\widehat{S}\}) \tag{32}$$

$$dJ(\widehat{S}) = -2 \sum_{i=1}^{32} d(\widehat{S})^T.[G_i]^T (\{\delta Y_i\} - [G_i].\{\widehat{S}\}) \tag{33}$$

$$dJ(\widehat{S}) = 0 \tag{34}$$

$$\left(\sum_{i=1}^{32} [G_i]^T.[G_i] \right).\widehat{S} = \sum_{i=1}^{32} [G_i]^T.\{\delta Y_i\} \tag{35}$$

5.4 Accuracy of the Simultaneous Simulation Using Truncated Integration Scheme

In this part, the results provided by the proposed algorithm and the results obtained by a classical sequential FE solution are compared. The classical FE solution consists of 32 FE solutions related to each parameter value. This solution being performed one after an other. The sensitivity histogram of full FEM computation is presented in Fig. 3 showing the 10 sensitivity coefficients (5 parameters $\times$ 2 responses) of matrix $[S]$. The x axis shows the 5 input parameters (x, n, z, m, B_s) respectively while the responses (U_1 and U_2) are located on y axis. The relative sensitivity of the response variables to the input parameters can be obviously noticed along z axis, using a logarithmic scale. For instance, $\pm 5\%$ perturbation of 5th parameter (B_s) which is related to the viscosity term of the model, is the most influential in terms of the sensitivity magnitude on both responses whereas the same perturbation of parameters associated with the spherical part of the model (z and m) doesn't disturb either of the responses.

As a matter of hierarchy, the deflection of the cantilever beam and its horizontal displacements during sintering are mostly sensitive to viscosity perturbation rather than either the deviatoric or spherical part of the model. Therefore the viscosity should be determined accurately. The other mechanical parameters of the method could be possibly determined for a large set of similar materials.

The qualitative results obtained using a separated-representation-based algorithm are very closed to that of full finite element analysis (Fig. 3) since the most sensitivity is caused by viscosity disturbance (B_s) and neither of responses are disturbed by the parameters of the spherical part of the model (z and m).

Table 3 Global solutions N_g, local solutions N_l and number of unknowns N_u related to each strategy

Strategies	N_g	N_l	N_u
Sequential FEM	$32 \times 981 = 31392$	$32 \times 1{,}569{,}600 = 50{,}227{,}200$	946
Simultaneous simulation without truncated integration scheme	1399	60,108,800	1399
Simultaneous simulation using truncated integration scheme	1399	7,760,400	1399

5.5 Efficiency of the Simultaneous Simulation Using Truncated Integration Scheme

In this section, three computational strategies were compared: (i) the classical FE sequential solution; (ii) the simulation of the simultaneous problems using a separated-representation-based algorithm without truncated integration scheme; (iii) the simulation of the simultaneous problems using both a separated-representation-based algorithm and a truncated integration scheme. As mentioned above, the problem to solve in order to find $\underline{\boldsymbol{R}}_X$ has the same dimension as a classical finite element model related to a unique value of parameters. Therefore, the number of linear problems of classical FE dimension solved when using each strategy is compared. This number is denoted N_g. For this example the dimension of this linear problem is 946. Moreover, to evaluate the complexity reduction due to the use of the truncated integration scheme, we compare the number of local computations (at Gauss points) of the stress over a time increment involved when using each strategy. This number is denoted N_l. Finally, the number of unknowns, denoted N_u, related to each representation were also compared. For the classical FEM strategy N_u is the number of degrees of freedom. For the proposed strategy N_u is the value of γ, (1), at the end of the simultaneous simulation.

As the simultaneous problems are uncoupled, it does not make sense to compare γ to the number of degrees of freedom of the simultaneous FE model which is 32×946. Therefore in this case there is no reduction of the number of unknowns. But the number of linear global solutions has been divided by 22. Without using the proposed truncated integration scheme the separated-representation-based algorithm increases the complexity of the local computations because the related equations are inseparable. The truncated integration scheme enables us to reduce the complexity of the local computations because the number of computations of the stress at a Gauss point over a time increment has been divided by 6.5. Therefore, the truncated integration scheme makes very efficient the solver based on the separated representation in case of simultaneous simulation involving inseparable equations.

6 Conclusion

The sensitivity analysis of mechanical parameter of sintering model has been performed by three different strategies: (i) Full (classic) sequential finite element analysis; (ii) simultaneous simulation using a separated-representation-based solver without truncated integration scheme; (iii) simultaneous simulation using a separated-representation-based solver with truncated integration scheme. The separated representation has been applied distinguishing three kinds of functions: (i) the space functions, (ii) the time functions, (iii) and the functions depending on the material coefficients of the sintering model. The comparison of the results of the three strategies shows the identical sensitivity matrices with different computational complexities. It is clear that the truncated integration scheme improves the efficiency of the separated representation in this case which involves inseparable equations. The number of local computations related to the stress evaluation has been divided by 6.5. During the construction of the separated representation new state functions have been constructed solving linear systems of a dimension equal to the dimension of the classical FE sequential model. The complexity reduction related to the space functions comes from the reduction of the number of linear problems to solve. This number has been divided by 22. Work in progress concerns the reduction of terms involved in the separated representation in case of simultaneous simulation, and the parallelization of the proposed solver.

References

1. Besson J, Abouaf M (1991) Behaviour of cylindrical hip containers. Int J Solids Struct 691–702
2. Ammar A, Mokdad B, Chinesta F, Keunings R (2006) A new family of solvers for some classes of multidimensional partial differential equations encountered in kinetic theory modeling of complex fluids. J Non-Newton Fluid Mech 139:153–176
3. Ammar A, Mokdad B, Chinesta F, Keunings R (2007) A new family of solvers for some classes of multidimensional partial differential equations encountered in kinetic theory modeling of complex fluids. Part ii: transient simulation using space-time separated representations. J Non-Newton Fluid Mech 144:98–121
4. Chinesta F, Ammar A, Joyot P (2008) The nanometric and micrometric scales of the structure and mechanics of materials revisited: an introduction to the challenges of fully deterministic numerical descriptions. Int J Multiscale Comput Eng 6:191–213

5. Chinesta F, Ammar A, Falco A, Laso M (2007) On the reduction of stochastic kinetic theory models of complex fluids. Model Simul Mater Sci Eng 15:639–652
6. Mokdad B, Pruliere E, Ammar A, Chinesta F (2007) On the simulation of kinetic theory models of complex fluids using the Fokker–Planck approach. Appl Rheol 17:1–14
7. Pruliere E, Ammar A, El Kissi N, Chinesta F (2009) Multiscale modelling of flows involving short fibersuspensions. Arch Comput Methods Eng, State Art Rev 16:1–30
8. Germain P, Nguyen QS, Suquet P (1983) Continuum thermodynamics. J Appl Mech 50:1010–1020
9. Lemaitre J, Chaboche J-L (1985) Mecanique des materiaux solides. Dunod, Paris. English version published by Cambridge University Press, Cambridge, 1st edn (1990)
10. Sansour C, Kollmann FG (1997) On theory and numerics of large viscoplastic deformation. Comput Methods Appl Mech Eng 146:351–369
11. Gonzalez D, Ammar A, Chinesta F, Cueto E (2009) Recent advances on the use of separated representations. Int J Numer Methods Eng
12. Ryckelynck D (2005) A priori hypereduction method: an adaptive approach. Int J Comput Phys 202:346–366
13. Ryckelynck D (2009) Hyper reduction of mechanical models involving internal variables. Int J Numer Methods Eng 77(1):75–89
14. Vanieck P, Jaak J, Featherstone WE (2003) Truncation of spherical convolution integrals with an isotropic kernel. Stud Geophys Geod 47:455–465
15. Babuska I, Rheinbolt WC (1978) A posteriori error estimates for adaptive finite element comptation. Numer Methods Eng 12:1597–1615
16. Song J, Gelin JC, Barrire T, Liu B (2006) Experiments and numerical modelling of solid state sintering for 316l stainless steel components. J Mater Process Technol 352–355
17. Gasik M, Zhang B (2000) A constitutive model and FE simulation for the sintering process of powder compacts. Comput Mater Sci 93–101
18. Bordia RK, Zuo R, Guillon O, Salamone SM, Redel J (2006) Anisotropic constitutive laws for sintering bodies. Acta Mater 111–118

Conclusions – Prospects

Sintering is a key part for producing materials in a useful and robust form, especially ceramics and generally porous materials, and involves heating the porous structure or a powder compact.
Theories about exactly what happens during sintering have provided the subject of innumerable scientific papers. Suffice to mention that atomic diffusion takes place and the welded areas formed during compaction grow until eventually they disappear.
As mentioned above, sintering leads to progressively increased strength by causing the particles to weld together by diffusion. Generally, the part tends to increase in density as sintering proceeds and this still further improves the mechanical properties. Increase in density implies, of course, an overall shrinkage which leads to complications. It should however be noted that dimensional change is influenced also by compact density: the lower this is the greater the tendency to shrink. This is one of the reasons that uniformity of density of the compact is of such importance. If there is significant variation from one part to another the differential dimensional change in the various sections can lead to warpage.
From the technological point of view, it is critical to understand how to control this dimensional change and allow it in the design and manufacture of tools in order to ensure that reproducible materials of high quality are obtained. This controlling procedure is usually performed by trial and error in industry which costs a lot. A much cheaper alternative is modelling the dimensional change of ceramic compacts during sintering by finite element analysis.

Main results

The results presented in this work can be divided into six main parts:

- Experimental methods for characterizing thermo-mechanical properties of ceramic materials during sintering: Densification (dilatometry) and pyroplastic behaviour analyses.
- Developing a novel laser-assisted sinter-bending test platform for studying pyroplastic behaviour of materials.
- Two material-process couples have been studied: Traditional porcelain manufactured by slip casting process, Investment casting mould core or shell manufactured by injection moulding process.
- Two constitutive models have been developed according to experimental results.
- Parameter identification procedure by experiment-numerical simulation correlation.
- Prediction of ceramic deformation during sintering using identified parameters of developed constitutive laws.

Anisotropic densification behaviour is observed for traditional porcelain manufactured by slip casting process. The origin of anisotropy of shrinkage is associated with manufacturing process. However, a ceramic part with three different dimensions along various axes, will develop preferential orientations relative to its surfaces which are in contact with the plaster mould during drying stage. Consequently, these preferential orientations will influence material deformation under thermo-mechanical loading. Furthermore, the anisotropic constitutive model of sintering is developed in order to simulate the observed experimental behaviour.
Thermo-mechanical behaviour of ceramic core materials used for manufacturing turbine blade supper-alloys by investment casting is also studied. These ceramic parts are made from a special almost shrinkage-free composition (zircon-silica). In this system a chemical reaction occurs during sintering process which will block shrinkage deformation. In order to simulate

this behaviour, a reactive sintering constitutive model is developed.
This work has been carried out in the framework of a national project with numerous industrial partners. The goal of the project was to develop a convivial numerical program as well as associated experimental platforms for ceramic manufacturers. Therefore, the economic and technical restrictions have been taken into account in order to propose a systematic and simple procedure for experimental tests, numerical identification and finite element simulation of ceramic parts.

Prospects

According to this research work, the following prospects can be proposed:

- Experimental fracture analysis during sintering
  The sinter-bending test platform can be used for studying the fracture mechanics of powder-made materials at high temperature. For this purpose, a notched ceramic beam can be used for sinter-bending experiment. Crack initiation and propagation can be even observed visually.

- Numerical simulation of fracture during sintering
  The sintering constitutive model can be coupled with fracture mechanics models like cohesive zone, etc in order to simulate ceramic warpage during firing process. Numerical and experimental images of sintering notched ceramic beams are presented in the following figures:

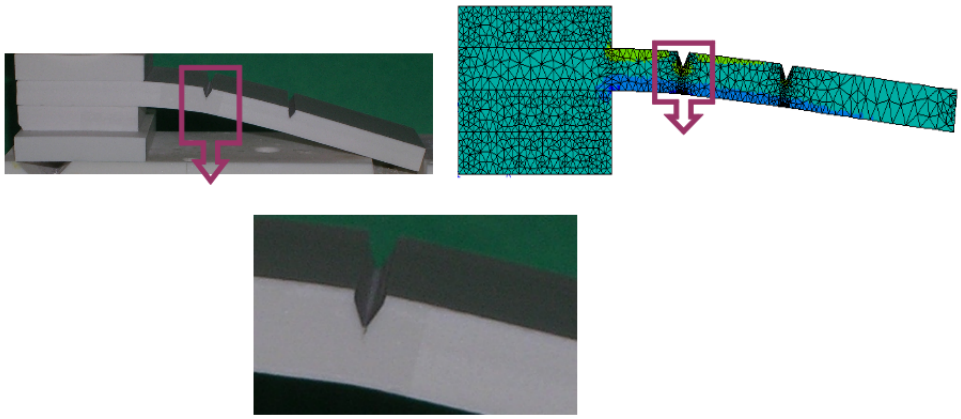

- Micro-mechanical simulation
  Nowadays, the main research works on numerical simulation of ceramic sintering are at micromechanical scale. From the industrial point of view, micro-mechanical modelling can not still be applied on an actual part since the simulation time and cost can not be compensated by the value of results obtained.

- Image analysis
  An alternative for direct optimisation process can be image correlation. Thus, it can also be used as validation for finite element simulation. In this regard, the sinter-bending test platform should be equipped by high temperature image recording system. After correlating the images obtained before and after sintering, the phenomenological constitutive model can be more precisely calibrated.

Bibliography

Watanabe, N., *Fundamental parameters of casting slips and methods of their measurement*, J. Ceram. Soc. Japan Pages: 561-571, 1972

Besson, J. and Abouaf, M., *Behaviour of cylindrical HIP containers*, Int. J. Solids Structures, Pages: 691-702, 1991

Besson, J. and Abouaf, M., *Grain growth enhancement in Alumina during Hot Isostatic Pressing*, Acta Metall. Mater. Pages: 2225-2234, 1991

Besson, J. and Foerch, R., *Large scale object-oriented finite element code design*, Comp. Meth. Appl. Mech. Engng, Pages: 165-187 1997

Takao, Y. and Hotta, T. and Naito, M. and Shinohara, N. and Okumiya, M. and Uematsu, K., *Microstructure of alumina compact body made by slip casting*, J. European Ceram. Soc., Pages: 397-401, 2002

Sidoroff, F. and Dogui, A., *Some issues about anisotropic elastic-plastic models at finite strain*, Int. J. Solids Structures, Pages: 9569-9578, 2001

Seidel, J. and Claussen, N. and Rodel, J., *Reliability of alumina ceramics.2: Effect of processing*, J. European Ceram. Soc., Pages: 727-733, 1997

Young, A. and Omatete, O. and Janney, M. and Menchhofer, P., *GELCASTING OF ALUMINA*, J. American Ceram. Soc., Pages: 612-618, 1991

Evans, AG, *Structural Reliability: A Processing-Dependent Phenomenon*, journal of the American Ceramic Society, Pages: 127-137, 1982

F.F. Lange, *Powder processing science and technology for increased reliability.*, J. American Ceram. Soc., Pages: 3-15, 1989

Taruta, S. and Kitajima, K. and Takusagawa,N. and Okada, K. and Otsuka, N., *Burnout of binder and sintering behavior of powder compacts of bimodally distributed alumina powders with stearic acid and lyethleneglycol.*, J. Ceram. Soc. Japan, Pages: 1189-1194, 1991

Ryckelynck, D., *Hyper-reduction of mechanical models involving internal variables*, International journal for Numerical Methods in Engineering, Pages: 75-89, 2009

Ryu, B. and Takahashi, M. and Suzuki, S., *Rheological characterization of aqueous alumina slurry for tape casting.*, J. Ceram. Soc. Japan, Pages: 643-648, 1993

Naito, M. and Fukuda, Y. and Yoshikawa, N. and Kamiya, H. and Tsubaki, N., *Optimization of suspension characteristics for shaping processes.*, J. European Ceram. Soc., Pages: 251-257, 1997

Unuma, H. and Ryu, BH and Hatano, I. and Takahashi, M., *The adsorption behavior of dispersant molecules and rheological properties of highly concentrated alumina slurries.*, J. Soc. Powder Tech. Japan, Pages: 25-30, 1998

Ryckelynck, D. and Chinesta, F. and Cueto, E. and Ammar, A., *On the a priori model reduction: overview and recent developments*, Archives of Computational Methods in Engineering, Pages: 91-128, 2006

Song, J. and Gélin, JC and Barriére, T. and Liu, B., *Experiments and numerical modelling of solid state sintering for 316L stainless steel components*, journal of materials processing technology, Pages: 352-355, 2006

Ryckelynck, D. and Missoum Benziane, D., *Multi-level A Priori Hyper-Reduction of mechanical models involving internal variables* , Computer Methods in Applied Mechanics and Engineering, Pages: 1134-1142, 2010

Green, D.J. and Guillon, O. and Rodel, J., *Constrained sintering: A delicate balance of scales*, journal of the European Ceramic Society, Pages: 1451-1466, 2008

Kim, H. and Gillia, O. and Bouvard, D., *A phenomenological constitutive model for the sintering of alumina powder.*, J. European Ceram. Soc., Pages: 1675-1685, 003

Blaine, DC and Bollina, R. and Park, S.J. and German, RM, *Critical use of video-imaging to rationalize computer sintering simulation models*, Computers in Industry, Pages: 867-875, 2005

Hennige, VD and others, *Shrinkage-free ZrSiO4-ceramics: characterisation and applications*, journal of the European Ceramic Society, Pages: 2901-2908, 1999

Snape, RG and Clift, S.E. and Bramley, A.N., *Sensitivity of finite element analysis of forging to input parameters*, journal of Materials Processing Technology, Pages: 21-26, 1998

Taylor, R.L., *A mixed-enhanced formulation for tetrahedral finite elements*, Int. J. Numer. Meth. Engng, Pages: 205-227, 2000

Holm, E.A. and Battaile, C.C., *The computer simulation of microstructural evolution*, JOM journal of the Minerals, Metals and Materials Society, Pages: 20-23, 2001

Olevsky, E.A., *Theory of sintering: from discrete to continuum*, Materials Science and Engineering: R: Reports, Pages: 41-100, 1998

Bordia, R.K. and Scherer, G.W., *On constrained sintering-I. Constitutive model for a sintering body*, Acta Metallurgica, Pages: 2393-2397, 1988

Kraft, T. and Riedel, H., *Numerical simulation of solid state sintering; model and application*, journal of the European Ceramic Society, Pages: 345-361, 2004

Olevsky, E. and Molinari, A., *Instability of sintering of porous bodies*, International journal of Plasticity, Pages: 1-37, 2000

Coble, RL, *A model for boundary diffusion controlled creep in polycrystalline materials*, journal of Applied Physics, Pages: 1679-1682, 2009

Folweiler, R.C., *Creep Behavior of Pore-Free Polycrystalline Aluminum Oxide*, journal of Applied Physics, Pages: 773-778, 2009

Herring, C., *Diffusional viscosity of a polycrystalline solid*, journal of Applied Physics, Pages: 437-445, 2009

Nabarro, F.R.M., *Grain size, stress, and creep in polycrystalline solids*, Physics of the solid state, Pages: 1456-1459, 2000

Nabarro, F.R.N., *Creep at very low rates*, Metallurgical and Materials Transactions A, Pages: 213-218, 2002

Olevsky, EA and German, RM and Upadhyaya, A., *Effect of gravity on dimensional change during sintering*, Acta mater, Pages: 1167-1180, 2000

Riedel, H., *A Constitutive Model for the Finite-Element Simulation of Sintering-Distortions and Stresses*, Ceramic Powder Science III, Pages: 619-630, 1990

Hansen, J.D. and Rusin, R.P. and Teng, M.H. and Johnson, D.L., *Combined-stage sintering model*, journal of the American Ceramic Society, Pages: 1129-1135, 1992

Besson, J. and Abouaf, M., *Rheology of porous alumina and simulation of hot isostatic pressing*, journal of the American Ceramic Society, Pages: 2165-2172, 1992

Green, D.J. and Guillon, O. and Rodel, J., *Constrained sintering: A delicate balance of scales*, journal of the European Ceramic Society, Pages: 1451-1466, 2008

Svoboda, J. and Riedel, H. and Zipse, H., *Equilibrium pore surfaces sintering stresses and constitutive equations for the intermediate and late stages of sintering-I. Computation of equilibrium surfaces*, Acta metallurgica et materialia, Pages: 435-443, 1994

Kanters, J. and Eisele, U. and Rodel, J., *Cosintering simulation and experimentation: case study of nanocrystalline zirconia*, journal of the American Ceramic Society, Pages: 2757-2763, 2001

Raj, R., *Analysis of the sintering pressure*, journal of the American Ceramic Society, 1987

Zuo, R. and Aulbach, E. and Rodel, J., *Continuum mechanical approach to sintering of nanocrystalline zirconia*, Advanced Engineering Materials, Pages: 949-952, 2005

Guillon, O. and Rodel, J. and Bordia, R.K., *Effect of green-state processing on the sintering stress and viscosity of alumina compacts*, journal of the American Ceramic Society, Pages: 1637-1640, 2007

Cai, P.Z. and Messing, G.L. and Green, D.J., *Determination of the mechanical response of sintering compacts by cyclic loading dilatometry*, journal of the American Ceramic Society, Pages: 445-452, 1997

Mohanram, A. and Messing, G.L. and Green, D.J., *Densification and Sintering Viscosity of Low-Temperature Co-Fired Ceramics*, journal of the American Ceramic Society, Pages: 2681-2689, 2005

Chang, J. and Guillon, O. and Rodel, J. and Kang, S.J.L., *Uniaxial viscosity of gadolinium-doped ceria determined by discontinuous sinter forging*, journal of the European Ceramic Society, Pages: 3127-3133, 2007

Zuo, R. and Aulbach, E. and Rodel, J., *Experimental determination of sintering stresses and sintering viscosities*, Acta Materialia, Pages: 4563-4574, 2003

Ollagnier, J.B. and Guillon, O. and Rodel, J., *Effect of anisotropic microstructure on the viscous properties of an LTCC material*, journal of the American Ceramic Society, Pages: 3846-3851, 2007

Zuo, R. and Rodel, J., *Temperature dependence of constitutive behaviour for solid-state sintering of alumina*, Acta Materialia, Pages: 3059-3067, 2004

Ostrowski, T. and Rodel, J., *Evolution of mechanical properties of porous alumina during free sintering and hot pressing*, journal of the American Ceramic Society, Pages: 3080-3086, 1999

Mohanram, A. and Lee, S.H. and Messing, G.L. and Green, D.J., *A novel use of constrained sintering to determine the viscous Poisson's ratio of densifying materials*, Acta Materialia, Pages: 2413-2418, 2005

Salamone, SM and Steams, LC and Bordia, RK and Harmer, MP, *Effect of rigid inclusions on the densification and constitutive parameters of liquid-phase-sintered YBa 2 Cu 3 O 6+ x powder compacts.*, journal of the American Ceramic Society, Pages: 883-892, 2003

Takao, Y. and Hotta, T. and Naito, M. and Shinohara, N. and Okumiya, M. and Uematsu, K., *Microstructure of alumina compact body made by slip casting*, journal of the European Ceramic Society, Pages: 397-401, 2002

Bitterlich, B. and Lutz, C. and Roosen, A., *Rheological characterization of water-based slurries for the tape casting process*, Ceramics International, Pages: 675-683, 2002

Young, A.C. and Omatete, O.O. and Janney, M.A. and Menchhofer, P.A., *Gelcasting of alumina*, journal of the American Ceramic Society, Pages: 612-618, 1991

Evans, A.G., *Structural reliability: a processing-dependent phenomenon*, journal of the American Ceramic Society, Pages: 127-137, 1982

Naito, M. and Fukuda, Y. and Yoshikaw, N. and Kamiya, H. and Tsubaki, J., *Optimization of suspension characteristics for shaping processes*, journal of the European Ceramic Society, Pages: 251-257, 1997

Germain, P. and Suquet, P. and Nguyen, QS, *Continuum thermodynamics*, ASME, Transactions, journal of Applied Mechanics, Pages: 1010-1020, 1983

Sansour, C. and Kollmann, FG, *On theory and numerics of large viscoplastic deformation*, Computer Methods in Applied Mechanics and Engineering, Pages: 351-369, 1997

Ammar, A. and Mokdad, B. and Chinesta, F. and Keunings, R., *A new family of solvers for some classes of multidimensional partial differential equations encountered in kinetic theory modeling of complex fluids*, journal of Non-Newtonian Fluid Mechanics, Pages: 153-176, 2006

Ryckelynck, D., *Hyper-reduction of mechanical models involving internal variables*, International journal for Numerical Methods in Engineering, Pages: 75-89, 2009

Kim, H.G. and Gillia, O. and Bouvard, D., *A phenomenological constitutive model for the sintering of alumina powder*, journal of the European Ceramic Society, Pages: 1675-1685, 2003

Gillia, O. and Josserond, C. and Bouvard, D., *Viscosity of WC-Co compacts during sintering*, Acta Materialia, Pages: 1413-1420, 2001

Scherer, G.W., *Sintering with rigid inclusions*, journal of the American Ceramic Society, Pages: 719-725, 1987

Raj, R. and Bordia, RK, *Sintering behavior of bi-modal powder compacts*, Acta Metallurgica, Pages: 1003-1019, 1984

Venturelli, C. and Paganelli, M., *The measurement of behaviour of ceramic materials during heat treatment.*, Ceramic Forum International, Pages: 37-40, 009

Bernardin, A.M. and de Medeiros, D.S. and Riella, H.G., *Pyroplasticity in porcelain tiles*, Materials Science and Engineering: A, Pages: 316-319, 2006

Kaiser, A. and Lobert, M. and Telle, R., *Thermal stability of zircon*, journal of the European Ceramic Society, Pages: 2199-2211, 2008

Gillia, O. and Bouvard, D., *Phenomenological analysis of densification kinetics during sintering: application to WC-Co mixture*, Materials Science and Engineering A, Pages: 185-191, 2000

Kim, H.G. and Gillia, O. and Dor é mus, P. and Bouvard, D., *Near net shape processing of a sintered alumina component: adjustment of pressing parameters through finite element simulation*, International journal of mechanical sciences, Pages: 2523-2539, 2002

Mori, K., *Finite element simulation of powder forming and sintering*, Computer methods in applied mechanics and engineering, Pages: 6737-6749, 2006

Toussaint, F. and Bouvard, D. and Tenaud, P. and Di Marcello, E., *Experimental and numerical analysis of the deformation of ferrite segments during sintering*, journal of materials processing technology, Pages: 72-78, 2004

Wang, Y.U., *Computer modeling and simulation of solid-state sintering: A phase field approach*, Acta materialia, Pages: 953-961, 2006

Zavaliangos, A. and Bouvard, D., *Numerical simulation of anisotropy in sintering due to prior compaction*, International journal of powder metallurgy, Pages: 58-65, 2000

Chao, C.H. and Lu, H.Y., *Optimal Composition of Zircon-Fused Silica Ceramic Cores for Casting Superalloys*, journal of the American Ceramic Society, Pages: 773-779, 2002

Lequeux, N. and Larose, P. and Boch, P. and Burkarth, N., *Low-shrinkage refractories by an infiltration technique*, journal of the European Ceramic Society, Pages: 23-27, 1994

Zhou, J.G. and He, Z., *Rapid pattern based powder sintering technique and related shrinkage control*, Materials and Design, Pages: 241-248, 1998

Wereszczak, AA and Breder, K. and Ferber, MK and Kirkland, TP and Payzant, EA and Rawn, CJ and Krug, E. and Larocco, CL and Pietras, RA and Karakus, M., *Dimensional changes and creep of silica core ceramics used in investment casting of superalloys*, journal of materials science, Pages: 4235-4245, 2002

Wilson, PJ and Blackburn, S. and Greenwood, RW and Prajapti, B. and Smalley, K., *The role of zircon particle size distribution, surface area and contamination on the properties of silica-zircon ceramic materials*, journal of the European Ceramic Society, 2011

Pohle, D. and Wagner, M. and Roosen, A., *Effect of friction on inhomogeneous shrinkage behavior of structured LTCC tapes*, journal of the American Ceramic Society, Pages: 2731-2737, 2006

Calata, J.N. and Lu, G.Q. and Chuang, T.J., *Constrained sintering of glass, glass-ceramic and ceramic coatings on metal substrates*, Surface and interface analysis, Pages: 673-681, 2001

Bordia, R.K. and Zuo, R. and Guillon, O. and Salamone, S.M. and Rodel, J., *Anisotropic constitutive laws for sintering bodies*, Acta materialia, Pages: 111-118, 2006

Zuo, R. and Aulbach, E. and Bordia, R.K. and Rodel, J., *Critical evaluation of hot forging experiments: case study in alumina*, journal of the American Ceramic Society, Pages: 1099-1105, 2003

Raj, P.M. and Cannon, W.R., *Anisotropic Shrinkage in Tape-Cast Alumina: Role of Processing Parameters and Particle Shape*, journal of the American Ceramic Society, Pages: 2619-2625, 1999

Raj, P.M. and Odulena, A. and Cannon, WR, *Anisotropic shrinkage during sintering of particle-oriented systems-numerical simulation and experimental studies*, Acta Materialia, Pages: 2559-2570, 2002

Boccaccini, A.R. and Trusty, P.A., *In situ characterization of the shrinkage behavior of ceramic powder compacts during sintering by using heating microscopy*, Materials characterization, Pages: 109-121, 1998

Ozer, IO and Suvaci, E. and Karademir, B. and Missiaen, JM and Carry, CP and Bouvard, D., *Anisotropic sintering shrinkage in alumina ceramics containing oriented platelets*, journal of the American Ceramic Society, Pages: 1972-1976, 2006

Zhang, W. and Gladwell, I., *Sintering of two particles by surface and grain boundary diffusion-a three-dimensional model and a numerical study*, Computational materials science, Pages: 84-104, 1998

Zhang, W. and Schneibel, JH, *The sintering of two particles by surface and grain boundary diffusion-A two-dimensional numerical study*, Acta metallurgica et materialia, Pages: 4377-4386, 1995

Shui, A. and Uchida, N. and Uematsu, K., *Origin of shrinkage anisotropy during sintering for uniaxially pressed alumina compacts*, Powder technology, Pages: 9-18, 2002

Degarmo, E.P. and Black, JT and Kohser, R.A., *Materials and Processes in Manufacturing, 2003*, John Wiley&Sons, New York, 2003

Huseby, IC and Borom, MP and Greskovich, CD, *High temperature characterization of silica-base cores for superalloys*, American Ceramic Society Bulletin, Pages: 448-452, 1979

Kato, K. and Nozaki, Y., *Ceramic Core for Precision Castings Manufactured by Injection Molding*, Imono, Pages: 155, 199l

Kato, K. and Nozaki, Y., *Ceramic core for solidification controlled casting*, 1990

Takayanagi, T. and Katashima, S., *Crystallization of the fused silica flour used to make ceramic core at elevated temperatures*, 1988

Mill, D. and Chem, C., *Properties of ceramic core, The British Investment Casters*, 1979

Wang, L.Y. and Hon, M.H., *The effect of cristobalite seed on the crystallization of fused silica based ceramic core-A kinetic study*, Ceramics international, Pages: 187-193, 1995

Wilson, PJ and Blackburn, S. and Greenwood, RW and Prajapti, B. and Smalley, K., *The role of zircon particle size distribution, surface area and contamination on the properties of silica-zircon ceramic materials*, journal of the European Ceramic Society, 2011

Jones, S. and Bentley, SA and Marquis, PM, *Effect of refractory phase separation on investment mould integrity*, British ceramic transactions, Pages: 100-105, 2002

Shi, Y. and Huang, X. and Yan, D., *Synthesis and characterization of ultrafine zircon powder*, Ceramics international, Pages: 393-400, 1998

Blaine, DC and Bollina, R. and Park, S.J. and German, RM, *Critical use of video-imaging to rationalize computer sintering simulation models*, Computers in industry, Pages: 867-875, 2005

Lemaitre, J. and Chaboche, J.L. and Germain, P., *Mécanique des matériaux solides*, 1985

King, A.G., *Ceramic technology and processing*, 2002

Bagchi, A. and Beaman, J.J., *Intelligent design and manufacturing for prototyping*, American Society of Mechanical Engineers, Atlanta, Georgia, December 1-6, 1991

Kang, S.J.L., *Sintering: densification, grain growth, and microstructure*, 2005

German, R.M., *Powder Metallurgy & Particulate Materials Processing*, 2005

Fantozzi, G. and Le Gallet, S. and Niepce, J.C., *Science & technologies céramiques*, 2011

Sarbandi, B. and Besson, J. and Boussuge, M. and Ryckelynck, D., *Anisotropic constitutive model and FE simulation of the sintering process of slip cast traditional porcelain*, AIP Conference Proceedings, 10th International Conference on Numerical Methods in Industrial Forming Processes, 2010

German, R.M., *Strength evolution in debinding and sintering*, Proceedings of the 3rd International Conference on the Science, Technology & Applications of Sintering, 2003

Shah, D.M. and Beals, J.T. and Marcin, J.J. and Murray, S.D., *Cores for use in precision investment casting*, 2001

Miller Jr, J.J. and Eppink, D.L. and Loxley, T.A., *Cores for investment casting process*, 1978

Beals, J.T. and Draper, S.D. and Lopes, J.A. and Murray, S.D. and Spangler, B.W. and Turkington, M.K. and Dube, B.P. and Santeler, K.A. and Snyder, J.A., *Investment casting cores*, 2003

Shah, D.M. and Marcin Jr, J.J. and Beals, T. and Murray, S.D., *Cores for use in precision investment casting*, 2008

Greskovich, C.D. and DeVries, R.C., *Alumina-based ceramics for core materials*, 1979

Crittz3t, *http://www.crittz3t.com*, 2006

Taub, S. and Kim, J.S., *Constrained Sintering Stress-Review*, 2010

Simulation numérique des déformations des produits céramiques lors du frittage

RÉSUMÉ :

Pour les fabricants de céramiques, il est primordial de maîtriser la déformation des pièces lors du frittage afin d'éviter les post-traitements et usinages ultérieurs qui augmentent les coûts de production. Face à ce problème, une alternative à la coûteuse démarche essai-erreur est la prévision par simulation numérique aux éléments finis des déformations des produits au cours du frittage. Pour une approche numérique, il faut d'abord développer des lois de comportement qui prennent en compte les différents mécanismes de déformation induits par le frittage. Les paramètres intrinsèques aux matériaux intervenant dans ces lois doivent être déterminés par l'expérience. Le but de cette thèse est de proposer des modèles prédictifs de la déformation des pièces céramiques lors du cycle de frittage. La procédure est basée sur une loi de comportement et les essais associés: l'essai de densification lors du frittage et l'essai de flexion-frittage. Deux matériaux différents ont été étudiés: Une porcelaine fabriquée par procédé dit de coulage et un réfractaire à base de zircon et de silice destiné à la fabrication de noyaux pour la fonderie de superalliages.
Les lois de comportement ainsi développées ont été implémentées dans le code de calcul par éléments finis "Zset". Après l'identification des paramètres des modèles, une simulation numérique par éléments finis a été réalisée sur des pièces génériques. Enfin la sensibilité des résultats aux paramètres d'une loi de comportement de frittage isotrope a été étudiée en utilisant une approche par réduction de modèle.

Mots clés : éléments finis, frittage, céramique, loi de comportement

Finite element simulation of ceramic deformation during sintering

ABSTRACT :

The control of the deformation of ceramic parts during the sintering process is essential, in order to avoid post-treatment and subsequent machining which increase the production costs. The procedure for obtaining the desired form after sintering is usually carried out by trial and error. An alternative to this costly approach is the prediction of shape instabilities during sintering by finite element simulation. With this aim, constitutive models have to be developed, taking into account the different deformation mechanisms induced by sintering.
These phenomenological constitutive models use different material parameters which must be determined by experiment. This thesis aims to propose a methodology for modelling the deformation of ceramics during sintering. This methodology consists in experimental analysis of densification and pyroplastic behaviour of ceramics, developing a phenomenological constitutive model and material parameters identification.
Two different materials have been studied: a porcelain manufactured by slip casting process and ceramic cores made by injection moulding and used for investment casting of superalloys.
The constitutive models have been implemented in the "Zset" finite element program. After identifying the model parameters, the finite element numerical simulation has been performed on representative parts.
Finally, the sensitivity of numerical results to mechanical parameters of an isotropic sintering model is analysed using a model reduction approach.

Keywords : finite element, sintering, ceramics, constitutive law

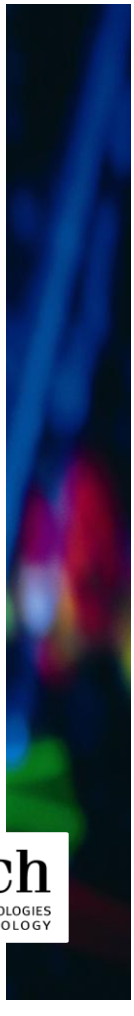

MINES ParisTech

ParisTech
INSTITUT DES SCIENCES ET TECHNOLOGIES
PARIS INSTITUTE OF TECHNOLOGY